MICROSTRUCTURE-PROPERTY RELATION IN $Li_{1.3}Al_{0.3}Ti_{1.7}(PO_4)_3$ SUPERIONIC Li-CONDUCTING CERAMICS

Von der Fakultät für Mathematik, Informatik und Naturwissenschaften der RWTH Aachen University zur Erlangung des akademischen Grades eines Doktors der Naturwissenschaften genehmigte Dissertation

vorgelegt von

Deniz Cihan Gündüz, M. Sc.

aus Aksehir, Türkei

Berichter: *Univ.-Prof. Dr. rer. nat. Rüdiger-A. Eichel*

Univ.-Prof. Dr. rer. nat. Joachim Mayer

apl. Prof. Dr. rer. nat. Ullrich Englert

Tag der mündlichen Prüfung: *11. März 2019*

Abstract

Lithium aluminium titanium phosphate ($Li_{1+x}Al_xTi_{2-x}(PO_4)_3$ LATP) is one of the materials under consideration as a solid electrolyte in future all solid-state lithium-ion batteries. In this work, I study the evolution of the microstructure of LATP ceramic samples, sintered between 900 and 1100 ^oC from $Li_{1.3}Al_{0.3}Ti_{1.7}(PO_4)_3$ powders prepared via a sol-gel route, by scanning electron microscopy (SEM) and confocal laser scanning microscopy (CLSM). LATP ceramics are highly brittle and they degrade under water; therefore, an all-oil-based grinding and polishing route was developed that does not alter the microstructure during sample preparation that allows differentiation of different microstructural components.

Sintering temperature dependent evolution of grain size, morphology, and connectedness as well as secondary phase content are tracked by CLSM and SEM. In addition to that, transmission electron microscopy (TEM) was used for the determination of grain boundary width and to identify the amorphous structure of the secondary phase. Goal of the work is to correlate the microstructure with total, grain and grain boundary resistance as extracted from electrochemical impedance spectroscopy via means of distribution of relaxation times (DRT). The latter showed a grain conductivity almost three order of magnitude larger than that of the grain boundaries. An increase of total conductivity with grain size is observed, which correlates with the grain size. However, at 1100 ^oC, total resistance increases with excess amount of secondary phase and crack formation comes into account.

In ceramic processing and for final macroscopic conductivity, the presence of secondary phases and porosity play an important role. In presence of more than one secondary phase and pores, image analysis must tackle the difficulties about distinguishing between these microstructural features. Therefore, I come up with a novel image segmentation and reconstruction method. In this work, we also study

the phase evolution of LATP ceramic samples by the image segmentation method based on elemental maps acquired in the scanning electron microscope combined with quantitative analysis of LATP grains. We find aluminium phosphate ($AlPO_4$) and another phosphate phase containing an only little amount of aluminium. It may contain lithium, which is not detectable by energy dispersive X-ray spectroscopy (EDS). The amount of these phases changes with sintering temperature which may influence the ionic conductivity of the whole material. First: As the grains act as an aluminium source for $AlPO_4$ formation, the aluminium content decreases decreasing also the intragranular conductivity. Second: Also, the amount of secondary phase changes from more $(Li_x)P_yO_z$ at 950°C to mainly $AlPO_4$ at 1100°C sintering temperature, which in addition may influence the grain boundary conductivity.

Kurzfassung

Lithium-Aluminium-Titan-Phosphat $Li_{1+x}Al_xTi_{2-x}(PO_4)_3$, kurz LATP, ist ein aussichtreicher Kandidat als Festkörperelektrolyt in Li-Ionen Batterien. In dieser Arbeit wird die Entwicklung der Mikrostruktur von gesinterten LATP-Keramiken, hergestellt aus über die sol-gel Methode gewonnen Pulver, in Abhängigkeit der Sintertemperatur von 900°C bis 1100°C mittels Rasterelektronen- (SEM) und Konfokaler Lasermikroskopie (CLSM) untersucht. Dabei wurden die Korngröße, -form, deren Konnektivität, sowie der Gehalt an Sekundärphasen und die Porosität genauer analysiert.

Darüber hinausgehend wurde auch die Transmissionselektronenmikroskopie (TEM) verwendet, um die Chemie und Struktur der Sekundärphasen und der Korngrenzen genauer zu beleuchten.

Ziel der Arbeit ist es, diese Ergebnisse mit dem Gesamtwiderstand der keramischen Pellets, gemessen mit makroskopischer elektrochemischer Impedanz Spektroskopie (EIS) zu korrelieren. Hier standen auch noch über die temperaturabhängige Verteilung von Relaxationszeiten (DRT) abgeleiteten Korn- und Korngrenzwiderstände zur Verfügung. Diese zeigten, dass der Haupteinfluss auf den Gesamtwiderstand die Korngrenzleitfähigkeit ist. Die Gesamtleitfähigkeit der Keramik wird dadurch hauptsächlich durch die Korngröße bestimmt und steigt mit der Korngröße. Bei 1100 ^oC steigt der Gesamtwiderstand aufgrund anderer Einflüsse.

Bei technischen Keramiken allgemein und in diesem Fall bei dem Einfluss auf die Gesamtleitfähigkeit spielt die Anwesenheit von Sekundärphasen und von Porosität eine entscheidende Rolle. Da sich durch das Vorliegen von zwei Sekundärphasen und Porosität die die quantitative Bildanalyse schwierig gestaltete, wurde diese zusätzlich an Elementverteilungskarten durchgeführt und das Gesamtgefüge aus diesen verschiedenen Bildern rekonstruiert. Als Sekundärphase wurden Aluminiumphosphat ($AlPO_4$) sowie ein weiteres Phosphat ohne

nennenswerten Aluminiumgehalt beobachtet. Da Lithium nicht mit Energie-dispersiver Röntgenanalyse (EDX) detektiert werden kann, können wir die Präsenz von Lithium in dieser Phase nicht ausschließen. Mit der Sintertemperatur nimmt der Gehalt an dieser Phase ab, während der Anteil an $AlPO_4$ steigt. Dies kann zum einen den Korngrenzwiderstand erhöhen, wenn diese mit $AlPO_4$ anstelle von Lithiumphosphaten benetzt werden. Zum anderen führt die Bildung von $AlPO_4$ zu einer Abnahme des Al-Gehalts in den Körnern und damit zu einem Anstieg des Widerstandes innerhalb der Körner. Beides sind negative Einflüsse auf den Gesamtwiderstand.

Contents

Chapter 1 : Introduction

1.1. Sustainable energy

Revolutionary changes have been taking place in science and technology since the start of the modern era. New inventions easily take their place in daily life of people. Cell phones and tablet computers are visible at-a-glance, televisions are considered even classical nowadays. These changes also bring forth a tremendous energy demand alongside. Moreover, developing countries require more and more energy year in and year out in correlation with their economic developments. It is expected that the total energy consumption of the developing world predominate over the rest of the world within the next thirty years [1]. Also considering the growth in human population, this enormous energy demand will increasingly continue in the future. The increase in global primary energy consumption was 1%, 0.9% and 1% in 2016, 2015 and 2014, respectively [2].

Despite the increasing world energy demand, there are some drawbacks of the currently dominating energy resources. Most of the energy is produced via fossil fuel consumptions nowadays [3]. However, fossil fuels are not sustainable sources of energy because of the simple fact that there are limited sources of fossil fuels. This lack of sustainable sources is a possible reason for political problems. Their extensive use also started deteriorating the climate. There are concerns that the earth might get warmer by 1-5 ^{o}C through the next century [4]. Rising sea levels are also associated with the extensive use of fossil fuels [5].

Considering the negative sides associated with the use of fossil fuels, a new approach is required in the area of energy consumption. The best alternative to currently dominating energy consumption habits is to switch to sustainable energy usage. It requires a great wealth of due-diligence. On the other hand, there are

various sustainable energy alternatives such as wind farms, geothermal power plants, photovoltaic cell farms and hydropower dams. Several examples of power plants employing suitable energy resources are depicted in Figure 1.1.

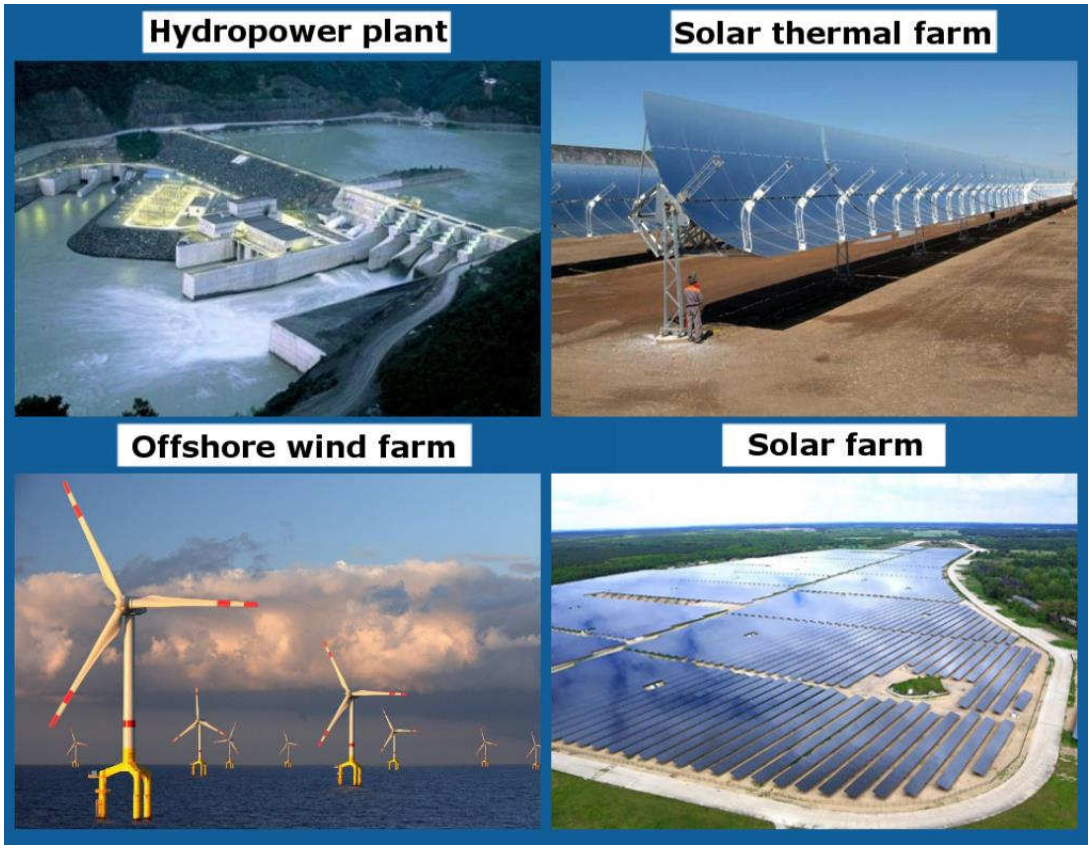

Figure 1.1: Exemplary power plants: a hydropower plant from Turkey [6], a solar thermal farm from USA [7], an offshore wind farm [8] and a solar farm from Germany [9].

Fossil fuels are both energy sources and storing the fossil fuels means storing energy at the same time. However, this is not the case for sustainable energy sources since they are usually used to generate electricity. Hence, there might be ups and downs in the energy production in this manner, for example photovoltaic panels only generate electricity through the day time but not through overnight. Similarly, there might be fluctuations depending on weather and seasons. The efficiency of hydropower plants is affected by rains as well as seasons. Therefore,

for an effective use of sustainable energy sources, compatible energy storage technologies are essential.

1.2. Batteries

With the change to renewable energies, the demand for energy storage systems increases. One quite established technology to store energy for mobile and stationary applications are batteries. A Battery is an electrochemical cell that transforms chemical into electricity. During the course of operation, the positive side of a battery is called cathode while the negative side is called anode. For energy storage only rechargeable batteries are applicable. Types of batteries range from lead-acid batteries to lithium-ion batteries. While in the first one chemical reactions take place at the electrodes, in lithium-ion batteries, which are abbreviated as LIBs, lithium ions are intercalated in the electrode materials.

LIBs are important in daily life since they are used in home electronics as well as portable electronics. Moreover, the use of LIBs is getting more and more space in military, battery electric vehicle (BEV), entertainment, computing, telecommunication and aerospace applications in a society that puts an unprecedented value on information [10]. The costs of LIBs` application in battery packs for electric vehicles are rapidly falling [11]. The main reason why lithium among the other metals is preferred lies under the fact that lithium is the most electropositive metal, which exhibits -3.04 V versus standard hydrogen electrode. Furthermore, it is also the lightest metal, its equivalent weight *M* is equal to 6.94 g mol^{-1} and its specific gravity is equal to 0.53 g cm^{-3}. This allows the systems providing high energy and high power densities [10]. In addition to this, LIBs exhibit only a tiny memory effect [12]. Due to all these positive sides of LIBs, they are not only a part of current world, but they are also promising for the future and research is on-going to improve the quality of them.

The middle part of batteries is called electrolyte. This needs to be conductive for Ions move through electrolytes but not for electrons, so that electrochemical reactions can take place and energy can be transferred to an external circuit.

The lithium-ion batteries available on the market nowadays work with organic liquid or gel electrolytes. However, liquid electrolytes have the drawbacks of being inflammable and requiring a leak tight battery case, which reduces the specific and volumetric energy density and adds additional costs. There were some recalls from some companies due to issues related to batteries; this includes the "Samsung Galaxy Note 7" recall because of the battery fires. Another drawback observed in the current lithium-ion batteries is their electrochemical instability because of the unstable lithium growth in the course of battery recharging [13][14]. Dendrites of lithium might be formed at the electrolyte-electrode interfaces of the batteries that employ organic liquid electrolytes. This can lead to short circuits or a decrease in battery capacity [10]. There is also the risk of freezing for the case of liquid or gel electrolytes [15]. Also, liquid electrolytes are hazardous to humans and the environment. All these properties are associated with the structure and/or the chemistry of components in use and the quest for better battery components is and must be going on.

1.3. Solid state batteries/electrolytes

Inorganic solid-state lithium-conducting electrolytes are being considered as potential candidates for next-generation lithium-ion batteries due to the aforementioned drawbacks of the organic liquid or gel electrolytes. The integration of inorganic solid-state lithium-conducting electrolytes into a lithium-ion battery with solid-state electrodes, instead of the liquid or polymer electrolytes are called all-solid-state lithium-ion batteries (ASSLIB). This technology is being considered as a real alternative to current lithium-ion battery technology employing liquid electrolytes, and it is expected to reach its full potential in the near future. The electrification of cars and even trucks is being considered as an important step in

transportation technology and it is also expected that they will be powered by ASSLIBs in the near future.

Ogava *et al.* showed that ASSLIBs can perform very well under a wide range of different operating temperatures [15]. The use of inorganic solid-state lithium-conducting electrolytes allows to overcome the key limitations of current technology associated with the use of the organic liquid or gel electrolytes, such as flammability and electrochemical instability [16]. Moreover, they can block finger like lithium-dendrite growth and therefore provide a safer battery design. They do not require a leak tight packaging which means less inactive material. Their tolerance to high temperatures is their most important advantages and also the long-term stability is considered to be higher.

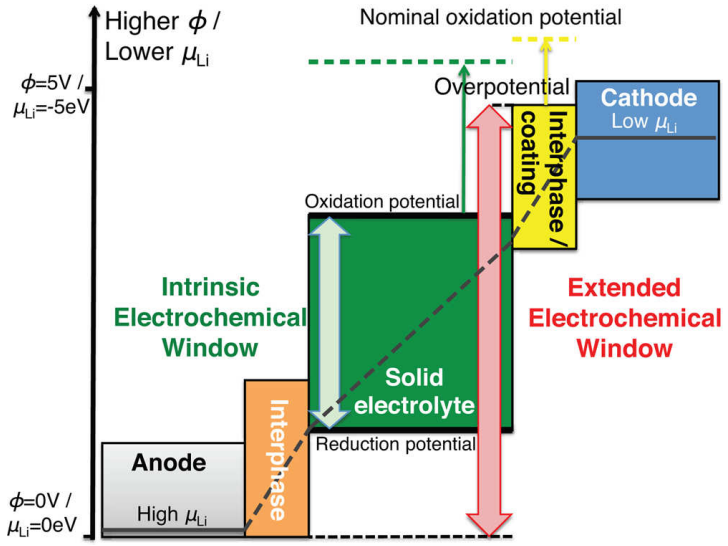

Figure 1.2: Schematic diagram on the electrochemical window and the lithium chemical potential profile in an all-solid-state lithium-ion battery [17].

Despite all its advantages, developing inorganic solid-state lithium-conducting electrolytes of lithium-ion conductivity comparable to state-of-the-art liquid electrolytes with conductivities $\geq 1\ \mathrm{mS\ cm}$, however, is a multi-scale challenge [18]. Criteria to tailor charge-transport properties in solids extend from atomic-scale

properties [13][19] over microstructural features related to intergranular contact [20] and secondary-phase formation [21] to interface issues in the full battery cell [22][23]. It is also expected that these electrolytes should be non-toxic, and they should not be expensive.

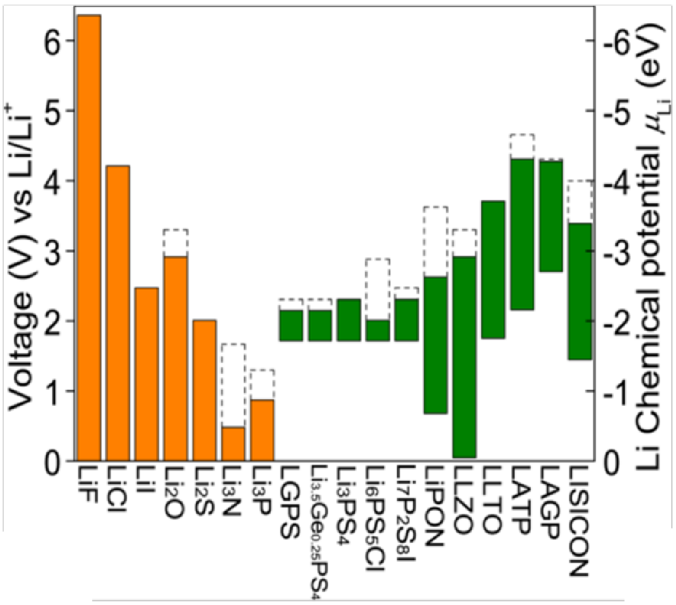

Figure 1.3: Electrochemical window of solid-state electrolytes and other materials [17].

Considering the overall advantages of inorganic solid-state lithium-conducting electrolytes over the liquid and gel electrolytes, a lot of effort have been devoted to develop various types of lithium ion conducting solid-state electrolytes, so far [24]. Promising ionic conductivities have been reported for Li_3N [25], perovskite type $La_{2/3-x}Li_xTiO_3$ [26], garnet type $Li_7La_3Zr_2O_{12}$ [27], thio LISICON-type $Li_{10}GeP_2S_{12}$ [28], B_2S_3–Li_2S–LiI glass [29], and NASICON-type $Li_{1+x}M_xTi_{2-x}(PO_4)_3$ [30][31].

Zhu *et al.* carried out first-principles calculations to study the electrochemical stability of lithium conducting solid-state electrolytes in all-solid-state lithium-ion batteries [17]. A schematic diagram on their studies is provided in Figure 1.2. They found out that great stability of the solid-state electrolytes is not

thermodynamically intrinsic; however, it arises due to kinetic stabilizations. Decomposition reactions have a cumbersome nature and they result in a high overpotential that leads to nominally wide electrochemical window. Their results suggest that the design of the interfaces and the decomposition interphases of the solid-state electrolyte are very important for the battery performance. Interphases exhibiting good electronic insulation and high lithium ion conductivity should employed so as to achieve an interface having a good stability and low resistance. They found that for Sulfide-based solid-state electrolytes the electrochemical window is significantly narrower than the of oxide-based solid-state electrolytes [17]. Despite the importance of interfaces, the current knowledge on the kinetics at the interfaces is poor. Wenzel *et al.* developed an in situ method to investigate interfacial reactions by photoelectron spectroscopy where they employ internal argon ion sputtering in a photoelectron spectrometer to deposit lithium on the specimen surface and to study the reaction between metal and solid-state electrolyte via photoelectron spectroscopy after lithium deposition [32]. Electrochemical window of solid-state electrolytes and other materials are shown in Figure 1.3 for a comparison. Focusing on solid-state electrolytes that can be processed under dry-room conditions, NASICON-type (Na Super-Ionic Conductor) $Li_{1+x}M_xTi_{2-x}(PO_4)_3$ lithium-conducting solid electrolytes are the materials of choice, as they combine high lithium-ion conductivity with stability under air [33][34] and electrochemical stability window from 2.17 V to 4.21 V [17]. This allows the fabrication and operation of an all phosphate all solid state battery with $Li_xV_2(PO_4)_3$ as cathode and $Li_xTi_2(PO_4)_3$ as anode materials over many cycles [35].

Chapter 2 : Fundamentals

2.1. NASICON structure

The advantages of NASICON-type (Na Super-Ionic Conductor) $Li_{1+x}M_xTi_{2-x}(PO_4)_3$ lithium-conducting solid-state electrolytes among the other solid-state electrolytes are discussed in the previous chapter. The ionic conductivity of the pure compound $LiTi_2(PO_4)_3$ is too low to be employed in an all-solid-state cell. Aono *et al.* demonstrated that partially substituting titanium with trivalent metal ions, $Li_{1+x}M_xTi_{2-x}(PO_4)_3$ (*M* = aluminium, scandium, yttrium, lanthanum, gallium, iron, indium, lutetium, or chromium) enhances the lithium-ion conductivity for x around 0.3 for all M^{3+} ions except for chromium [30][31].

The main difference between substituting titanium with different elements is that each element has a different ionic radius. As an example, the ionic radius of aluminium cation is equal to 0.535 Å, while titanium has a radius of 0.605 Å. Therefore, the ionic radius of aluminium cation is smaller than the radius of titanium. On the other hand, chromium cation, iron cation, indium cation, gallium cation, and scandium cation have the radiuses of equal to 0.615, 0.645, 0.80, 0.62, 0.745 Å, respectively. Therefore, all of them have a higher radius than titanium [36] and a direct relation to the ionic radii was not found by Aono *et al.* [30][31]. More influence on the conductivity was observed in the relation to porosity which is reduced upon substitution.

NASICON-type material $LiTi_2(PO_4)_3$ has a rhombohedral structure (with space group $R\bar{3}c$). It has a three-dimensional framework with alternating vertex-sharing MO_6 octahedra and PO_4 tetrahedra. MO_6 octahedra are positioned on the threefold axes of the unit cell, and lithium ions occupy the octahedral voids in the polyanionic $[Ti_2P_3O_{12}]^-$ framework. The phosphate backbone of the structure of L(A)TP with low packing density paves a way for channels where enough number of compensating

cations can find a place. In the NASICON framework, two different positions for the mobile lithium ions can be separated from each other. This position M1 in an octahedral void with threefold symmetry is on Wyckoff position 6b (0 0 0) in the space group $R\bar{3}c$ [37]. The M1 site is connected in a hexagonal plane to two other M1 sites and four M2 sites, and out of plane to four M1 sites and four M2 sites. The other void M2 is located M2 is located at 0.667, 0, 1/4 (or at 0, 0.333, 1/12), in Wyckoff position 18e with site symmetry 2 [37]. The M2 site has 6 nearest neighbour oxygens and is larger than M1 site. As the multiplicity is three times higher than that of the M1 site, the M2 site is partially filled with lithium ions. The M3 and M3' sites [38] are distorted (slight shift) M2 sites.

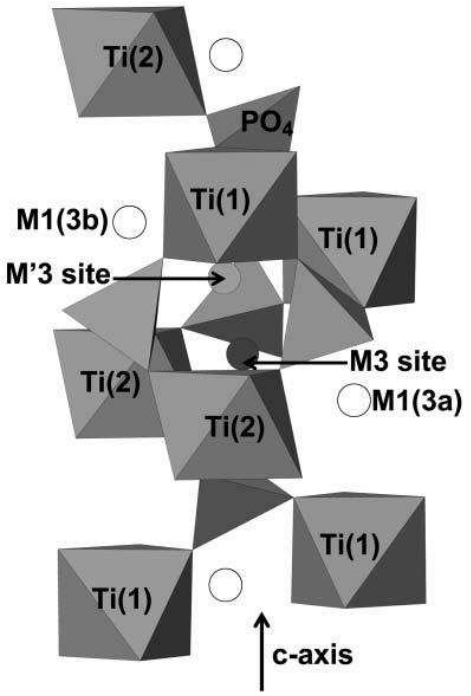

Figure 2.1: M3 and M'3 positions are shown in $Li_3Ti_2(PO_4)_3$ structure [38].

The structural effects of the partial substitution of tetravalent titanium in $LiTi_2(PO_4)_3$ via trivalent aluminium was reported by Dashjav *et al* [39]. During the substitution, lithium atoms maintain charge neutrality. Apart for the fully occupied

lithium position 6b site (Li1), excess lithium ions are refined at 6a site (Li2). As conduction path the cavities around the 6a site are proposed. With a thermal treatment at 1050 ^{o}C, they observed small amounts of $LiTiOPO_4$ phase; however, this does not change the crystal structure and the ion conduction of the main NASICON phase. Arbi *et al.* [40] report that lithium migration in LATP takes place between Li1 (6b) and Li3 in general position.

In addition to rhombohedral NASICON-type materials, a triclinic phase was also observed once the size of the tetravalent cation increases. In this triclinic phase, lithium ions locate between M1 and M2 sites in four-fold oxygen coordination [41][42]. In another report by the same research group, $Li_{0.5}Mn_{0.5}Ti_{1.5}Cr_{0.5}(PO_4)_3$ samples are studied [43]. It is found that manganese and lithium ions occupy M1 sites and electrochemically intercalated lithium ions are localized at M2 site.

Vibrational spectra studies show that phosphate bending modes are distorted more with the insertion of lithium ions compared to the stretching modes of phosphate which is supported by infrared measurement for v_4 mode and Raman measurements for v_2 mode. Phosphate bending modes are more localized compared to its stretching counterparts; therefore, even small changes in a unit cell can easily affect bending modes. The lithium ion concentration does not have any effect on the frequencies of vibrational modes. $Li_3Ti_2(PO_4)_3$ bands are only observed in infrared measurement while they are not observed in Raman measurements despite the fact that lithium ion cage modes are Raman active modes. This is because such vibrations usually bear small polarizability. Therefore, lithium ion cage modes do not generate enough Raman intensity [44], which would make it really difficult to study the lithium ion conduction pathways via Raman spectrometry.

2.2. Lithium aluminium titanium phosphate (LATP)

The NASICON-type lithium aluminium titanium phosphate (LATP) is obtained via partial substitution of titanium in $LiTi_2(PO_4)_3$ by aluminium cation, with the chemical formula of $Li_{1.3}Al_{0.3}Ti_{1.7}(PO_4)_3$. Since the discovery of LATP [45], several different synthesis techniques of LATP has been reported and the resulting samples exhibit some different ionic conductivity values: cold press and sintering route [46]; sol-gel synthesis route [47][48][49][50][51][52], Sol-gel and colloidal crystals [53], solid state reaction method [51][54] , glass-ceramic route [55][56], rapid quenching method (explosion method) [57], mechanical milling method [58][59], spray granulation method [60] and tape casting method [61].

All different synthesis methods of LATP have their advantages and disadvantages. For example, solid-state synthesis route is more appropriate for mass production. On the other hand, that method suffers from the contamination and/or formation of excessive amount of secondary phases. Sol-gel synthesis route may solve the aforementioned problems of the solid-state synthesis route; however, it has the drawbacks of using toxic and flammable solvents like ethanol, acetylacetone and methanol. Use of such chemicals may pose a risk for the environmental safety and also complicates the mass production.

In the case of partial substation of *M* trivalent metal ions in NASICON-type $Li_{1+x}M_xTi_{2-x}(PO_4)_3$ lithium-conducting solid electrolytes, researchers Aono *et. al.* [30] did not see an influence of the ionic radius; however, attributed a lot of contribution to the increased conductivity to the increased density of the pellets and also the increase in the amount of lithium ion concentration. During the partial substitution of titanium in $LiTi_2(PO_4)_3$ by aluminium, anisotropic linear decrease in lattice constants was observed with an accompanying increase in aluminium content until x = 0.4 since the ionic radius of aluminium cation is smaller than titanium radius. The hexagonal $R\bar{3}c$ structure has highly anisotropic thermal expansion and also on lithiation [38]. The observed stoichiometric limit in Aono`s

report for a single-phase formation was x = 0.3. Until that point, an increasing conductivity was observed with an increase in x. However, a secondary phase was formed for x > 0.4, where conductivity commenced decreasing. Furthermore, substitution limit of T^{4+} by Al^{3+} was found to be around x = 0.4 [30]. Moreover, no correlation was observed at all between conductivity and variation of cell constants via aluminium substitution. In general, three different types of systems were examined: $LiTi_2(PO_4)_3$, $LiTi_2(PO_4)_3$ + $Li_3M_2(PO_4)_3$ mixed phase system and $Li_{1+x}M_xTi_{2-x}(PO_4)_3$ single phase system [30], conductivity is increasing in the given order. For the case of mixed phase system, the main conductive part is $LiTi_2(PO_4)_3$ and secondary phase $Li_3M_2(PO_4)_3$ has a relatively low conductivity [30][45]. Lithium ion transport properties of NASICON-type solid-state electrolytes $Li_{1+x}Cr_xTi_{2-x}(PO_4)_3$ and its aluminium substituted analogue $Li_{1.4}Al_xCr_{0.4-x}Ti_{2-x}(PO_4)_3$ were studied by Zhang *et al* [47]. They observed an enhancement in the lithium ion conductivity of samples after partial substitution of chromium by aluminium and they attribute this enhancement mainly to the decrease of the grain boundary resistance.

Within the crystal structure, the lithium ion diffusion along the pathways is affected by size of bottlenecks. Therefore, the increase in lithium-ion conductivity in the substituted systems was also attributed to the modification of the bottlenecks of lithium ion conduction and an elevation in the mobile lithium ion concentration in some studies [62][63][64]. Juarez *et. al*. [65] also studied the effect of partial substitution. They found that the activation energy of lithium ion conduction depends strongly on the bottleneck size between M1 and M2 sites as well as to the interactions of lithium–lattice and/or lithium–lithium.

On the other hand, Nuspl *et al.* [66] carried out molecular dynamics (MD) simulations that shows substituting titanium via aluminium can only slightly influence the activation energy of lithium ion transport. Hong et *al.* [67] shows that the diameter of the narrowest bottleneck calculated from the discrete oxygen positions must be bigger than twice the sum of radii of mobile ion and oxygen ion

for high ionic conductivity. Nairn *et. al.* [68] and Forsyth *et. al.* [69] revealed via Nuclear magnetic resonance spectroscopy (NMR) studies that some of the substituted aluminium ions take their position in the tetrahedral sites rather than locating at Ti^{4+} site 12c. This can result in the formation of a glassier phase and elevated sinterability. Takada et al. [70] and Forsyth et al. [69] compared LTP and LATP in their NMR reports, and they found that the partial substitution of titanium by aluminium only paves way to some small changes in the line widths, that shows that only a small effect of aluminium content on the lithium ion conductivity of LATP samples.

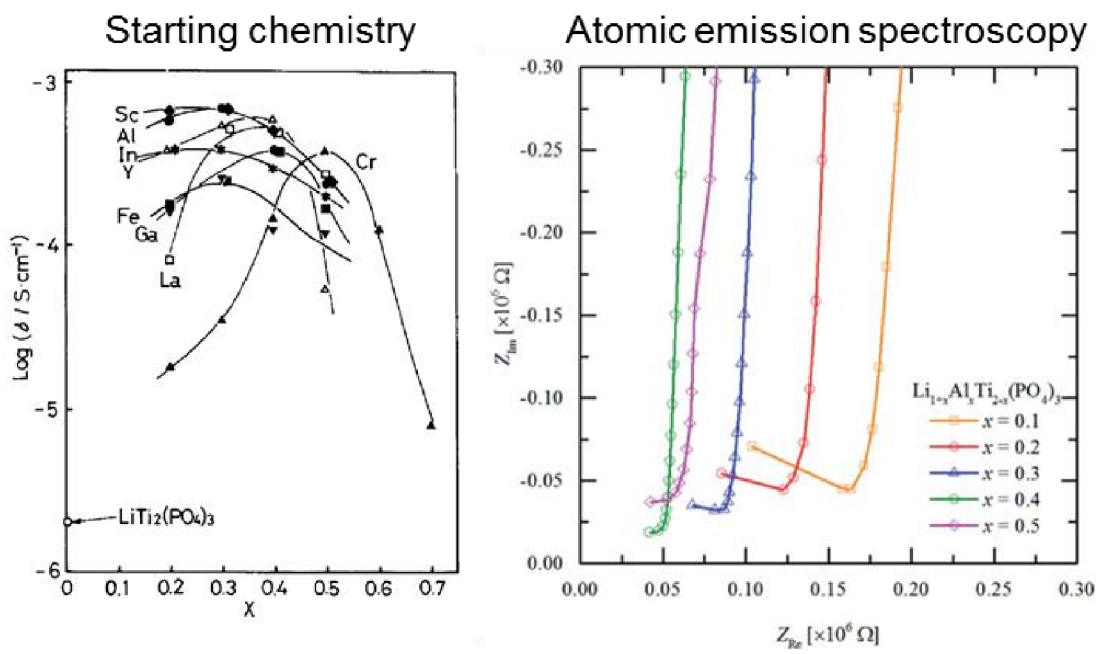

Figure 2.2: Effect of aluminium content x on lithium-ion conductivity studied by starting material chemistry [30] and also by atomic emission spectroscopy [71].

Recently, the increase in conductivity on substituting titanium by aluminium in $Li_{1+x}Al_xTi_{2-x}(PO_4)_3$ was shown independently on microstructural effects on single crystals by using micro-contacting reaching a maximum at x = 0.4 [57]. They

measured the chemistry of the system via atomic emission spectroscopy shown in Figure 2.2.

The lithium ion diffusion pathways within the $Li_{1.3}Al_{0.3}Ti_{1.7}(PO_4)_3$ crystal structure was also recently revealed by high-resolution synchrotron and neutron powder diffraction to be along paths connecting Li1 (6b) and Li3 (36f) sites [72][40]. Lithium-ion diffusion pathways within LATP proposed by Monchak *et. al.* is given in Figure 2.3. This structure [72] differs from another one proposed for $Li_{1.2}Al_{0.2}Ti_{1.8}(PO_4)_3$ only in the positions of the excess lithium which in this case should occupy the 6a site instead of 36 f [39]. Redhammer *et al.* reports that in LATP titanium replacement scales very well with aluminium and lithium incorporation. Additional lithiums position at the M3 cavity and these partially occupied sites are considered as responsible for increased lithium ion conductivity in LATP compared to LTP.

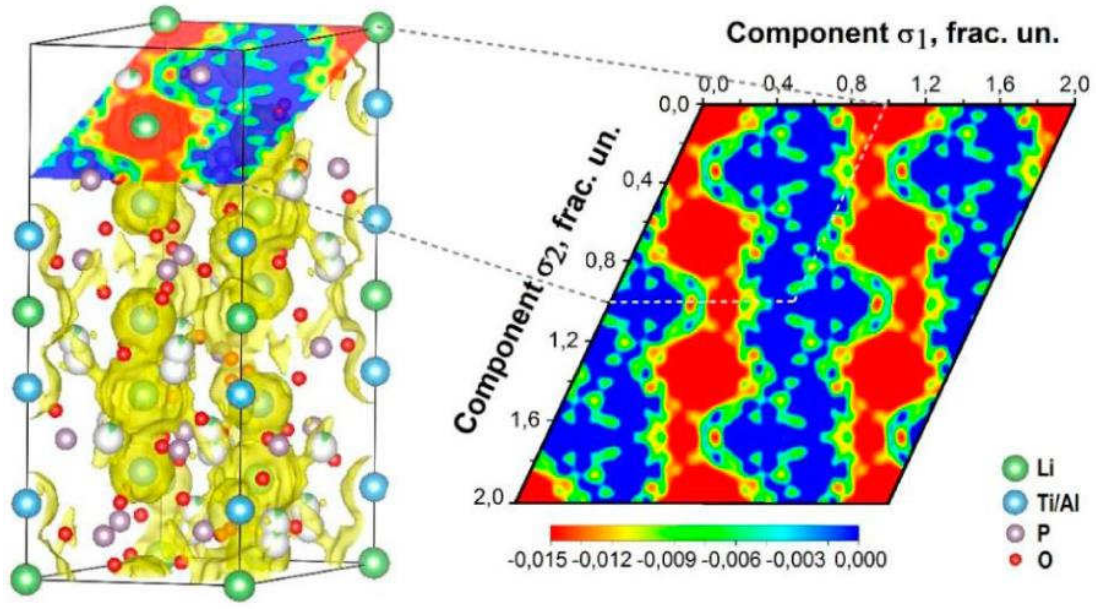

Figure 2.3: Lithium-ion diffusion pathways within LATP [72].

Generally, the total conductivity in polycrystalline ceramics is determined by both, the 'bulk' (intragrain) conductivity σ_g and the grain-boundary conductivity $\sigma_{g.b}$. Depending on the ratio of those conductivities, conduction paths are either through grains and across grain boundaries for $\sigma_g >> \sigma_{g.b}$ or along grain boundaries for the opposite case $\sigma_g << \sigma_{g.b}$. For the system studied in our case already Aono *et al.* [6] reported high grain conductivity. Exploiting impedance analytical data, the impact of grain boundaries on the total ionic conductivity can be estimated in terms of a '*brick-layer*' model (BLM) [73][74]. In its most basic form, however, the BLM assumes a rather idealized microstructure with uniform cubic shaped grains separated by thin grain boundaries and main required inputs are grain size and grain boundary thickness. For highly resistive grain boundaries Fleig tried to adapt the BLM to non-ideal microstructures by introducing insulating secondary phases in part of the grain boundary which is then included by the contact ratio, which describes the ratio of direct grain to grain contacts and the area of contacts blocked by insulating secondary phases [75][76]. In a later work, he also incorporated the non-cubic shaped grains with non-monodisperse grain size [77].

For the present material, impedance measurements give a grain conductivity that exceeds the grain-boundary conductivity by almost three orders of magnitude [78]. Hence, conduction pathways are expected through grains and across grain boundaries. Other groups studied the correlation between microstructure and ionic conductivity in dependence of sintering time for LATP, and best ionic conductivity was observed for short sintering times and small grain sizes [79]. For the poorer conductivity for long sintering times, cracks in larger grains were claimed to be a possible reason by Hupfer *et al.* [79]. Cracks were found to originate at the interface of LATP grains and $AlPO_4$ secondary phase by Waetzig *et al.* [80]. They identified two different mechanisms leading to crack formation. Firstly, at the sintering temperature of about 950 ^oC, Li_2O vaporization results in the partly phase transition of LATP into $AlPO_4$ secondary phase and oxides. $AlPO_4$ secondary phase was observed to show microcracks due to the lattice shrinkage. On the other hand,

at this temperature, the change in microstructure is not dramatic; therefore, lithium ion conductivity is still high. Secondly, at the sintering temperatures of above 1000 ^{o}C, grain coarsening and thermal expansion anisotropy lead to microcracking. These extreme alterations in microstructure result in a decrease of lithium ion conductivity of samples [80].

High conductivity for small grain sizes was observed in $Na_{1.3}Al_{0.3}Ti_{1.7}(PO_4)_3$ sintered at different temperatures, but the grain/bulk conductivity is smaller for sodium ion compared to lithium ion [81]. Thokchom *et al.* also reported for LATP ceramic samples that smaller grain size and their narrow distribution increases the ionic conductivity. They also observed that most of the $AlPO_4$ secondary phase locates at the grain boundaries [82].

In a more recent work on LATP ceramic samples, Hupfer et al. [50] studied the influence of the addition of small amounts of $LiTiOPO_4$ to LATP and LTP ($Li_1Ti_2(PO_4)_3$) on the microstructure and ionic conductivity. They found 5% addition of $LiTiOPO_4$ as an optimum to limit the amount of $AlPO_4$ non-lithium-conductive secondary phase during sintering, but not fully suppressing its formation to still benefit from the fact that it inhibits abnormal grain growth [50]. A sintering temperature of more than 1100 ^{o}C is required for densification of a pure LTP phase. They found that the addition of $LiTiOPO_4$ to LTP decreases the sintering temperature of pellets, but still a minimum sintering temperature of 1050 °C is needed for the densification of pellets. Also, the addition of $LiTiOPO_4$ to LTP produce more homogenous samples. On the other hand, the addition of $LiTiOPO_4$ to LATP increases the sintering temperature of pellets from around 850 ^{o}C to 900 ^{o}C and leads to inhomogeneity. An improvement of lithium ion conductivity was observed for 5% addition of $LiTiOPO_4$ to LATP. On the other hand, they could not provide any quantitative information about the grain size distributions due to the fact that secondary phase and grains exhibit very similar colour and an automatic separation of these microstructural components were not possible [50]. Aono et al. [83][84] reported the increased densification by

adding lithium salts (Li_3PO_4, Li_2O, $Li_2P_4O_7$) to $Li_3Ti_2(PO_4)$ and LATP which could also assist in increasing grain boundary conductivity. A similar behaviour was observed for LAGP with excess lithium by Chun et al [85].

Duluard *et al.* [86] prepared LATP ceramic pellets via spark plasma sintering and observed the lowest lithium ion conductivity at the sintering temperature of 1000 ^oC. They interpret the decrease in lithium ion conductivity in terms of the lack of cohesion between the large grains. Interestingly, at the other sintering temperatures (850, 900 and 950 ^oC), such a drop in lithium ion conductivity was not observed despite the regions with large grains. Therefore, they conclude that large grains are not deteriorating lithium ion conductivity when small grains are present together with large ones, because small grains provide a better cohesion. They mention that investigations are going on to determine the origin of this phenomenon. On the other hand, a statistical grain size distribution is not available in this study. Another report from the same research group attributes the high lithium ion conductivity of samples to the high purity level of LATP samples, low amount of $AlPO_4$ secondary phase, optimum grain sizes and optimized calcination steps [87].

The effect of powder calcination temperature on the lithium ion conductivity of LATP ceramic pellets was studied by Schell *et al.* Calcined samples are sintered and the highest lithium ion conductivity was observed for the samples calcined at the temperature of 900 °C. In addition to that, quite homogeneous microstructure is observed for these samples.

Kotobuki et al. studied the effect of phosphate source on the lithium ion conductivity of samples. They prepared LATP solid electrolytes by means of coprecipitation using various phosphate sources such as H_3PO_4, $NH_4H_2PO_4$ or $(NH_4)_2HPO_4$. They found that the type of phosphate source has an effect on the sintering behaviour and secondary phase formation in LATP. Therefore, lithium-ion conductivity is also influenced by the starting phosphate source. The LATP ceramic

samples prepared using $NH_4H_2PO_4$ as a phosphate source showed the highest lithium-ion conductivity because these samples did not show impurities and had less grain boundaries, which result in a higher grain to grain boundary volume ratio and decreases the length of lithium ion conduction pathways [88].

One of the problems faced during microstructural studies is the degradation of LATP in the course of water based metallographic sample preparation processes. Therefore, it was aimed to develop a non-water based metallographic sample preparation route so as to make the microstructural characterization of LATP samples possible.

For the LATP ceramic samples sintered at different temperatures, both the grain and overall conductivity changes with increasing sintering temperature, and in order to understand the reason for this behaviour, it is of importance to study the microstructure of LATP ceramic pellets. Therefore, it is aimed to provide a better understanding on the sintering temperature dependent evolution of microstructural properties such as grain size, grain morphology, connectivity of grains, the amount and type of secondary phases and their connection with LATP bulk chemistry and eventually the relation between all these properties and lithium ion transport characteristics of LATP samples. It is aimed to provide an improved microstructural characterization of LATP ceramic pellets via a combined confocal laser scanning and scanning electron microscopy investigation of LATP. Use of a correlative microscopy in the investigation of LATP ceramics was reported by us before via a correlative SEM-AFM approach [89]. However, a combined SEM-CLSM approach allows a statistical study of LATP ceramics and their sintering temperature dependent evolution.

In the presence of more than one secondary phase and pores, image analysis must tackle the difficulties about distinguishing between these microstructural features. So as to overcome such difficulties, it is aimed to develop novel image segmentation and phase map reconstruction recipe for quantitative phase map

analyses which utilizes high quality Energy-dispersive X-ray spectroscopy (EDS) maps. These microscopic techniques are employed to provide a better understanding on the sintering temperature dependent evolution of different phases, their relationship with the LATP bulk chemistry and their overall correlation with the lithium ion conductivity of LATP samples retrieved from impedance analyses.

Chapter 3 : Experimental methods

The aim of this chapter is to describe the methods used in the synthesis, metallographic sample preparation and characterization of LATP ceramic pellets. The main focus is on the combined microscopy techniques. Descriptions of all these methods can be found below.

3.1. Pellet fabrication

LATP-powders were synthesized by an oxalic acid supported conventional sol-gel method. In the synthesis route, 25mL of $Ti(OC_3H_8)_4$ ($\geqslant$ 97.0%) was mixed with 50mL NH_4OH (Sigma-Aldrich, 28-30% solution), which then produced a white gelatinous precipitate. The precipitate was cleaned with a large amount of deionized water to get rid of the excess base and put into 100 mL of deionized water ($\geqslant$ 99.9%). 200mL of 1M oxalic acid (Sigma-Aldrich, 99.9%) was added into this solution, which produced a clear solution of $H_2[TiO(C_2O_4)_2]$. Stoichiometric $Al(NO_3)_3 \cdot 9H_2O$ ($\geqslant$ 98.0%)(Sigma-Aldrich), $(NH_4)_2HPO_4$ ($\geqslant$ 98.0%)(Sigma-Aldrich) and 5% excess $LiCOOCH_3 \cdot 2H_2O$ ($\geqslant$ 98.0%)(Sigma-Aldrich) were dissolved in water added into the $H_2[TiO(C_2O_4)_2]$-solution in a slow manner so as to clear it under stirring. The final solution was then heated on a hot plate at 60 ^oC overnight under very strong stirring. Finally, the temperature was elevated to 140 ^oC until the evaporation of water takes place giving a white precipitate of well mixed precursors for annealing. Afterwards, precursors were ground. The mixture was then pre-annealed in the air for 5 hours at 850 °C with the heating rate of 100 °C per an hour. Holding time and heating rate was optimized according to phase purity and lithium ion loss.

The pre-annealed $Li_{1.3}Al_{0.3}Ti_{1.7}(PO_4)_3$ powder was first ground, filled into dies and uniaxially pressed to cylindrical pellets of 10 mm diameter with 20 kN. Subsequently, the pellets were densified by cold isostatic pressing for 10 s at 1425 kN. These pellets were sintered in the air atmosphere for 8 hours at different

temperatures from 900 °C to 1100 °C in 50 °C steps. Ceramic pellets were covered with a parent powder in order to avoid from lithium-ion loss as well as contamination from the crucibles.

3.2. Grinding and polishing procedure

3.2.1. Grinding

For microscopic investigations, LATP ceramic pellets were firstly glued on the top of the moving part of the sample holder with crystal bond. Grinding is the first step to be taken during the course of mechanical material removal.

When carried out in a proper manner, with grinding, it is aimed to remove deformed/damaged surface material at the same time hedging the possible extra surface deformation. The purpose is to reach well-defined plane surface. Fixed abrasive particles that can produce chips of the samples are employed. Using sharp abrasive grains provide the highest removal rate. During the course of grinding, firstly, the grains of the abrasive material, which are glued to sandpaper surface, get in contact with the sample surface. Formation of chips starts when abrasive grains enter the sample. As the grinding procedure continues, the chip removed from the sample surface grows. Finally, abrasive grains leave the sample surface the resulting in some scratches in the sample surface.

Due to the fact that LATP ceramics are water sensitive, water is not used in any of the grinding steps. Rather, grinding routes based on oil are developed and optimised which would allow differentiating the microstructural components clearly. Initially, samples are ground with 15 µm (FEPA-Norm 1200), 10 µm (FEPA-Norm 2400) and 5 µm (FEPA-Norm 4000) silicon carbide (SiC) sandpapers, in the respective order with a commercially available oil-based lubricant solution (Cloeren Technologies). In order to get rid of the deformed/damaged part of the sample surface, at least three times of the size of the respective sandpaper was removed

from the sample surface. The amount of the removed sample surface can easily be checked via the reading of the micrometre screw of the sample holder.

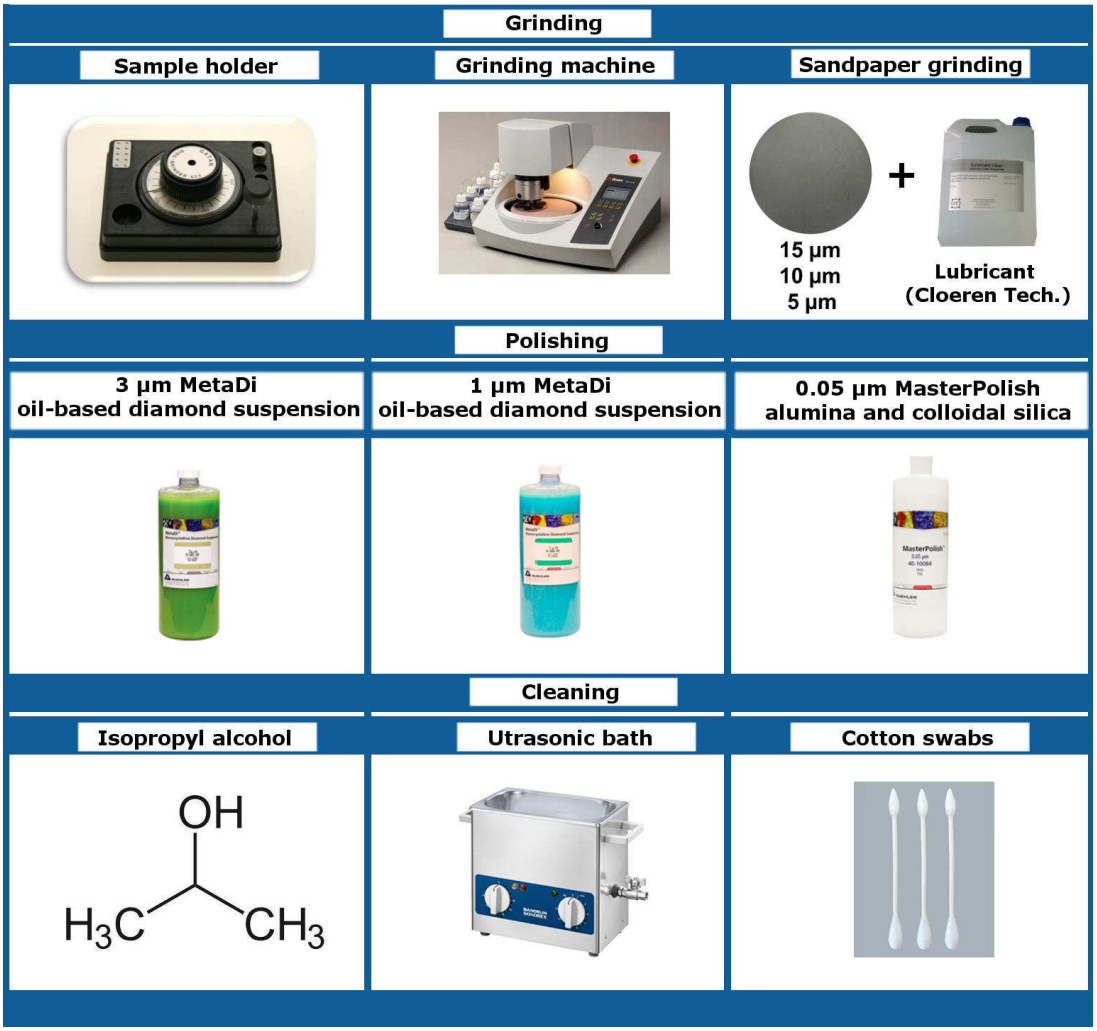

Figure 3.1: The sample preparation route in the respective order from top to bottom and left to the right.

3.2.1. Polishing

Similar to grinding, polishing is also used to remove the damage/deformation staying from the previous steps of grinding/polishing. Polishing is the last finishing processes for smoothing a sample surface. The use of water is avoided during the

course of polishing likewise the grinding steps. For polishing, a smaller chip sizes are considered so as to get a sample surface without scratches and damage/deformation or at least with a minimum amount of them. Therefore, unlike grinding procedure, more resilient polishing clothes were employed. To start with, polishing was applied with oil-based diamond suspensions with particles sizes of 3 µm and 1 µm (Buehler, MetaDi, oil based) in order to approach the chip size of near zero.

In the last polishing step, a water-free suspension of a blend of high-purity alumina and colloidal silica with a particle size of 0.05 µm (Buehler, MasterPolish) was used. It is important to keep the force applied on the sample holder as low as possible to keep the chip sizes approaching to almost zero.

After polishing procedure is completed, the samples were cleaned under pure isopropyl alcohol in an ultrasonic bath for 10 minutes, and then they were wiped with cotton swabs thoroughly and meticulously. This sample preparation route is schematized in Figure 3.1 with a respective order from left to right and top to bottom.

3.3. Impedance spectroscopy

Both sides of LATP samples were coated with a gold layer of 450 nm thicknesses using a sputter coater (BAL-TEC SCD 050, Balzers, Germany). Impedance measurements were carried out using a potentiostat (VSP-300 potentiostat, Bio-logic Science Instruments, Claix, France) at an excitation amplitude of 5×10^{-3} A from $f = 3 \times 10^{6}$ Hz to $f = 1 \times 10^{2}$ Hz.

3.4. Microscopy

3.4.1. Optical microscopy

Optical microscope, which is also usually called as the light microscope, is a type of microscope which employs visible light and also a set of lenses in order to enlarge small objects via angular magnification, providing the user a magnified virtual image. In this study, optical microscope feature of Olympus LEXT (OLS4100, Japan) was used to retrieve initial information on the polished samples.

3.4.2. Confocal laser scanning microscopy

The Confocal laser scanning microscopy (CLSM) is an optical imaging and characterization technique. It is used to increase the optical resolution and contrast of images via employing a spatial pinhole so as to block light which is out of focus during the course of image formation.

It is quite similar to a conventional optical microscope. However, in a conventional microscope the whole sample is illuminated. CLSM allows taking many two-dimensional micrographs with different depths in specimens, and using them to reconstruct three dimensional structures, this is called as optical sectioning. Despite some of its similarities with light microscopes, there are some main differences. In CLSM, laser light has a 405 nm wavelength while a conventional optical microscope uses visible light with a wavelength of 550 nm. Therefore, CLSM allows a highly controlled and limited depth of focus.

A 3D measuring confocal laser scanning digital microscope (CLSM) (Olympus LEXT OLS4100, Japan) was employed to carry out microstructural investigations on polished samples. High-resolution images were recorded with 50x and 100x objective lenses, which both have a numerical aperture of 0.95. A suitable sample holder was prepared in a metal lathe to put the samples that were previously glued

on top of stubs. In this manner, the goal is the keep the samples during the course of CLSM imaging.

3.4.3. Electron microscopy

Unlike the light microscopes which employ light to illuminate, the source of illumination in electron microscopes is an accelerated particle beam of electrons. Electron microscopes are capable of providing higher lateral resolving capability than light microscopes because of the fact that the wavelength of an electron is up to a hundred thousand times shorter compared to that of visible light photons. At an acceleration voltage of 10 kV, electron wavelength is equal to 0.0122 nm. This feature of electron microscopes allows the detection of smaller objects during the course of imaging. In all types of electron microscopes, electromagnetic and/or electrostatic lenses are employed in order to determine the path of electrons and also to focus them to form an image because glass lenses, used in light microscopes, would have no effect on the electron beam at all. Electromagnetic lenses are designed as solenoids. This paves the way for the magnification up to two million times.

When electrons move faster, their wavelengths are shorter. The resolution capability of a microscope depends directly on the wavelength of the irradiation employed to for the formation of images. Observing sub-wavelength structures using microscopes is difficult due to the Abbe diffraction limit. Resolution in optical microscopy is limited by wavelength. On the other hand, electrons have shorter wavelength. For a typical SEM operating at 10 kV, electron wavelength is equal to 0.0173 nm while for a typical TEM operating at 200 kV, electron wavelength is equal to 0.0027 nm. As the wavelength of the irradiation decreases, the resolution of the images increases. Therefore, once the accelerating voltage of the electron beam is increased, the resolution of the electron microscope is increased as well. On the other hand, electron wavelength is much lower than the resolution limit, which is determined by quality of the lenses, and also how much the beam can be

focused which depends on the accelerating voltage and also the current, this effect is named as Boersch effect.

There are two main types of electron microscopes, which are called as Scanning electron microscopy (SEM) and Transmission electron microscopy (TEM). These two types of EMs are described below.

3.4.3.1. Scanning electron microscopy

Scanning electron microscopy (SEM) is a type of an electron microscope that operates via rapidly scanning a focused electron beam over the sample. This scanning takes place through a rectangular area of the samples, which is called as raster scan. There are various mechanisms which can take place when the electron beam interacts with the samples. This leads electrons to be scattered from surface of samples.

The volume inside the sample going into interaction with electrons is called as the interaction volume. This is naturally three dimensional and depends on several factors such as beam energy, material parameters as well as specimen tilt. On the other hand, the so-called electron range is used to describe interaction volume with a single parameter, which is an estimate number [90]. Kanaya *et. al.* parametrizes the electron range as the following equation [91]:

$$R_{KO}\ (\mu\mathrm{m}) = \frac{0.0276A}{Z^{0.89}p} E_0^{1.67} \qquad (3.1)$$

where A is the atomic weight (g/mole), Z is the atomic number, ρ is the density (g/cm^3), E_0 is the beam energy (keV), 0.0276 is a constant and R_{KO} is the electron range in microns. For the case of $Li_{1.3}Al_{0.3}Ti_{1.7}(PO_4)_3$, the molecular weight in g/mole is calculated as following:

$$MW(LATP) = 1.3M(Li) + 0.3M(Al) + 1.7M(Ti) + 3M(P) + 12M(O) \qquad (3.2)$$

when the atomic weights, Li (6.941), Al (26.9815), Ti (47.867), P (30.9738) and O (15.9994) are put into the equation 3.2, molecular weight of LATP is retrieved as:

$$MW(\mathrm{Li_{1.3}Al_{0.3}Ti_{1.7}(PO_4)_3}) = 383.4058 \quad (3.3)$$

Here the equation 3.1 deals with a compound rather than an element; therefore, effective atomic number Z_{eff}, which is a weighted average, is used:

$$\mathrm{Z_{eff}}(LATP) = \frac{1.3Z(Li) + 0.3Z(Al) + 1.7Z(Ti) + 3Z(P) + 12Z(O)}{1.3 + 0.3 + 1.7 + 3 + 12} \quad (3.4)$$

When the related atomic numbers are put into the equation 3.4, it becomes:

$$\mathrm{Z_{eff}}(LATP) = \frac{1.3(3) + 0.3(13) + 1.7(22) + 3(15) + 12(8)}{1.3 + 0.3 + 1.7 + 3 + 12} \quad (3.5)$$

$$\mathrm{Z_{eff}}(LATP) = 10.1749 \quad (3.6)$$

For the LATP ceramic sample sintered at 1100 °C, the sample density was 2.77 g/cm^3[92]. Therefore, for a measurement with the beam energy (E_0) of 10 kV, one can now calculate the electron range (R_{KO}) with the formula given in 3.1:

$$R_{KO}\ (\mathrm{Li_{1.3}Al_{0.3}Ti_{1.7}(PO_4)_3})(\mu\mathrm{m}) = \frac{(0.0276)(383.4058)}{(10.1749^{0.89})(2.77)}(10^{1.67}) \quad (3.7)$$

$$R_{KO}\ (\mathrm{Li_{1.3}Al_{0.3}Ti_{1.7}(PO_4)_3})(\mu\mathrm{m}) = 22.6665 \quad (3.8)$$

Strong Coulomb interaction of the electrons with the positive potential of the atom core leads to the Backscattered-Electrons (BSE). There is a correlation between the amount of the backscattered electrons hitting the detector and the atomic number Z. Therefore, this correlation is useful to distinguish between different phases of different density [90]. On the other hand, BSE imaging can also provide information on the other properties of samples such as crystallography, topography and magnetic field of the specimen.

For the detection of backscattered-electrons, mainly solid-state detectors are used; they mainly have p-n junctions. They operate based on the formation of electron hole pairs by the backscattered-electrons that leave the sample and hit the detector. The current correlates to both the energy and the number of backscattered-electrons. The position of the BSE detectors is above the sample, arranged in a "doughnut" type with separate part which are symmetric, in order to maximize the solid angle of collection of the backscattered electrons.

The most common imaging mode is the detection of secondary electrons (SE). Secondary electrons hit out of the electron cloud (mainly the k-shell) of the atom and have energy < 50 eV. Therefore, they only arise from the surface and give topographic contrast. For the detection of secondary electrons, the Everhart-Thornley detector [93] is the most generally employed device. It is normally positioned at one side of the chamber to increase their efficiency. The Everhart-Thornley detector has a scintillator inside a Faraday shield. This is positively charged and captures SE. This scintillator inside the Faraday shield is used to accelerate electrons and when these accelerated electrons have enough energy, they lead scintillator to emit light.

Energy-dispersive X-ray spectroscopy (EDS) is both a qualitative and quantitative microanalytical method employed for the elemental analysis and/or chemical characterization of specimens. Its working mechanism mainly depends on the interaction of X-rays and specimens. Electrons from primary electron beam penetrate the specimen and X-rays are produced because of that interaction. Since each element has a different unique atomic structure, each element exhibits different peaks on its electromagnetic emission spectrum. In this thesis study, EDS is used at the accelerating voltages of 5 kV and 10 kV.

To gather correlative microstructural and chemical information from polished LATP ceramic specimens, samples were analysed using Scanning electron microscopy (SEM) (Quanta FEG 650; FEI part of Thermo Fischer, Hillsboro, Oregon,

USA) equipped with field emission gun (FEG) and Energy-dispersive X-ray spectroscopy (EDS) (Octane 60 mm², EDAX Inc., Mahwah, NJ, USA).

3.4.3.2. Transmission electron microscopy

Transmission electron microscopy (TEM) is a microscopy technique where an electron beam is transmitted through a sample to form an image. TEM has some main components: First is the electron gun, where electron beam is produced; and the condenser system which focuses the beam; second is the image producing systems including objective lens, specimen stage; third is the image-recording systems including fluorescent screen and digital camera. TEM samples are usually ultrathin sections with a thickness less than a hundred nm or a suspension on a grid. A micrograph is formed via the interaction of the sample with the electrons as the electron beam is transmitted through the sample.

Scanning transmission electron microscope (STEM) is a type of TEM. In STEM, the microscope lenses are adjusted in a manner to form a focused convergent electron beam at the sample surface. This is a small spot of size 0.05 - 0.2 nm. It is then scanned through the specimen in a similar way to SEM; however, the sample is thin TEM section. Therefore, no underlying volume is probed unlike in SEM.

For the TEM experiment done by Roland Schierholz, a lamella was cut out of an SEM sample using focused ion beam (Helios nanolab 460 F1, FEI part of Thermo Fisher, Hillsboro, Oregon, USA) [94]. TEM experiments were conducted at 200 kV with a Tecnai G2 F20 (FEI part of Thermo Fisher, Hillsboro, Oregon, USA) [95].

Chapter 4 : Correlative confocal laser scanning microscopy and scanning electron microscopy of LATP

In this chapter, I report on a combined confocal laser scanning and scanning electron microscopy investigation of polished LATP samples, sintered at temperatures of between 950 and 1100 ^{o}C with 50 ^{o}C intervals to provide an improved microstructural characterization and a better understanding on the temperature dependent evolution of LATP. TEM imaging was done by Roland Schierholz, and impedance results were provided by Shicheng Yu and Andreas Mertens.

4.1. Microstructural components

4.1.1. CLSM

In order to distinguish all relevant microstructural components, a combined confocal laser scanning (CLSM) and scanning electron microscopy (SEM) approach was applied. SEM is the standard technique for the characterization of materials, as it provides reasonably high lateral resolution and field of view and the capability of chemical analysis. On the other hand, CLSM does not require high vacuum, does not reduce the sample and is capable of easily identifying pores by its high resolution in the z-direction. Therefore, relatively high-magnification studies and chemical analysis have been carried out via means of SEM while both low and high magnification micrographs were taken by CLSM.

The crystalline structure of the main phase was shown to be consistent with the R-3c structure (ICSD No. 427619, [39]) proposed for LATP by X-ray diffraction on the same material [90]. The CLSM micrograph in Figure 4.1 (a) of the LATP sample sintered at the temperature of 1100°C displays LATP grains with a bright contrast,

an intergranular phase with intermediate grey level contrast (light gray areas), and black and dark gray pores. In some regions Newton's rings are also observed which might arise due to the different path length light follows in the sample. This path difference can be due to closed porosity and imperfections in the sample surface flatness.

The two lines in Figure 4.1 (a) mark the position of the line profiles in Figure 4.1. These two profiles clearly reveal that the light gray areas and the grains are in the same plane while the black and dark gray areas have significantly different height than the polished surface. Therefore, both could be assigned to pores of different height. However, also a second secondary phase might be present and the height difference might arise due to preferential etching of another phase during polishing [96]. Accordingly, although the CLSM data allows to determine height maps as shown in Figure 4.1 (c), a confident determination of the amount of porosity and the second secondary phase is difficult. On the other hand, in the height map, the red line stays below 0.2 µm even if it passes through the dark gray region; therefore, if one sets the threshold to 0.2 µm it should not count as porosity. Via employing the image matrixes of the height maps, it is possible to check which percentage of a matrix is composed of elements below certain threshold. In this way, it is possible to provide quantitative values for the porosity of LATP ceramic samples. For this, a MATLAB script was used, which uses an image matrix as an input and returns the porosity in percentage. This script is provided in the appendix. Quantitative values for the porosity are retrieved via image matrix analysis of the regions given in the Figure 4.10. Results are tabulated in Table 4.1.

Formation of secondary phases manifests in contrast differences for regions with similar height (e.g. top right corner and blue line profile) owing to different reflectivity compared to LATP. With careful adjustment of the thresholds it is possible to distinguish grains and the light grey secondary phase which I attribute to $AlPO_4$.

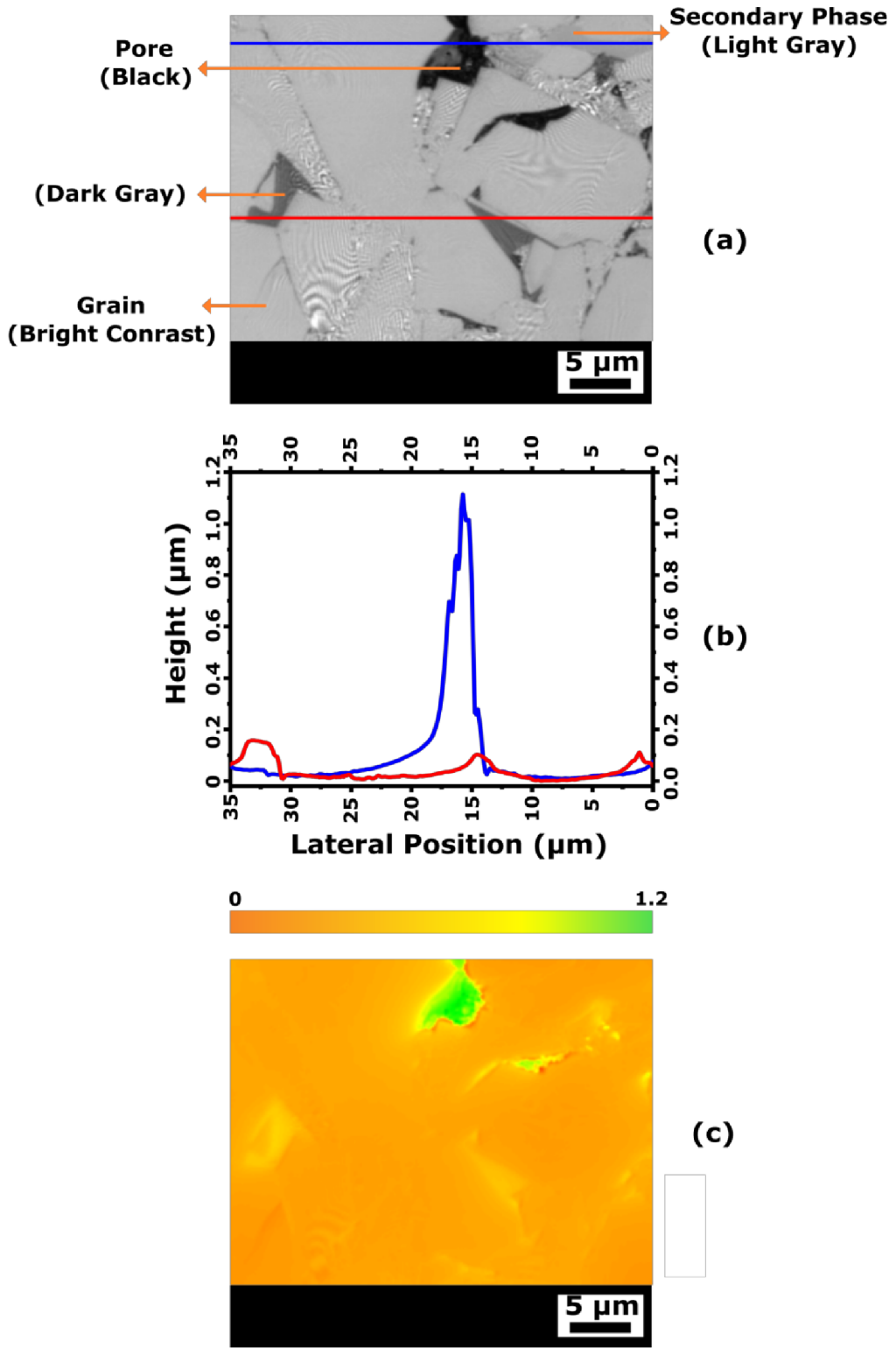

Figure 4.1: (a) CLSM micrograph of LATP pellet sintered at 1100 °C, (b) Depth profiles of the red and blue lines in (a), (c) Height map of the respective LATP pellet sintered at 1100 °C.

Table 4.1: Porosity of samples. To differentiate the pores from dark gray regions (a second secondary phase), only regions below some certain threshold is considered as porosity.

Porosity (%)						
Z threshold/ Sintering temperature	0.1 µm	0.2 µm	0.3 µm	0.4 µm	0.5 µm	0.6 µm
950 °C	2.8	1.1	0.5	0.2	0.1	0.1
1000 °C	6.8	2.4	1.0	0.6	0.4	0.3
1050 °C	16.9	6.7	3.5	2.0	1.4	1
1100 °C	6	4.7	4.0	3.4	3.0	2.6

4.1.2. Comparison of CLSM and SEM

In Figure 4.2, Correlative SEM (top) and CLSM (middle) micrographs as well as a CLSM height map (bottom) of a polished LATP ceramic sample with the sintering temperature of 1050°C is shown. In both CLSM and SEM micrographs, LATP grains exhibit a bright contrast and secondary phase regions show a light gray colour that we assigned to $AlPO_4$. On the other hand, some areas which appear quite dark in CLSM micrograph seem to contain material in SEM micrograph. A close up of such an area is shown in Figure 4.3. In the blue circle in Figure 4.3, the $ALPO_4$ seems well connected to the surrounding grains, so it might aid on densification of the material as discussed in literature [44]. Morphologically, the secondary phase appears intergranular, which is rather an evidence for an amorphous structure in contrast to the findings by XRD [43][37][80].

Cracks within LATP grains are also observed in grains not directly connected to AlPO4. Waetzig *et al.* [80] stated that cracks in LATP originate from $AlPO_4$. At the

sintering temperatures of above 1000 °C, they observed extreme changes in the microstructure with large grains and cracks through the main and secondary phase originating from the grain growth of main LATP phase and the thermal expansion anisotropy. As result, the density and conductivity are reduced. In Duluard's report, for the LATP ceramic pellets prepared by spark plasma sintering, large grains together with small grains were observed at the sintering temperatures of 850, 900 and 950 °C [86]; however, only large grains remained at the sintering temperature of 1000 °C. This is also the temperature where they observed a decrease in lithium ion conductivity. Therefore, they conclude that large grains do not hinder lithium ion conductivity as long as they exist together with small grains since small grains provide a better cohesion among larger ones. On the other hand, they mention that underlying reason of this phenomenon is not clear and under investigation [86]. They also attribute the high lithium ion conductivity of samples to low amount of $AlPO_4$ secondary phase, high purity level of LATP ceramic samples, optimum grain sizes and optimized calcination steps [87].

In a report by Kotobuki et al. the influence of different phosphate source on the lithium ion conductivity of LATP ceramic samples were investigated via a coprecipitation method. H_3PO_4, $NH_4H_2PO_4$ or $(NH_4)_2HPO_4$ were employed as phosphate source. When $NH_4H_2PO_4$ used as phosphate source, highest lithium-ion conductivity is observed since these LATP ceramic samples did not exhibit impurities and had less grain boundaries. This increases the grain to grain boundary volume and shortens the lithium ion conduction pathways [88].

Other secondary phases such as TiO_2, which should appear with a bright contrast, as reported in the literature [41][42][46][49][80] were not observed in our case, neither by EDS nor by BSE or CLSM imaging, where they should appear with a brighter contrast than the LATP grains.

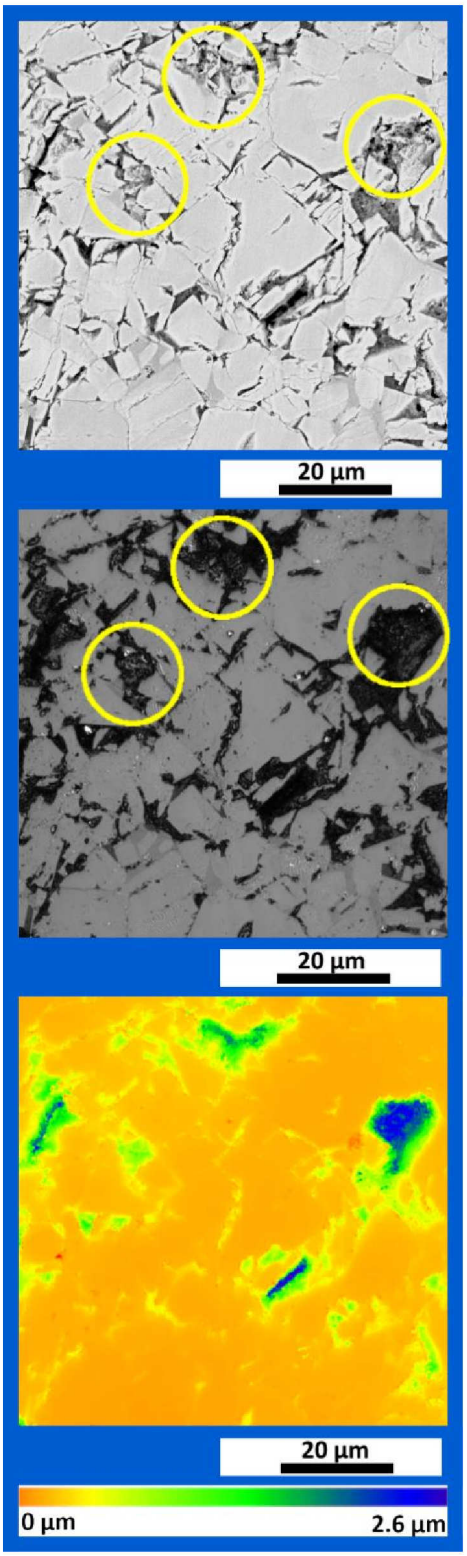

Figure 4.2: Correlative SEM (top), CLSM (middle) micrographs and a height map (bottom) from the same positions of the LATP sample sintered at a temperature of 1050°C.

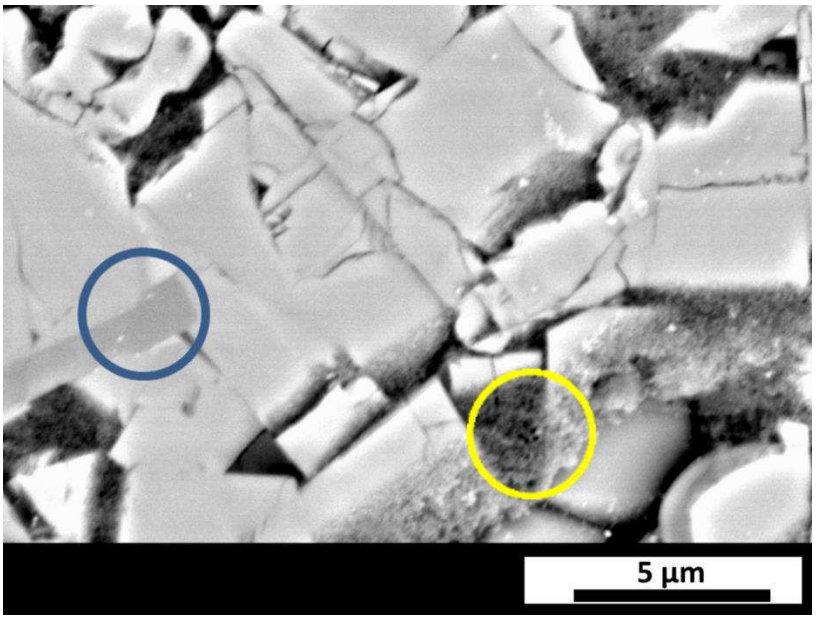

Figure 4.3: A higher-magnification SEM-micrograph of the same sample showing dense secondary phase in the blue circle and the accumulated polishing particles in the yellow circle.

4.1.3. TEM

TEM investigations support the abovementioned results as amorphous regions in triple points were observed frequently as shown for LATP sintered at the temperature of 1000°C in Figure 4.4 (a). In addition to this, part of the grain boundary shows a thin film with amorphous contrast in high-resolution TEM micrographs as shown in Figure 4.4 (b) at the right side. Grain boundaries vary in width and no significant difference could be observed between the different samples. With the small sampling area of TEM, no grain boundary width distribution can be extracted from the data. Especially for the higher sintering temperatures with larger grain sizes only part of a single grain boundary can be investigated per TEM sample. Also, the preferential etching of grain boundaries and secondary phases during TEM sample preparation is a problem. Therefore, quantitative values for the grain boundary width distributions cannot be given. Wetted fraction of grain boundaries for a more detailed determination of the

contact ratio cannot be given as well. As can be seen in Figure 4.4 (a) the film does not occur along the full length of this grain boundary neither in the grain boundary in the lower right part of Figure 4.4 (a). On the other hand, the grain boundary above the triple point in the upper right part shows such a film.

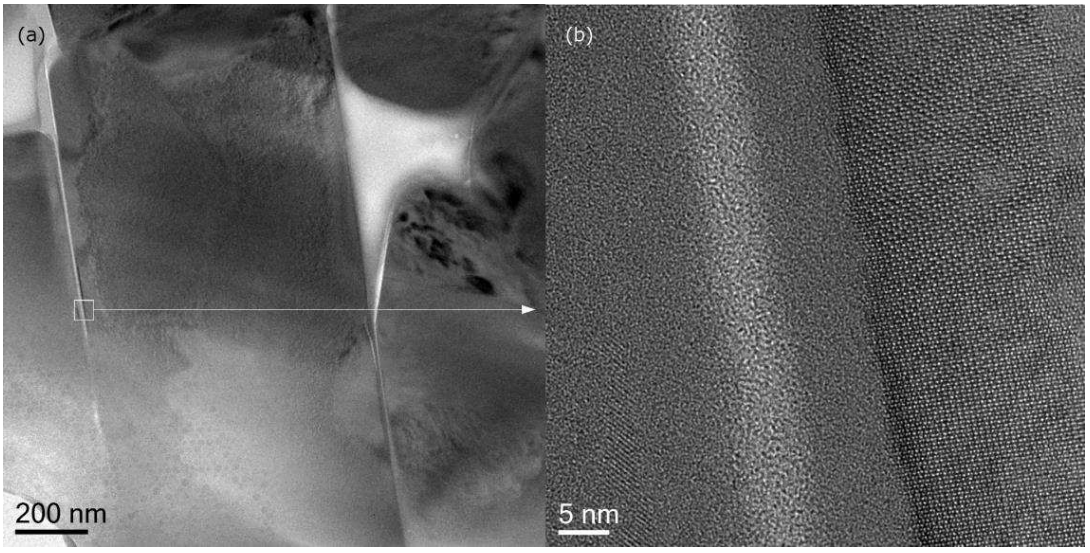

Figure 4.4: (a) TEM-micrograph of LATP sintered at a temperature of 1000°C showing crystalline LATP grains and an amorphous secondary phase. (b) HRTEM-micrograph of the grain boundary in (a) revealing a thin amorphous region at the grain boundary.

4.1.4. Development of microstructure

In this section, it is aimed to discuss the microstructural development of LATP ceramic samples sintered at temperatures of 900, 950, 1000, 1050 and 1100 ^{o}C in a qualitative manner. In Figure 4.5, an SEM micrograph of LATP ceramic sample sintered at 900 ^{o}C is provided. Grains are not compactly connected to each other. This can be because of the minimum sintering temperature threshold required to complete the sintering of the ceramic samples. Before the sintering temperature of 950 ^{o}C, samples look more like a loose powder. Both the CLSM and SEM micrographs of LATP ceramic samples indicate that a minimum sintering temperature of 950 ^{o}C is required to produce fully sintered samples.

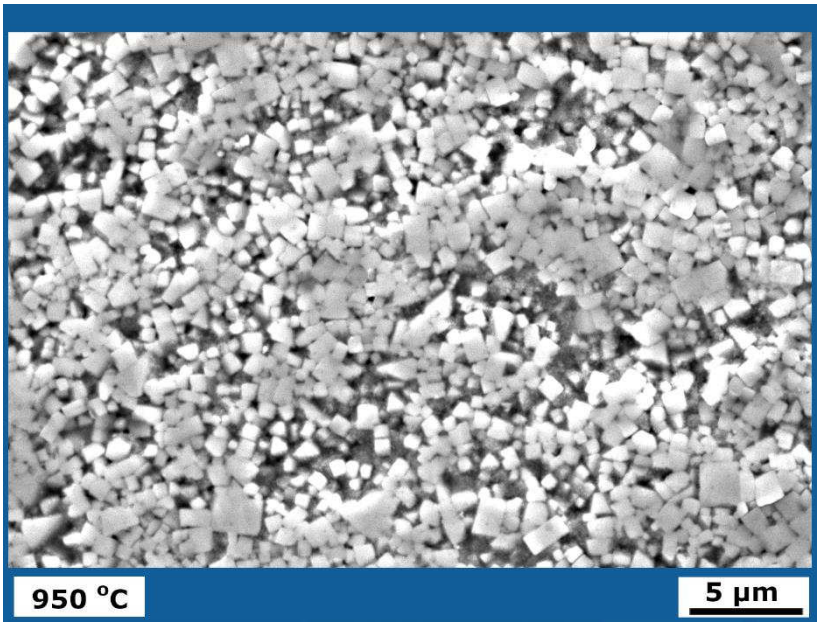

Figure 4.5: An SEM-micrograph of the LATP sample sintered at 900 °C.

Figure 4.6 and 4.7 show the SEM and CLSM micrographs, respectively, of all LATP ceramic samples for the sintering temperatures of between 950 and 1100 °C. The low magnification micrographs were recorded at the same magnification in order to reveal the microstructural changes with increasing sintering temperatures, and drastic changes can be seen. The sample sintered at 950 °C mainly exhibits small grains while some larger grains are present as well. Grains seem to be very well compactly connected. At the sintering temperature of 1000 °C, the size of grains seems to be doubling. It is possible to observe secondary phase regions (light gray areas) with this sintering temperature. The size of the grains as well as the amount and size of secondary phase regions increase at the sintering temperature of 1050 °C while the grain connectedness seems to be decreasing. On the other hand, lithium ion conduction pathways are still probable around secondary phase regions. Both the size and amount of secondary phase seems to be increasing at the sintering temperature of 1100 °C. In addition to this, bulky secondary phase regions

are formed separating some of the grains apart. On the other hand, grains reach the highest size at this sintering temperature.

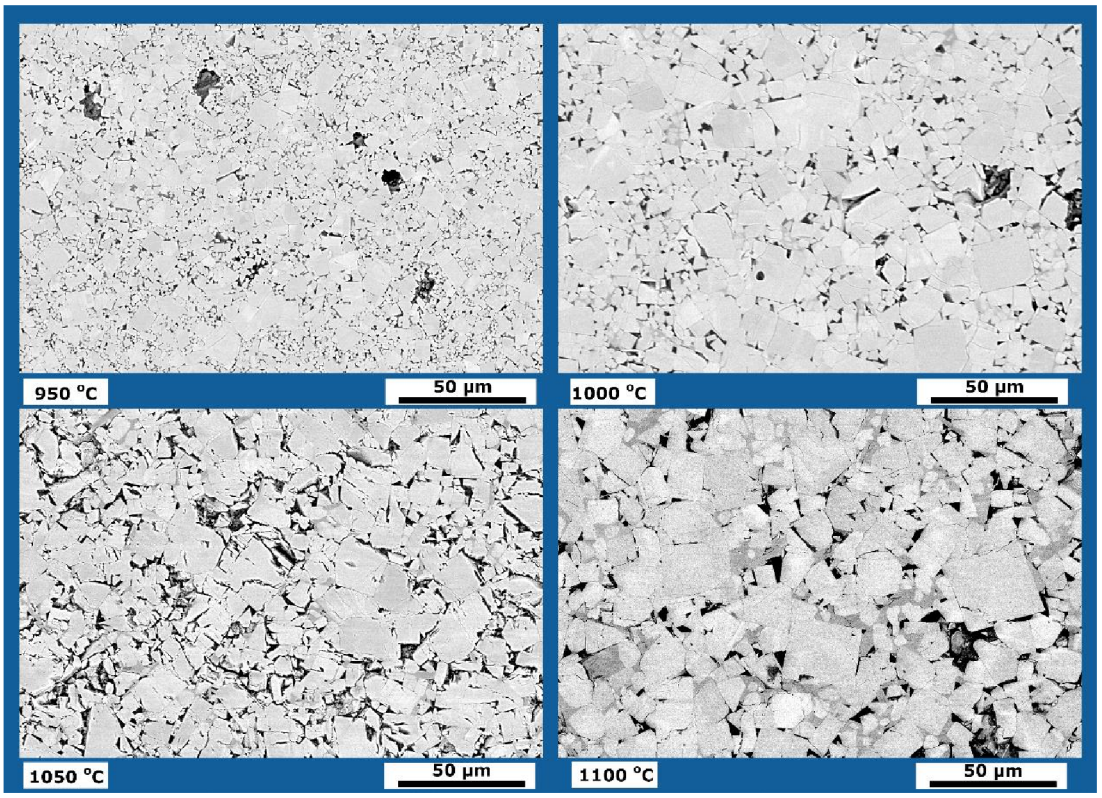

Figure 4.6: BSE micrographs at the same magnification of all samples showing the development of microstructure especially grain size.

It is also important to retrieve quantitative information on the microstructure of the ceramic samples so as to provide a better understanding on the relation between microstructure of the samples and their electrical properties. Duluard *et al.* reported on the coexistence of large and small grains at the sintering temperatures of 850, 900 and 950 °C [86], and only the existence of large grains at the sintering temperature of 1000 °C. However, no quantitative information on the size distribution of grains is provided. In addition to this, Hupfer *et al.* discusses on the effect of $LiTiPO_4$ content on the microstructure of LATP ceramic samples and they provide estimate values for the grain sizes from the micrographs of the LATP

samples; however, they do not go for the direction of micrographs analyses since the low contrast between grains makes the quantitative grain analysis a tough process. Therefore, a quantitative microstructural micrograph analyses of LATP ceramics are missing in the literature.

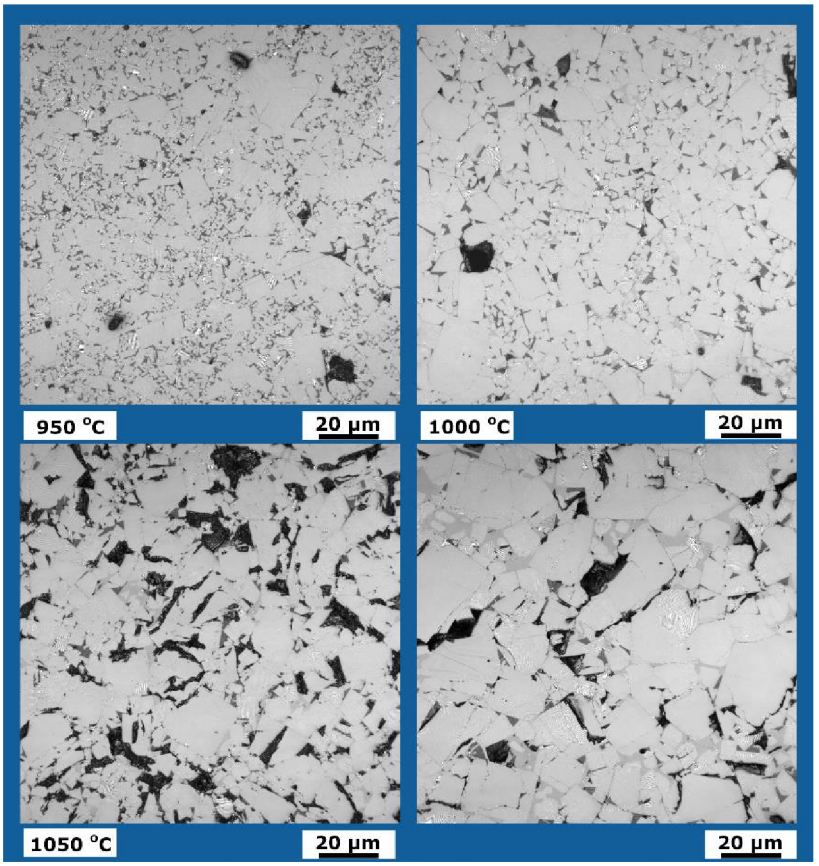

Figure 4.7: CLSM micrographs at the same magnification of all samples showing the development of microstructure.

4.2. Image analyses

The results described above mainly which different phases were identified by various microscopic techniques including SEM, CLSM and TEM and how the microstructure develops qualitatively with increasing sintering temperature. Now,

this section aims to provide qualitative microstructural parameters that can be extracted from image analyses of CLSM and SEM micrographs.

4.2.1. Method

Micrographs of the polished LATP ceramic samples were analyzed with a commercial image processing program Avizo® 9 (FEI Visualization Sciences Group, FEI, Hillsboro, Oregon, USA). Sintering temperatures of between 950 – 1100 ^{o}C are covered in the micrograph analysis of LATP samples. The image analyses were based on pixels of the gray scale images of the respective micrographs. In gray scale images, each pixel is assigned to a value in a range of between 0 to 65535. Binarization was carried out for three different regions corresponding to grains, secondary phases and pores using the interactive thresholding module. Below the bottom threshold, pores are covered; above the upper threshold, grains are covered; and secondary phase regions are covered in the intermediate scale between two threshold scales.

Employing the Segmentation Editor, manual corrections were carried out for the regions, where binarized scale separation does not properly suit. Despite the fact that different microstructural components were separated from each other, some grain boundaries were still not clear; therefore, some grains were still touching to each other. Separate Objects module is used to separate grains from each other. While this module is not quite effective for the separation of concave objects, it is a quite powerful tool for the separation of convex objects, which makes it an ideal module for the analysis of LATP Grains. An exemplary procedure is shown in Figure 4.8, binarization seems to be able to detect different LATP grains for this region; however, these grains still touch each other. When separate objects module is employed, LATP grains 1 and 2 are separated from each other, whereas the grains 2 and 3 are still in contact. Eventually, they are separated from each other with manual corrections.

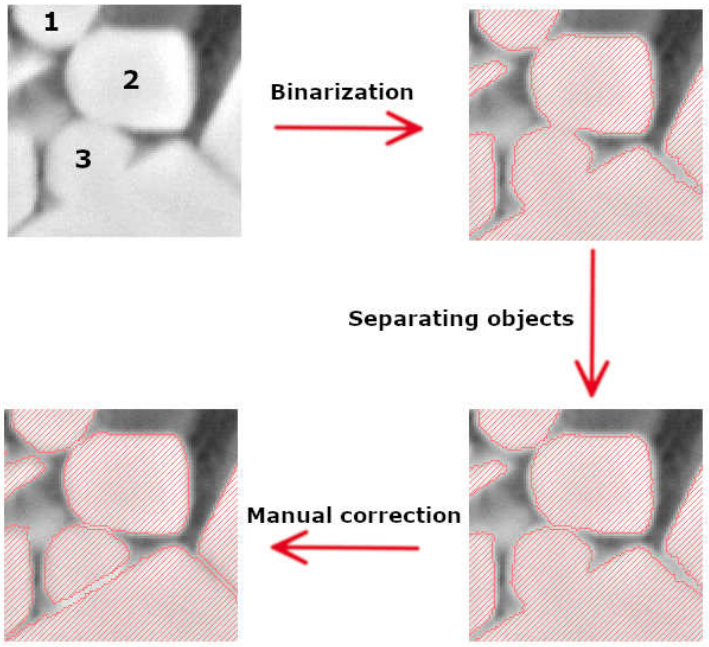

Figure 4.8: Binarization, the use of separate objects module and manual corrections are shown on LATP grains from a small area.

Once grains, secondary phases and pores are fully separated from one another, it became possible to analyse each of those components (grains, pores and secondary phases) separately via assigning different objects to them, resulting in three groups of objects.

Statistical and numerical information including area distributions and shape analyses were obtained using the Label Analysis module. Depending on the results of the Label Analysis module, the Analysis Filter module is used to exclude the areas smaller than some area threshold to eliminate noise. The grains that are not fully inside of the analysis area are excluded from the grain size and grain morphology analysis.

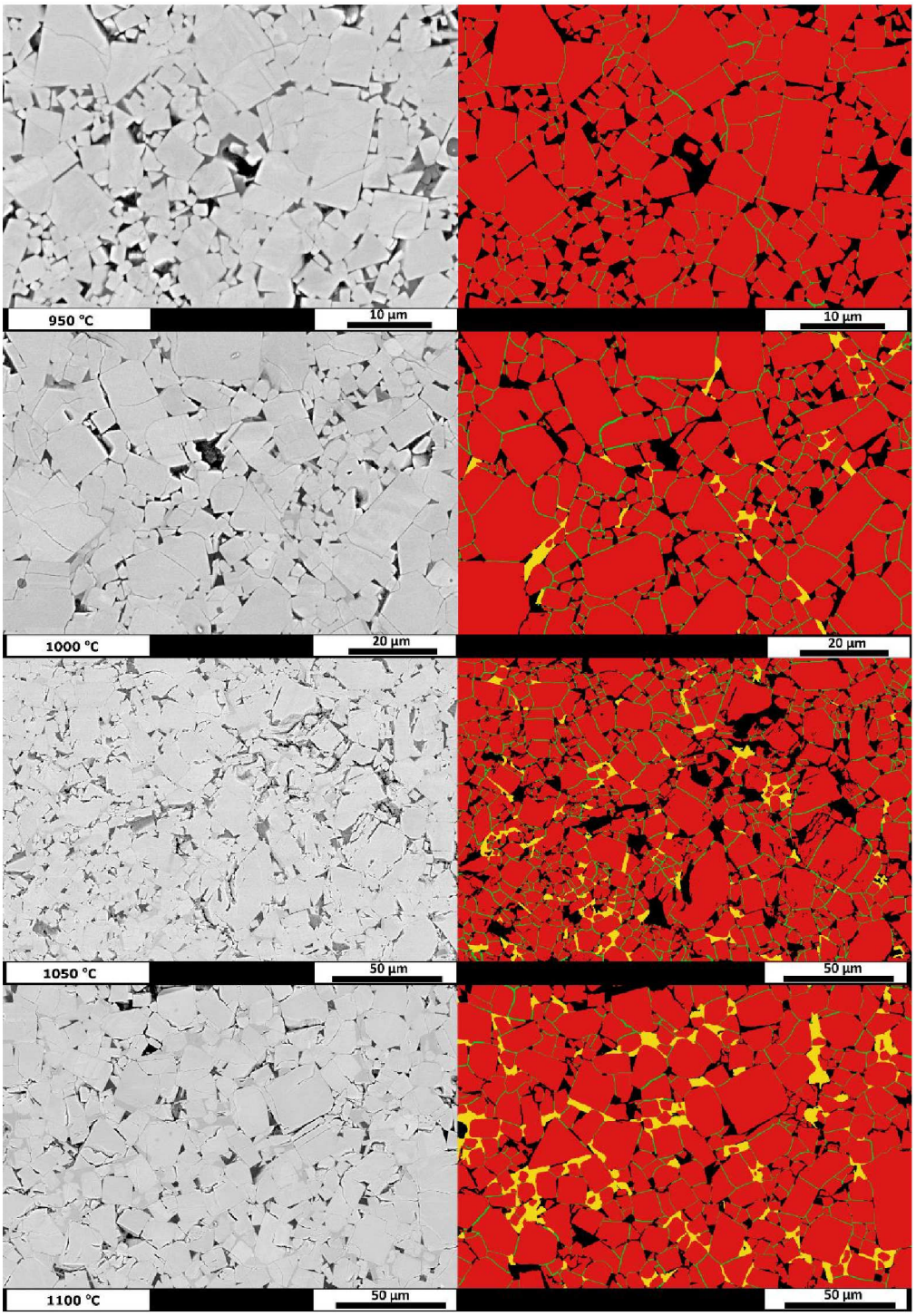

Figure 4.9: Left column shows BSE micrographs used for segmentation with adapted magnifications. The segmented images are shown in the right column. Grains, grain boundaries, secondary phase and pores are shown in red, green, yellow and black, respectively.

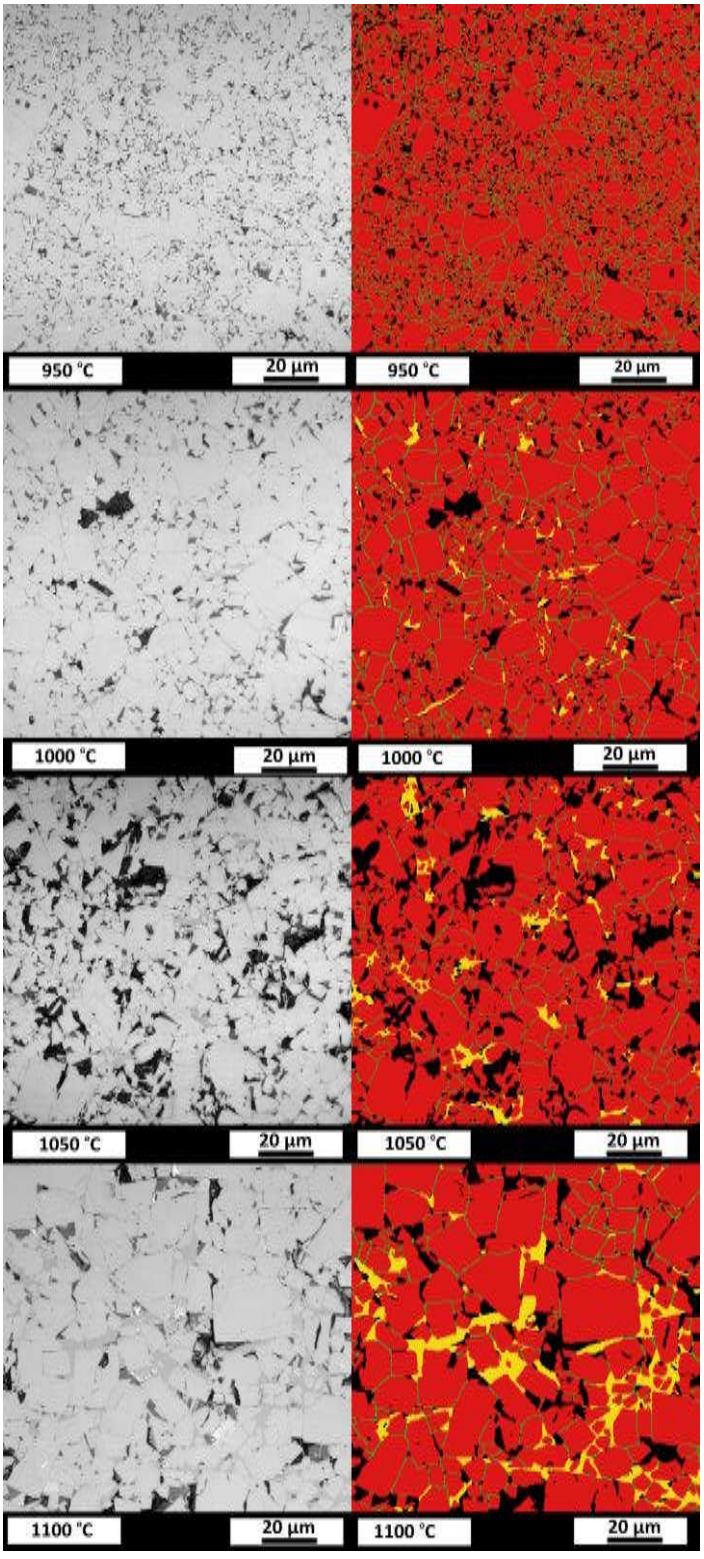

Figure 4.10: CLSM micrographs of LATP samples for the sintering temperatures of between 950 and 1100°C and their segmentation.

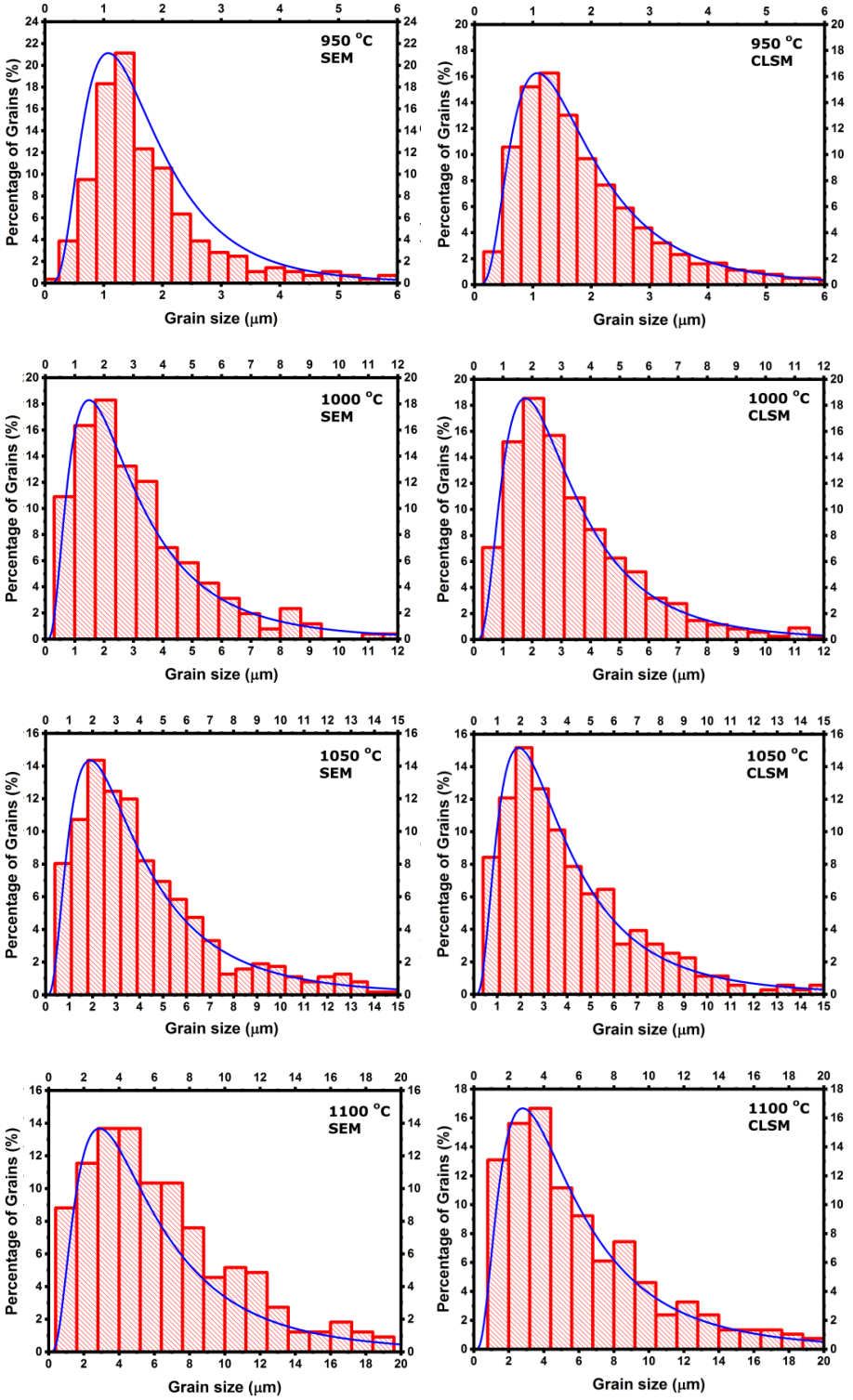

Figure 4.11: Grain size distributions given with their percentages as retrieved from SEM (left) and CLSM (right) micrographs.

Table 4.2: Results of the grain size analysis from CLSM and SEM micrographs.

CLSM					
Sintering temperature	Mean grain size [µm]	σ [µm]	standard error [µm]	Number of grains analysed	Area analysed [µm²]
950 °C	1.59	1.87	0.03	3799	32338
1000 °C	2.77	1.96	0.05	1230	32338
1050 °C	3.29	2.08	0.11	356	16169
1100 °C	4.88	2.10	0.081	672	65333
SEM					
Sintering temperature	Mean grain size [µm]	σ [µm]	standard error [µm]	Number of grains analysed	Area analysed [µm²]
950 °C	1.52	1.80	0.10	284	1962
1000 °C	2.56	2.09	0.13	257	7155
1050 °C	3.35	2.12	0.08	634	28649
1100 °C	5.01	2.10	0.11	329	28649

Table 4.3: Results of the grain morphology and connectivity analysis from CLSM and SEM micrographs.

CLSM						
Sintering temperature	Grain symmetry	Number of grains analysed	Secondary phase [%]	α^+	α^-	Area analysed [µm²]
950 °C	0.75±0.11	3799	-	0.50	0.49	32338
1000 °C	0.79±0.09	1230	1.7	0.46	0.44	32338
1050 °C	0.78±0.10	356	3.9	0.20	0.18	16169
1100 °C	0.77±0.10	672	7.2	0.23	0.22	65333
SEM						
Sintering temperature	Grain symmetry	Number of grains analysed	Secondary phase [%]	α^+	α^-	Area analysed [µm²]
950 °C	0.85±0.06	284	-	0.40	0.38	1962
1000 °C	0.82±0.07	257	1.9	0.42	0.40	7155
1050 °C	0.76±0.12	634	3.2	0.30	0.28	28649
1100 °C	0.81±0.08	329	6.4	0.30	0.28	28649

Figure 4.9 shows CLSM and Figure 4.10 shows SEM images of polished LATP ceramic samples in the column at the left side and their segmentation by Avizo© in the column at the right side for the samples sintered at temperatures of between 950 and 1100 °C. For SEM studies, different magnifications were used for image analysis to adapt the different grain size for each sample in such a way that few hundred grains are included in each image. The segmented images show LATP grains, secondary phase, grain boundaries and pores in red, yellow, green, and black, respectively. Employing combined CLSM and SEM, quantitative information on the evolution of grain sizes, morphology of grains and the contact fraction of grains. Evolution of secondary phase is also quantitatively retrieved from the micrograph analyses of both, CLSM and SEM. All the results from image analysis of CLSM (top of the tables) and SEM (bottom of the tables) micrographs are given in table 4.2 (mean grain size, standard deviation of grain size distribution and standard error) and 4.3 (grain symmetry, secondary phase content, contact fraction of the grains $\alpha^{-}_{contact}$ and $\alpha^{+}_{contact}$).

4.2.2. Grain size distributions

Grain size distributions extracted from the SEM (on the left column) and CLSM (on the right column) micrographs are depicted in the Figure 4.11. Data is shown in red and fits are depicted with a blue colour. Grain size distributions exhibit lognormal distributions with the mean grain sizes listed in table 4.2. By inspection of the images, it can be seen for the sample sintered at the temperature of 950 °C that much of the area is covered by small grains below 2 µm size; whereas, some larger grains are already present. The mean grain size is observed as 1.59 at this sintering temperature. At the sintering temperature of 1000 °C, the distribution becomes broader and extends to much larger grain sizes with a mean grain size of 2.77 µm. For the sintering temperature of 1050 °C, the grain size increases further but not much to a mean value of 3.29 µm. A more drastic increase is observed at the sintering temperature of 1100°C. The broadest grain size distribution is

observed at this sintering temperature and the mean grain size jumps up to 4.88 µm. Grain size distributions determined by SEM are similar to the ones determined by CLSM. Grain size distributions both exhibit log-normal distribution characteristics in CLSM and SEM analyses. In addition to that, like the trend observed by CLSM, a strong increase in grain size observed for the increase of the sintering temperature from 950 °C to 1000 °C and also for the last step from the sintering temperature of 1050 °C to the sintering temperature of 1100°C. With the increasing sintering temperature, increasing mean grain sizes and broader grain distribution are observed both by CLSM and SEM.

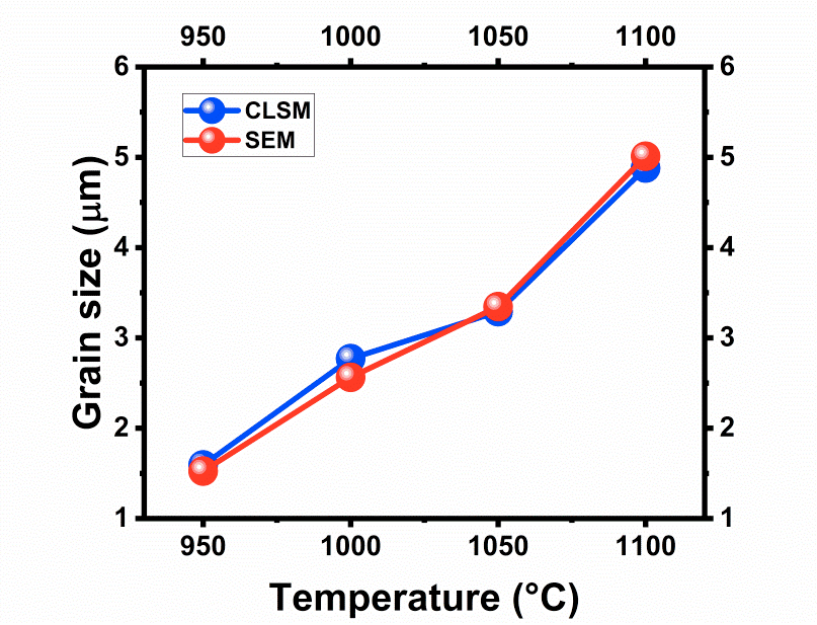

Figure 4.12: The evolution of the mean grain size with increasing sintering temperature.

Duluard *et al.* qualitatively reported on the coexistence of small and large grains at the sintering temperatures of 850, 900, 950 °C and only the existence of large grains at the sintering temperature of 1000 °C. In this thesis study, due to lognormal grain size distribution characteristics, large and small grains were observed together in the same samples for the sintering temperatures of 950 – 1100 °C. In all samples, larger grains exhibit cracks as already stated by other

researchers [37]. For the sample sintered at the temperature of 1100°C, these cracks are observed more frequently.

Alteration in the mean grain areas obtained both from CLSM and SEM are plotted versus sintering temperature of the samples in Figure 4.12. With the increasing sintering temperature, grain sizes increase. The standard error of the mean (SEM), $\Delta\sigma$, can be written as the following:

$$\Delta\sigma = \frac{\sigma}{\sqrt{n}} \tag{4.1}$$

where σ is the standard deviation of the measurements and n is the size (number of measurements) of the data. On the other hand, as tabulated in Table 4.2, the number of the analysed grains is much higher compared to the standard deviations. Therefore, standard errors of the grain size measurements are low, and they are not shown in the Figure 4.12 since error bars would stay in the circular data points.

4.2.3. Secondary phase

The secondary phase (light gray areas) can be resolved for the samples sintered at the temperatures of 1000°C and higher and is found mainly agglomerated in larger intergranular spaces. Table 4.3 also lists the area fractions of secondary phase. The total amount but also the size of the secondary phase regions increases with the increasing sintering temperature from about 2% for the sintering temperature of 1000°C to 4 % and 7 % for the sintering temperatures of 1050 and 1100 °C, respectively for both CLSM and SEM. Secondary phase locates in intergranular space and therefore has a complicated concave shape. Despite the secondary phase formation, conduction paths around less conductive secondary phase regions are still possible at least up to the sintering temperature of 1050 °C. On the other hand, bulky secondary phase regions were observed at the sintering temperature of 1100 °C. Some of these secondary phase regions can deteriorate conduction paths via insulating some of the grains from the others.

As discussed in section 4.1.1 the z-information can be used to distinguish the secondary phase with dark contrast from porosity by introducing a z-threshold. With a z-threshold of 0.2 µm, this leads to the amounts for the secondary phase and porosity given in table 4.3. This is the advantage of CLSM over SEM, as porosity and the dark secondary phase do not always have a clearly distinct contrast.

Thin films at the grain boundary could be present but are not detectable neither by CLSM and nor by SEM images. This would only have minor effect on the total amount of secondary phase as the total area would not change in a significant manner. It still could affect the total ionic conductivity because of the fact that such a film of secondary phase wetting the grain boundaries would increase their resistance.

The changes in the bulk chemistry during the course of secondary phase formation might also be important for the lithium ion transport properties of samples. Therefore, an overall chemical investigation of different phases worth studying in order to provide a better understanding on the evolution and formation mechanism of secondary phase and its effect on the electrical properties of samples. On the other hand, such a further study requires the use of EDS.

4.2.4. Grain morphology

Grain morphology is one of the most critical factors influencing the properties of ceramic materials in general. In addition to that, the classical BLM assumes cube-shaped grains of identical size [73][74][75][76][77]. Some qualitative descriptions on the morphologies of grains are available. Therefore, many of these analyses depend on the subjective approach of the researcher. On the other hand, a standardized general model accounting for the quantitative grain-shape analysis, however, is still missing. For LATP, cuboidal grains are described in literature [52] [98][99], but still no specific model has been reported so far.

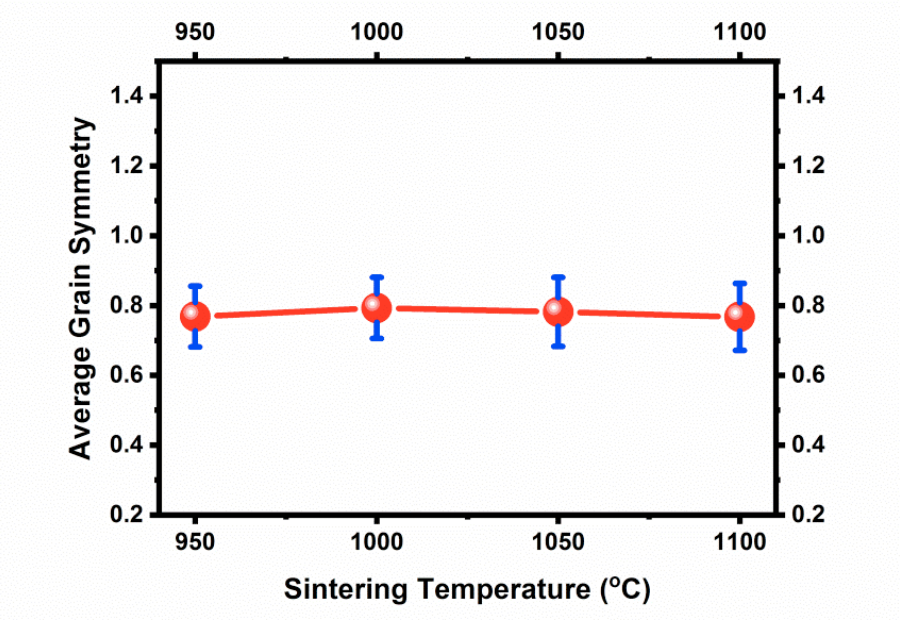

(a)

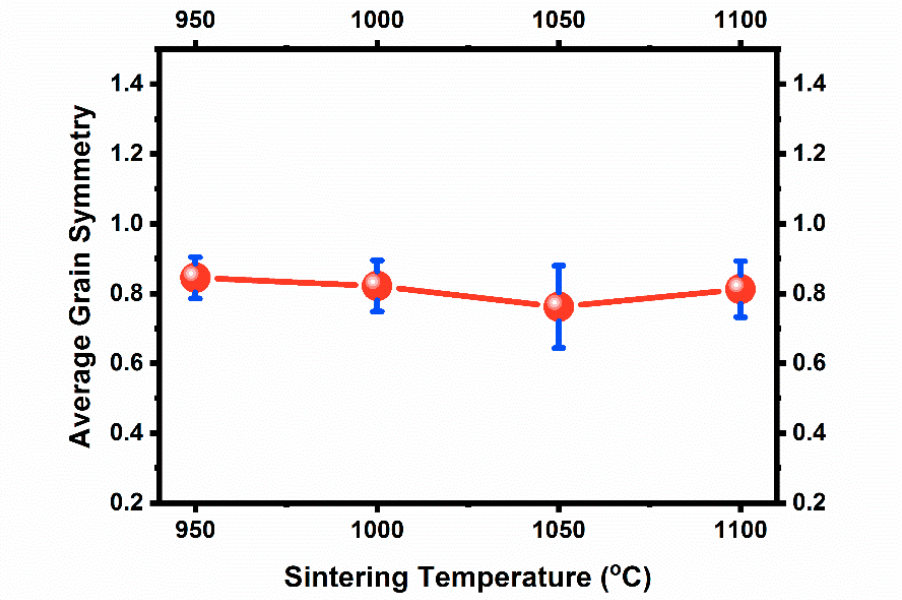

(b)

Figure 4.13: Values of the symmetry measurement function retrieved from the analyses of (a) CLSM micrographs and (b)SEM micrographs.

Exploiting the CLSM and SEM micrographs of polished LATP ceramic samples in Figures 4.9 and 4.10, at first sight mainly cuboidal shaped grains are present. Hence, it is required to quantify how much these cuboidal looking grains deviate from the ideal cubes. In order to gain further insight about the shape of grains, the symmetry measurement function, S, is employed. Related geometric parameters are shown in Figure 4.14. C represents the centre of mass of the two-dimensional homogenous grain; $\mathrm{I_a}$ and $\mathrm{I_b}$ are the two intersection points of a single line and grain boundary. The symmetry measurement function can be written in terms of the geometric parameters as following:

$$(G) = \frac{1}{2}[1 + Min_n(\frac{A_{min}}{A_{max}})] \qquad (4.2)$$

where G stands for the single grain, $\mathrm{A_{min}} = \mathrm{MIN}(\overline{\mathrm{I_aC}}, \overline{\mathrm{I_bC}})$ and $\mathrm{A_{max}} = \mathrm{MAX}(\overline{\mathrm{I_aC}}, \overline{\mathrm{I_bC}})$ are the minimum, maximum length of intersections through the centre of gravimetry of the grain C. It should be noted that $\mathrm{A_{min}}$ and $\mathrm{A_{max}}$ are measured on the same line. $\mathrm{Min_n}$ represents the minimum value operator over the angles $\theta_n \in [0, \pi]$. In this manner, all possible lines are spanned. For the case of a fully symmetric shape, a square for this case, symmetry measurement function will be equal to one because on any continues line, $\mathrm{A_{min}}$ and $\mathrm{A_{max}}$ would be equal to each other. On the other hand, it will decrease with an increase in asymmetry. For all sintering temperatures, values around 0.8 are obtained for the symmetry function. Hence, the grains are not close to cubic shape, and no temperature dependence is observed.

In Figure 4.13, average grain symmetry values depending on the synthesis temperature are provided for the polished LATP ceramic samples for the sintering temperatures of between 900 – 1100 ^{o}C ((a) CLSM and (b) SEM). For all the sintering temperatures, values around 0.8 are obtained for the symmetry function both by CLSM and SEM despite small deviations. Hence, the grains are not ideally cubic. On the other hand, no temperature dependence is observed.

Likewise, all the results from grain morphology and connectedness analysis of SEM micrographs are given in table 4.3 below the values obtained from CLSM for comparison.

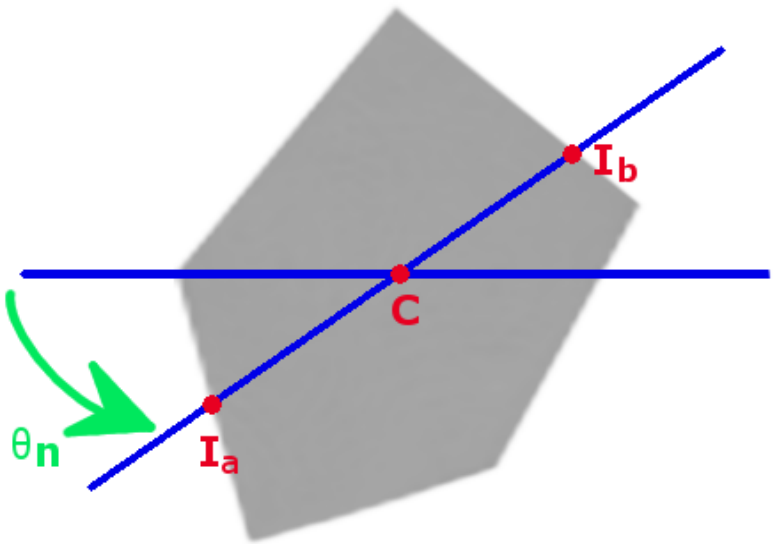

Figure 4.14: Working mechanism of symmetry measurement is shown for a single grain.

4.2.5. Contact ratio

For the case of imperfect contacts, Fleig and Maier [45] suggest that only a fraction $\alpha_{contact}$ of a grain is in a perfect contact with the neighboring grains in solid-state electrolytes. Therefore, for LATP ceramic samples, a fraction of $\alpha_{contact}$ of a grain has a perfect contact with the neighbouring grains due to the blocking of pores and secondary phase. The contact fraction of the grains $\alpha_{contact}$ can also be retrieved from the image analyses via the ratio of the connected length of the grains and the total length of boundaries present in a micrograph as the following equation:

$$\alpha_{contact} = \frac{connected\ length\ of\ grain\ boundary}{total\ length\ of\ grain\ boundary} \quad (4.3)$$

The grain size analysis also gives perimeter p of grains and other objects, such as pores and secondary phase regions, which is used for the calculation of the contact fraction of the grains $\alpha_{contact}$. As for all quantitative image analysis, it is assumed that the image is representative for the sample and the contact fraction of the grains $\alpha_{contact}$ is calculated assuming periodic boundary conditions, which is a reasonable assumption for a sufficiently large field of view. Assuming that the cut off produced by the image is a real perimeter, the contact fraction of the grains $\alpha_{contact}$ can be described as follows:

$$\alpha^{+}_{contact} = \frac{\frac{1}{2}(\sum_{i=1}^{n} p_{gi} - \sum_{j}^{m} p'_j)}{\frac{1}{2}(\sum_{i=1}^{n} p_{gi} + \sum_{j}^{m} p'_j)} \quad (4.4)$$

where p_g are the grain perimeters and p' are the perimeters of other objects including pores and secondary phase regions. Pores and secondary phase regions are merged together before the contact fraction to eliminate the complications which might arise due to the borders between secondary phase regions and pores.

Perimeters of the images are not real perimeters of objects. Therefore, if the perimeters of the images are subtracted from the sum of perimeters, equation (4.4) becomes:

$$\alpha^{-}_{contact} = \frac{\frac{1}{2}(\sum_{i=1}^{n} p_{gi} - \sum_{j}^{m} p'_j - p_{image})}{\frac{1}{2}(\sum_{i=1}^{n} p_{gi} + \sum_{j}^{m} p'_j - p_{image})} \quad (4.5)$$

The sum of perimeters is counted half only in order not to count them twice. Figure 4.15 provides a simple schematic representation of the calculation method of the contact fraction of the grains $\alpha_{contact}$. I calculate both the contact fraction of the grains $\alpha^{+}_{contact}$ and $\alpha^{-}_{contact}$ in order to estimate the error of these assumptions. An additional error is always naturally introduced by the selected area for the analysed micrograph. In Figure 4.15, there are three red large grains with a side length of "a" is equal to 2, three small ones in the same colour with a side length "a"

is equal to 1 and also a blue "other object". Perimeters are shown in green. According to the equation (4.4), the contact fraction of the grains $\alpha^{+}_{contact}$ is calculated as 16/20 = 0.8 and according to the equation (4.5), the contact fraction of the grains $\alpha^{-}_{contact}$ as 8/12 = 0.67.

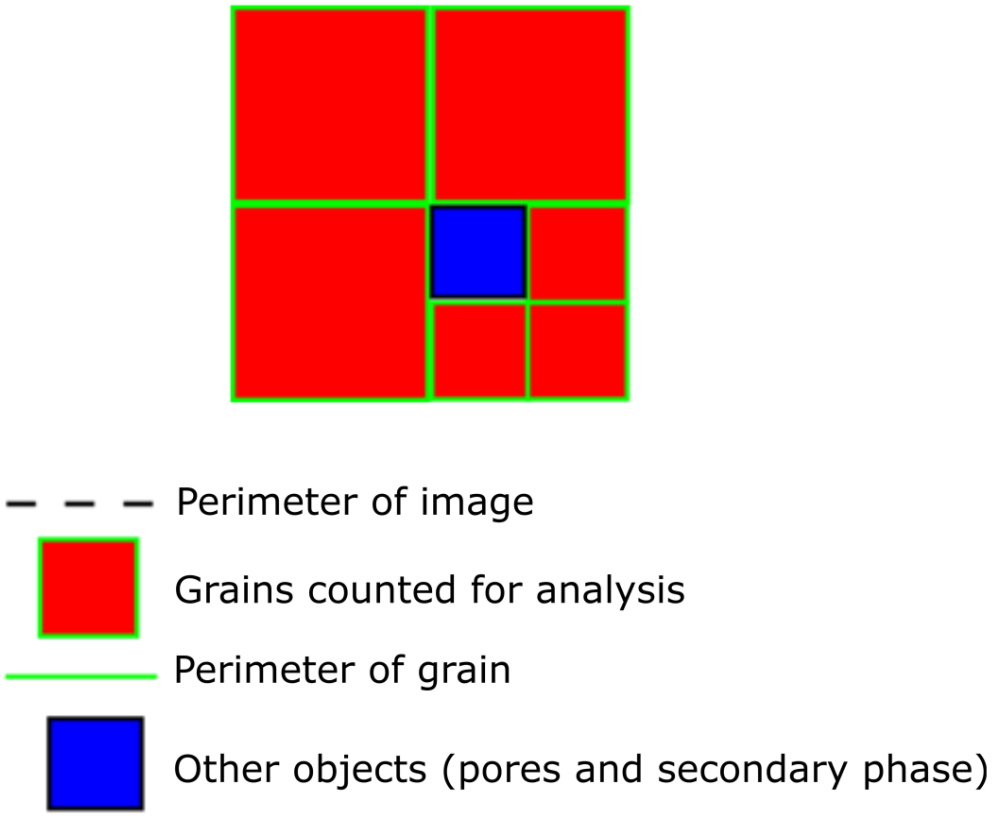

Figure 4.15: Visualization of the determination of the contact ratio α simplified with square-shaped grains.

In an ideal case, perfect contacts between homogenous grains are assumed. On the other hand, as both CLSM and SEM micrographs suggest, secondary phase and pores deteriorate such ideal grain contacts. From the segmented CLSM and SEM micrographs of LATP ceramic pellets, contact ratio of grains $\alpha_{contact}$ was deduced as described before. In addition to the error introduced by the cut off at the edges of micrographs, an error is also introduced by the selected area in the

micrograph. Both of these errors will reduce for a larger field of view with higher numbers of grains and other objects within a single image. The contact fraction of the grains $\alpha^{+}_{contact}$ and $\alpha^{-}_{contact}$ calculated in that way are listed in table 4.3 and their difference is small with the sufficient field of view.

One trade-off in the image analyses of CLSM and SEM micrographs of LATP ceramic samples is the limited spatial resolution > 125 nm for CLSM and even for SEM it varies in the range between 36 and 130 nm. Thin films of secondary phase partially wetting grain boundaries, as observed in TEM will be missed in both, CLSM as well as SEM investigations. On the other hand, both CLSM and SEM micrographs show a similar trend, with the contact ratio of the grains $\alpha_{contact}$ decreases from about 0.4 – 0.5 for the LATP ceramic samples sintered at temperatures of 950°C and 1000°C sintered sample to about 0.2 to 0.3 for the samples sintered at temperatures of 1050°C and 1100°C. This decrease of the contact fraction of the grains $\alpha_{\mathrm{contact}}$ with increasing sintering temperature is valid under the assumption of only non-lithium ion conducting secondary phase such as $AlPO_4$ and porosity.

4.3. Impedance

Electrochemical Impedance Spectroscopy (EIS) was measured at a temperature of 20 °C for the LATP ceramic samples with the sintering temperatures of 950, 1000, 1050 and 1100 °C and Nyquist plots are shown in Figure 4.16. The analysis of impedance data for all the samples showed the lowest total resistance for the sample sintered at the temperature of 1050 °C. Assuming a dense pure phase ceramic ionic conductor, the total conductivity will be according to the BLM [73][74] defined by grain and grain boundary conductivity. In its most simple form, all grains have the same size.

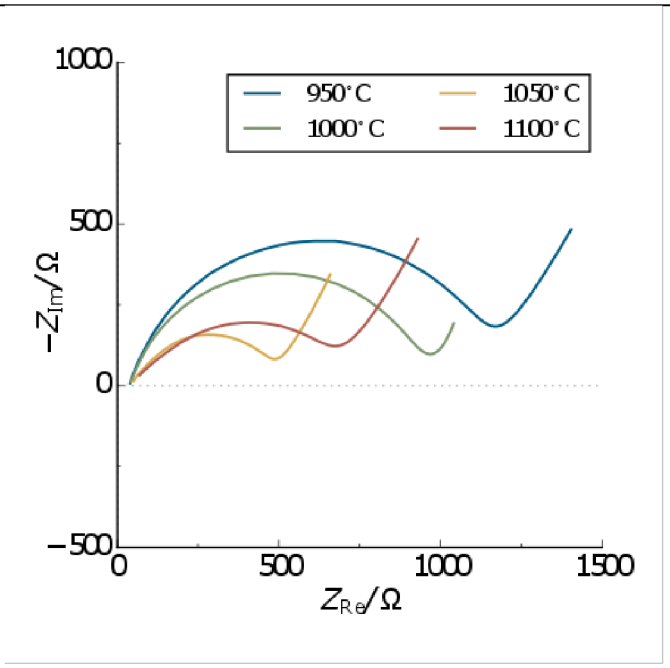

Figure 4.16: Nyquist plots measured at 20 °C for the samples sintered at temperatures of between 950 and 1100°C.

4.4. Correlation of impedance and microstructure

In this section, the electrical properties of the LATP ceramic samples, sintered at temperatures between 950 and 1100 °C, in dependence of sintering temperature and related microstructural properties such as grain size, morphology of grains, contact fraction of grains and secondary phase content retrieved from correlative SEM and CLSM studies are discussed in detail and main determining parameters are found.

Because of the fact that the grain boundary resistance is three orders of magnitude higher than the grain resistance, the main effect on conductivity is expected to be the number of grain boundaries which are needed to be crossed on the way through the pellet as sketched in Figure 4.17, where grains are shown in red, grain boundaries are depicted in green and the contacts are shown in gray.

With the assumption of straight lithium ion conduction pathways through the pellet, the total resistance R_t will be determined by a serial connection of the grain resistance R_g and the grain boundary resistance $R_{g.b}$. Both of the grain resistance and grain boundary resistance values are determined by the length of the conduction path through each kind of material with its ionic conductivity σ_g (grain) and $\sigma_{g.b}$ (grain boundary) as described in the equations 4.6 to 4.8, where *t* is the pellet thickness, *A* is the contact area of the pellet, *D* is the grain size and *d* is the grain boundary width. Grain resistance, grain boundary resistance and the total resistance can be written as the followings in terms of the described parameters:

$$R_g = \frac{1}{\sigma_g}\frac{t}{A}\frac{D}{(D+d)} \tag{4.6}$$

$$R_{g.b} = \frac{1}{\sigma_{gb}}\frac{t}{A}\frac{d}{(D+d)} \tag{4.7}$$

$$R_t = R_g + R_{g.b} \tag{4.8}$$

With the approximation made for *D* >> *d*, which is reasonable for grain size in the micrometre and grain boundary width in the nanometre range, equations (4.6), (4.7) and (4.8) can be rewritten as the following equations:

$$R_g = \frac{1}{\sigma_g}\frac{t}{A} \tag{4.9}$$

$$R_{g.b} = \frac{1}{\sigma_{gb}}\frac{t}{A}\frac{d}{D} \tag{4.10}$$

$$R_t = R_g + R_{g.b} \tag{4.11}$$

This would explain the fact why the samples sintered at temperatures of 1050°C and 1100°C show the highest overall conductivity since the contribution of the grain boundary to the total resistance is low due to the large grain size.

For the case of $D >> d$, which is reasonable for the grain sizes in the micrometre and grain boundary width in the nanometre range as shown in Figure 4.4, a linear behaviour would be expected for the total and the grain boundary resistance, assuming a constant grain boundary width for all samples, which is reasonable by our TEM findings. The grain resistance should stay constant in a first approximation.

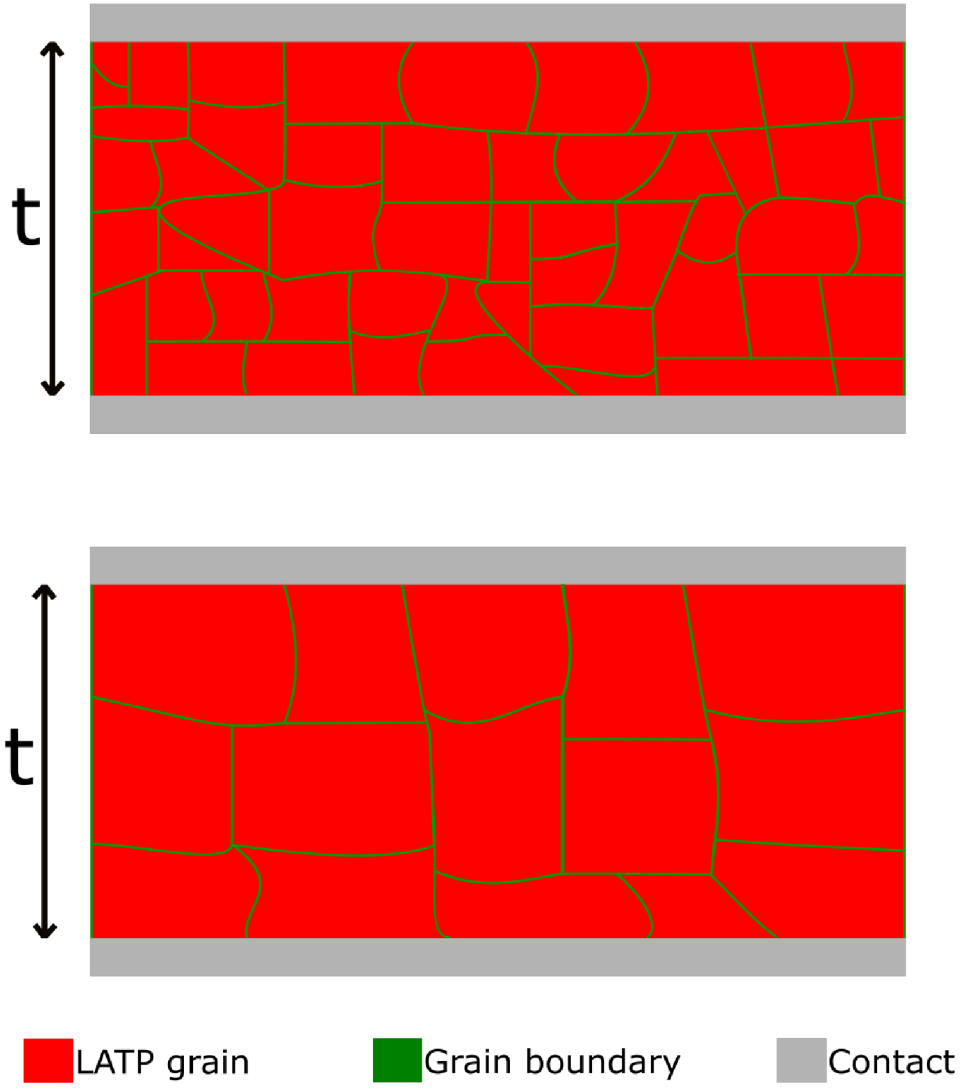

Figure 4.17: A simple schematic description of the alteration in the grain sizes of LATP with increasing sintering temperature. Grains, grain boundaries and contacts are coloured with red, green and gray in a respective manner. *t* is the thickness of samples.

By quantitative Image analysis grain size distribution were obtained for the four sintering temperatures. In Figure 4.18 the total resistance, R_t, *is* plotted versus the inverse grain size values retrieved from CLSM and SEM micrograph analysis. The total resistance of the pellet decreases with increasing sintering temperature vs. mean inverse grain size 1/D up to the sintering temperature of 1050°C. During the course of the transition from the sintering temperature of 1050°C to 1100°C, it increases.

Microstructural analyses showed that there are pores and secondary phase regions. Finite-element method modelling was previously carried out by Fleig *et al*. so as to reveal the effect of partially wetting insulating phase and porous imperfect contacts on grain boundary resistance [75][76]. They describe how the ratio of grain boundary and grain resistance is influenced by the contact fraction of the grains $\alpha_{contact}$, the number of contact points *n* between two grains and g_{corr} is the correction factor for geometrical current constriction (equation 4.12) and can be assumed as $g_{corr} \approx 0.5$ for $\alpha_{contact} < 0.4$ [75].

The values for contact fraction $\alpha_{contact}$ retrieved from segmented micrographs represent in approximation the ratio of the length of grain boundary in the image to the sum of grain perimeters. The values determined vary between 0.2 and 0. 5. In equation 4.12, $R_{g.b}$ and R_g are the grain boundary and grain resistances respectively; n is the average number of contact points between two grains and g_{corr} is the correction factor for geometrical current constriction. As mentioned, for the case of the contact fraction of the grains $\alpha_{contact}$ is smaller than 0.4, and this can be approximated to $g_{corr} \approx 0.5$ leading to the approximation of equation 4.12 and only in such cases a low frequency semicircle is observable in impedance spectroscopy [75].

Mariappan *et al.* used the following formula in order to retrieve the contact ratio from grain boundary resistance and grain resistance measured by impedance on a similar material $Li_{1.5}Al_{0.5}Ge_{1.5}(PO_4)_3$ (LAGP) NASICON Ceramic [100]:

$$\frac{R_{g.b}}{R_g} \approx \frac{1}{\sqrt{n\alpha_{\text{contact}}}} g_{corr} \approx \frac{1}{\sqrt{4n\alpha_{\text{contact}}}} \quad (4.12)$$

They retrieved a value of 0.25 in accordance with their TEM micrograph. On the other hand, their impedance analysis led to comparable activation barriers (E_g = 0.43 ± 0.02 eV, $E_{g.b}$ = 0.42 ± 0.02 eV) for grain and grain boundary conduction if LAGP in contrast to our LATP for which E_g = 0.147 eV and $E_{g.b}$ = 0.403 eV were determined. However, the area they study contains just a few grains due to the limited field of view of TEM. Therefore, a more comprehensive approach is required. Therefore, in this thesis study, I employed SEM and CLSM, which allows the study of hundreds of grains.

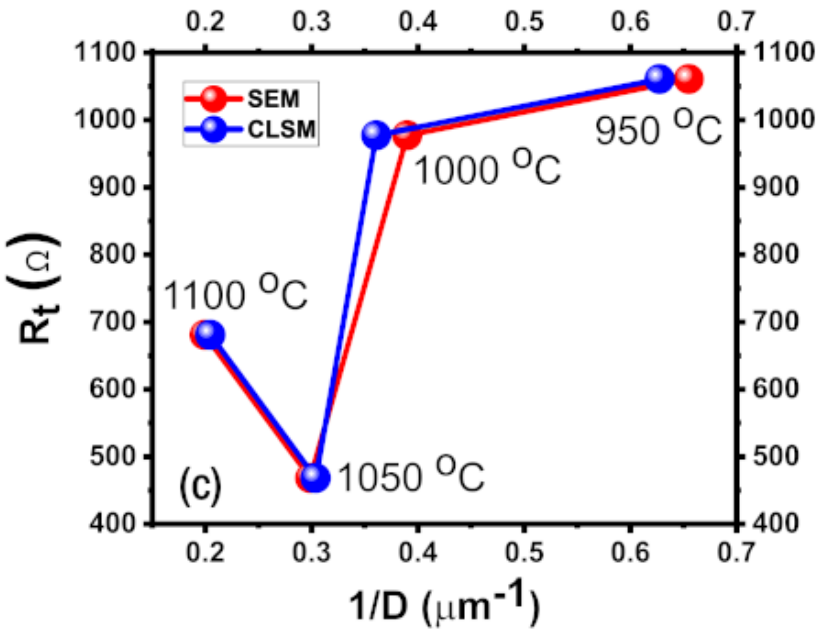

Figure 4.18: Total resistance retrieved from impedance plotted vs. the inverse mean grain size for the sintering temperatures of at between 950 and 1100°C.

The contact fraction of the grains $\alpha_{contact}$ in this work was determined from CLSM and SEM micrographs varies between 0.2 and 0.5, which seems reasonable. On the other hand, the micrographs have limited resolution in the range of 22

nm/px for the sintering temperature of 900°C and 130 nm/px for the sintering temperature of 1100°C, depending on the necessary field of view for statistical analysis. Hence, the secondary phase cannot be detected in these images, if distributed in narrow films between grains due to limited lateral resolution. TEM micrographs show the presence of few nm thin films in grain boundaries for all the sintering temperatures. If these films would be assumed as blocking the contact fraction of the grains $\alpha_{contact}$ should be much smaller but this would not explain the global ionic conductivity of the pellets. Therefore, I interpret the grain boundaries with a thin film of secondary phase as conductive to lithium ion with a ionic conductivity about three orders of magnitudes lower than the grain conductivity [78], which is in agreement with literature in a manner that lithium-aluminium-phosphates have been reported with a low lithium ion conductivity also in the range of 10^{-5} S/cm [101,102]. Because of the fact that the contact fraction of the grains $\alpha_{contact}$ stays almost constant within its error with sintering temperature, the main contribution to the increasing conductivity with increasing sintering temperatures must be attributed to other parameters. In addition to this, due to the fact that the grain morphology does not change at all and the grain symmetry measurement function gives values around 0.8 for all of the sintering temperatures, only the grain size can play a determining role.

Up to 1050°C sintering temperature, the main effect on total conductivity might be attributed to the increasing grain size and hence the reduced lithium ion conduction path length across grain boundaries as sketched in Figure 4.17. Partial wetting of the grain boundaries by the secondary phase as well as a significant increase of the amount of secondary phase with increasing sintering temperature were observed, especially from the sintering temperature of 1050 °C to 1100 °C. Therefore, this is probably the reason why the resistance increases at 1100 °C. Similar to Hupfer et al. [27], I also observe cracks in the large grains. Therefore, both cracks as well as secondary phase wetting grain boundaries could be limiting

factor for a further decrease of grain boundary resistance measured by impedance spectroscopy for sintering temperature 1100 °C.

Taking all the microstructural information which were gathered from correlative CLSM and SEM studies by us (grain morphology, contact fraction of the grains $\alpha_{contact}$, grain size and the amount of aluminium phosphate secondary phase), we can come to the conclusion that up to a sintering temperature of 1050 °C the main microstructural parameter that affects the lithium ion conduction is the increase of the grain size with increasing sintering temperature via reducing the length of the lithium ion conduction pathways. Therefore, it is possible to tune the ionic conductivity of LATP ceramic samples via increasing grain sizes. On the other hand, the impacts of crack formation and elevated aluminium phosphate formation at the sintering temperature of 1100 °C come into the account as well. During the course of the transition from the sintering temperature of 1050 °C to 1100 °C, resistance increases. Therefore, crack formation and elevated aluminium phosphate formation also become the factors that should be taken into consideration.

Chapter 5 : Quantitative study of secondary phase evolution during sintering of $Li_{1.3}Al_{0.3}Ti_{1.7}(PO_4)_3$ superionic Li-conducting ceramics

In this chapter, the phases present in the material are identified by EDS in both SEM and STEM. This phase identification is used for image segmentation based on elemental mapping in the SEM. The evolution of different phases is tracked for the sintering temperatures of between 950 – 1100 ^{o}C. Moreover, both the formation mechanism of $AlPO_4$ secondary phase chemical changes in the LATP bulk is revealed, and all these factors are correlated with the electrical properties of LATP ceramic samples. STEM imaging was done by Roland Schierholz, and impedance results were provided by Shicheng Yu and Andreas Mertens.

5.1. Phase identification and attribution by EDS

At first EDS measurements were performed on different points in the microstructure. Figure 5.1 shows two BSE micrographs for LATP samples sintered at temperatures of 1100°C (a) and 1050°C (b). In Figure 5.1 (a), three different grey levels can be obtained and point spectra reveal three different phases, with the quantification given in table 5.1. Spectra belonging to the marked regions of Figure 5.1 (b) are provided in Figure 5.2. For clarity, the colours of arrows and numbers in Figure 5.1 (b) are provided with the same colour in the corresponding spectra in Figure 5.2 for the corresponding regions. The associated elements of spectral peaks are marked above the spectral peaks in Figure 5.2

The spectrum (1) in Figure 5.2 (a) from point (1) inside a grain in Figure 5.1 exhibits oxygen Kα emission line (Kα1 at 0.5249 keV), aluminium Kα emission line

at 1.486 keV, phosphorus Kα emission line at 2.013 keV, titanium Kα (Kα1 at 4.51084 keV and Kα2 at 4.50486 keV) and titanium Kβ ($K\beta_1$ 4.93181 keV) emission lines. On the other hand, titanium Lα (Lα1 at 0.4522 keV and Lα2 at 0.4522 keV), titanium Lβ (Lβ1 at 0.4584 keV) emission lines partially overlap with oxygen Kα (Kα1 at 0.5249 keV) emission line. The quantification of the spectra at point (1) in both samples gives values of about 2 at.% aluminium, 12 at.% titanium, 21 at.% phosphorus and 66 at.% oxygen. These values are quite close to the theoretical ones for $Li_{1.3}Al_{0.3}Ti_{1.7}(PO_4)_3$, which are also given in table 5.1. As lithium cannot be detected and quantified by EDS, theoretical values excluding lithium are also provided. The experimental values confirm that the grains consist of LATP. However, still, the differences (absorption of Oxygen Kα) are significant and might be explained by the different emission line energies, which result in different excitation/escape volumes for the different elements. Within the experimental error, the grains are attributed to crystalline $Li_{1.3}Al_{0.3}Ti_{1.7}(PO_4)_3$with R-3c crystal structure (ICSD no. 427619) [39] according to previously reported X-ray powder diffraction results of the same material [92].

The spectrum (2) in Figure 5.2 (b) from point (2) in the light gray secondary phase in Figure 5.1 exhibits oxygen Kα emission line (Kα1 at 0.5249 keV), aluminium Kα emission line at 1.486 keV, phosphorus Kα emission line at 2.013 keV, titanium Kα (Kα1 at 4.51084 keV and Kα2 at 4.50486 keV) and titanium Kβ ($K\beta_1$ 4.93181 keV) emission lines. The quantification of point (2) clearly exhibits a higher content of aluminium and a reduced amount of titanium compared to the grains (Table 5.1).

Point (3) in dark gray secondary phase only shows oxygen Kα and phosphorus Kα emission lines in the spectrum. As lithium is not detectable by EDS, no conclusion can be drawn whether lithium is present in this secondary phase, but a lithium phosphate is probable. The phosphorus:oxygen ratio ranges from close to 1:3 (point 3 in Figure 5.1 (a)) for LATP sintered at temperature of 1100°C to 2:5 (point 3 in Figure 5.1 (b)) for LATP1050°C.

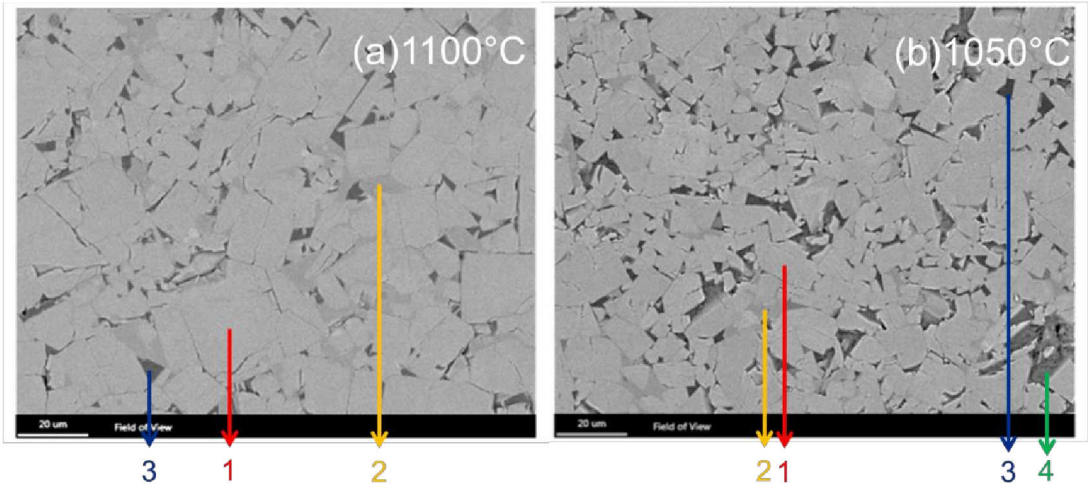

Figure 5.1: SEM micrographs of LATP samples sintered at (a) 1100 and (b) 1050 °C and point spectra from marked positions.

Table 5.1: Quantification of spectra from the points 1 to 3 in both images in Figure 5.1. For comparison, theoretical values are given for $(Li_{1.3}Al_{0.3}Ti_{1.7}(PO_4)_3$ (excluding lithium as it cannot be detected by EDS) and $AlPO_4$.

SEM 1100°C	Al	Ti	P	O
Point 1	1.89	11.57	20.91	65.63
Point 2	4.93	8.08	20.71	66.28
Point 3	-	-	23.9	76.1
SEM 1050°C	Al	Ti	O	P
Point 1	2.05	11.93	21.32	64.71
Point 2	4.29	8.55	21.99	65.17
Point 3	-	-	27.94	72.06
Theoretical	Al	Ti	P	O
$(Li_{1.3})Al_{0.3}Ti_{1.7}(PO_4)_3$	1.76	10.00	17.65	70.59
$AlPO_4$	16.67	0.00	16.67	66.67
$(Li_3)PO4$	-	-	20	80

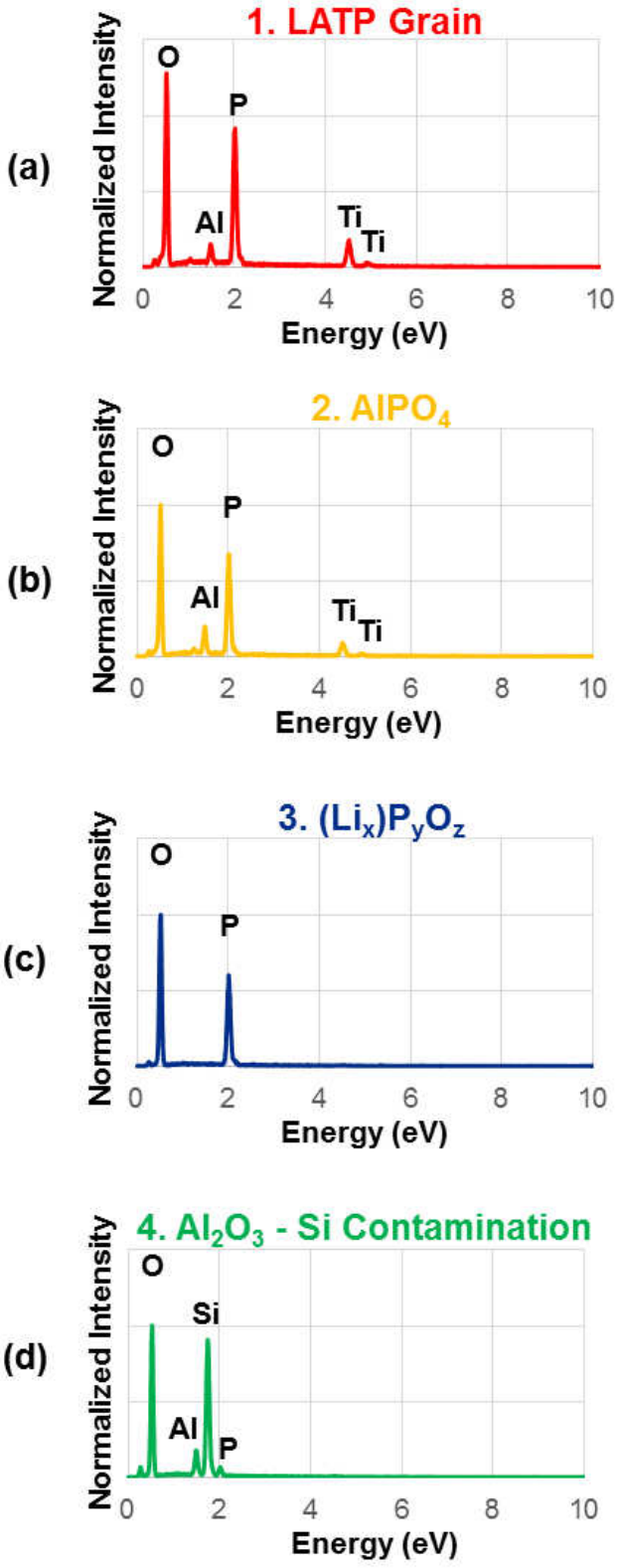

Figure 5.2: Point spectra from marked positions of the Figure 5.1 (b).

The spectrum (4) in Figure 5.2 (b) from point (4) in dark gray contamination region in Figure 5.1 exhibits oxygen Kα emission line (Kα1 at 0.5249 keV), aluminium Kα emission line at 1.486 keV, phosphorus Kα emission line at 2.013 keV and silicon Kα emission line at 1.740. The spectrum of point (4) in the 1050°C sample shows only a weak phosphorus signal and instead aluminium, silicon and oxygen signals, which can be attributed to residual Al_2O polishing particles accumulating in this area [96]. These residual Al_2O polishing particles were found in some areas by higher magnification SEM. This shows that thresholding the images for segmentation of SEM micrographs is sensitive to errors and artefacts, as it is especially difficult to separate the dark gray secondary phase, pores and pores partially filled by the polishing material.

Table 5.2: Quantification of spectra from the three regions marked in Figure 5.3 and 5.4. For comparison, theoretical values are given for $(Li_{1.3}Al_{0.3}Ti_{1.7}(PO_4)_3$ (excluding lithium as it cannot be detected by EDS) and $AlPO_4$.

STEM	**Al**	**Ti**	**P**	**O**
Area 1 LATP 950°C	17.57	0.02	17.16	65.25
Area 2 LATP 950°C	2.28	11.52	20.67	65.52
Area 3 LATP 1050°C	0.09	0.02	21.07	78.82
Theoretical	Al	Ti	P	O
$(Li_{1.3})Al_{0.3}Ti_{1.7}(PO_4)_3$	1.76	10.00	17.65	70.59
$AlPO_4$	16.67	0.00	16.67	66.67
$(Li_3)PO4$	-	-	20	80

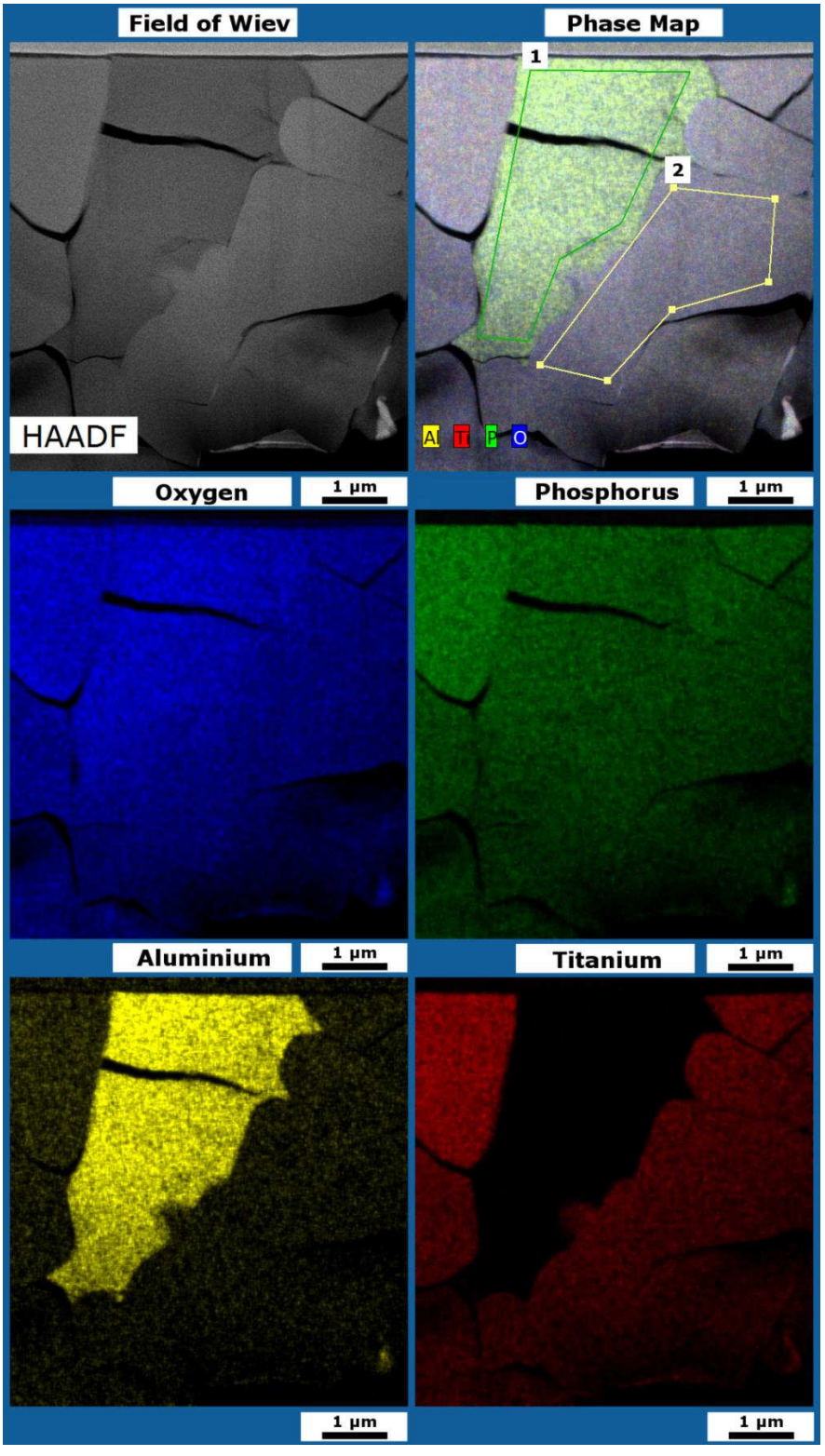

Figure 5.3: STEM image of LATP (950 °C) with simultaneously acquired EDS elemental maps. The maps of aluminium, titanium, phosphorus, and oxygen are displayed.

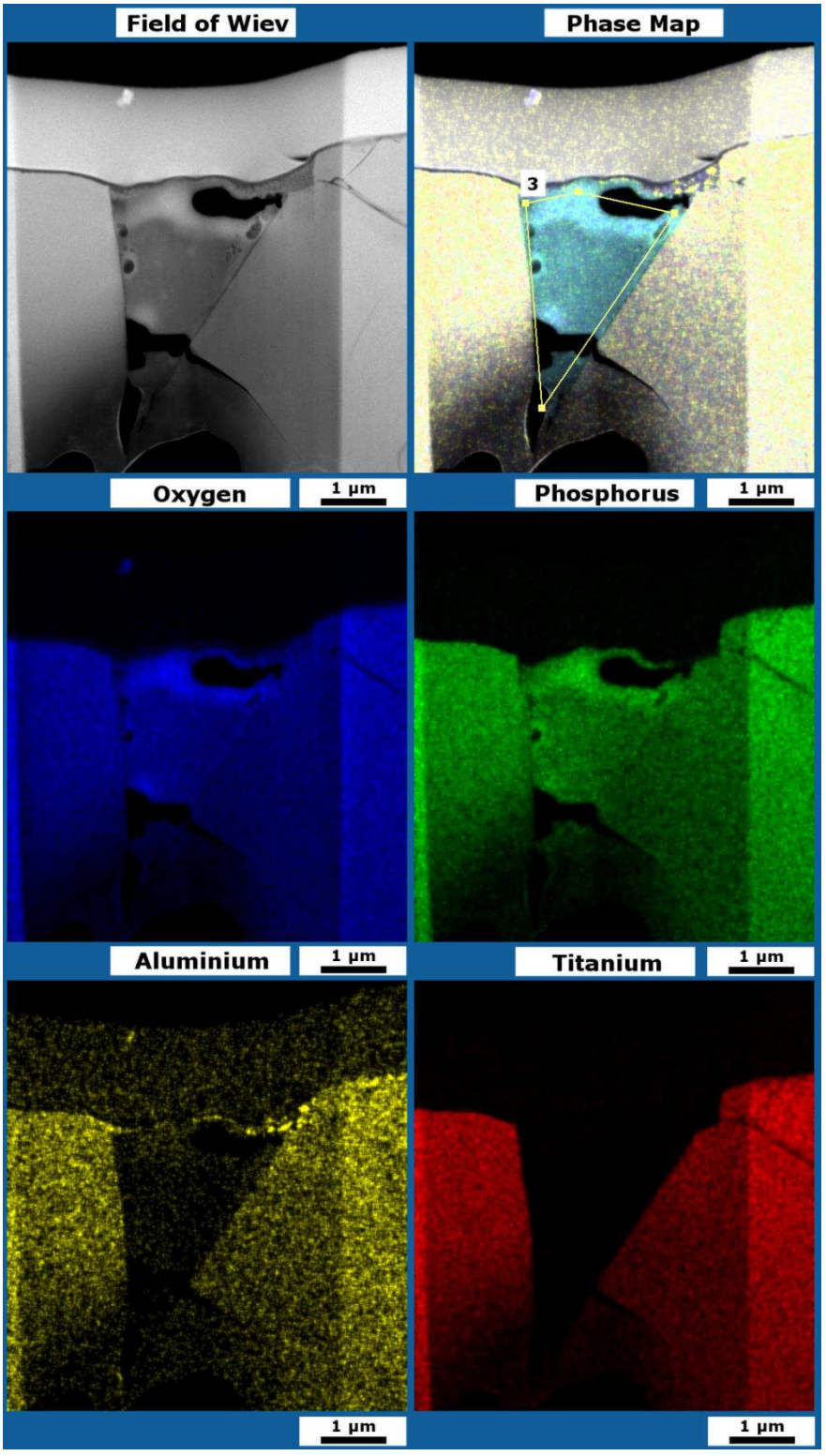

Figure 5.4: STEM image of LATP (1050 °C) with simultaneously acquired EDS elemental maps. The maps of aluminium, titanium, phosphorus, and oxygen are displayed.

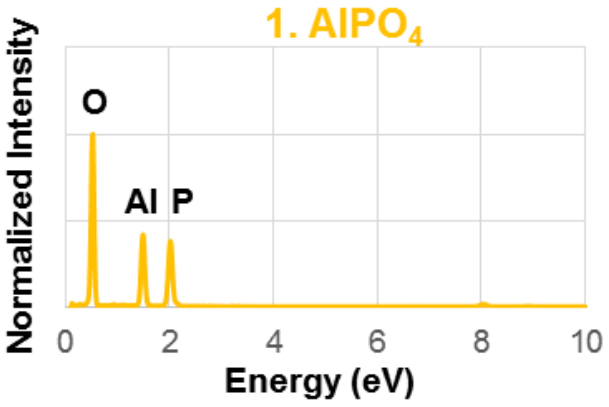

(a)

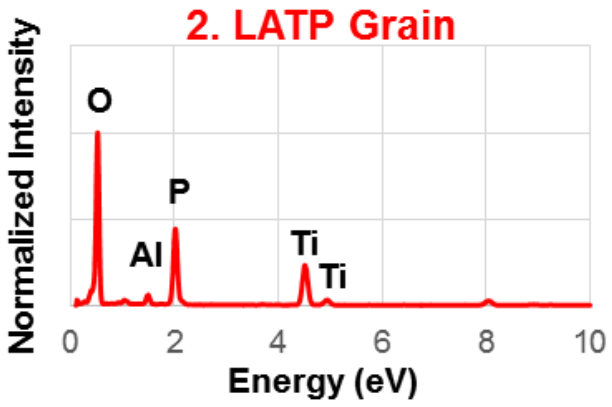

(b)

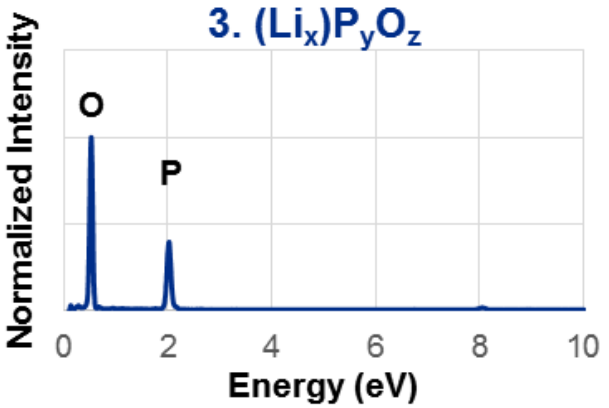

(c)

Figure 5.5: Spectra extracted from three regions for different phases from Figures 5.3 and 5.4.

In the recent literature, mainly $AlPO_4$ and TiO_2 are mentioned as secondary phases [79][80] based on XRD and SEM results. TiO_2 regions were not observed in SEM studies. The secondary phase in point (2) can be attributed to aluminium phosphate even though the quantification of SEM-EDS spectra gives deviating results, with some titanium content and phosphorus:oxygen ratio differing from 1:4. From the morphology, this phase appears rather amorphous in the SEM, which was also found in TEM.

Aono *et al.* mention $Li_4P_2O_7$ and LiO_2 as decomposition products if lithium salts are added as binders [30]. In our case, $Li_4P_2O_7$ is possible as well as any other phosphates. Li_3PO_4 and $AlPO_4$ are not miscible; however, they have a eutectic point at 933°C with 61 % Li_3PO_4 [103]. This eutectic point could also explain the observation of the non-completed sintering of the sample sintered at the temperature of 900°C. Some but rather poor ionic conductivity in crystalline lithium monophosphates has been reported [104]. As stated by Aono *et al.* lithium phosphate secondary phase could aid as binder increasing the lithium-ion conductivity at the grain boundaries [30].

For the secondary phases, the influence of the excitation/escape volume comes even more into account. Titanium with Kα emission line at ≈ 4.5 keV will have the largest volume and the amount of titanium will be rather overestimated, as titanium Kα emission lines can be excited in and escape from neighbouring as well as underlying LATP grains. For oxygen with Kα emission line at ≈ 0.525 keV, this is rather the opposite. Oxygen is only detectable close to the surface. Unfortunately, titanium L emission lines overlap with the oxygen Kα emission lines impeding a quantification based only on titanium Lα and oxygen Kα emission lines.

Because of the fact that SEM-EDS quantification suffers from the difference in excitation/escape volume for the different elements impeding a quantification/phase assignment, additional STEM-EDS was performed on a FIB cut TEM-lamella of samples sintered at 950 and 1050 °C. Figure 5.3 and Figure 5.4 show

the single elemental maps of aluminium, titanium, phosphorus and oxygen as well as the overlay of the aluminium, titanium, phosphorus and oxygen maps to the HAADF-micrographs. Oxygen, phosphorus, aluminium and titanium maps are shown in blue, green, yellow and red respectively. In each of these mapping studies, these areas were selected in a manner that each area shows a close-up view of a secondary phase region. In addition to the EDS elemental mapping studies, EDS spectra were extracted from the three different regions marked in Figures 6.3 and 6.4. These three different regions can be clearly distinguished in consistency with SEM observations. These three regions have been picked for quantitative analysis of the spectra.

Spectra belonging to the marked regions are provided in Figure 5.5 and the associated elements of spectral peaks are marked above the spectral peaks. The region (1) only contains oxygen, aluminium and, phosphorus, which is obvious from the maps. Unlike the EDS studies carried out by SEM, titanium Kα (Kα1 at 4.51084 keV and Kα2 at 4.50486 keV) and titanium Kβ ($K\beta_1$ 4.93181 keV), titanium Lα (Lα1 at 0.4522 keV and Lα2 at 0.4522 keV), titanium Lβ (Lβ1 at 0.4584 keV) emission lines were not observed for this phase. This is because of the thin TEM sample, so no underlying volume is probed unlike in SEM. Region (2) in Figure 5.3 contains oxygen, aluminium, phosphorus, titanium. In the spectrum of the region (3), only phosphorous and oxygen emission lines are present.

Related quantifications of the above-mentioned spectra are given in table 5.2. Theoretical values are also provided for comparison beneath the quantifications. For the grain (region two), similar deviations from the nominal composition are observed as in SEM confirming these results. Quantification of the aluminium-rich area (region one) gives results matching very well with $AlPO_4$ confirming that the bright secondary phase is $AlPO_4$. Quantification of the spectra belonging to the third phase (region three) is containing mainly phosphorus and oxygen in a ratio of 1:4. Therefore, for the third phase a (lithium) phosphate [105] is assumed which will be

named as $(Li_x)P_yO_z$. Lithium is possible, but in the limitations of EDS and beam damage during electron energy-loss spectroscopy (EELS) investigations, it was not detected. While looking at the Figure 5.4, beam damage in this secondary phase can be recognized. During FIB preparation, this secondary phase is the most sensitive. On the other hand, LATP is the most stable and $AlPO_4$ secondary phase shows beam damage but not as much/quickly as $(Li_x)P_yO_z$. Also, some amount of aluminium may be present in this approximately amorphous phase. Ions of potassium, magnesium as well as aluminium in phosphate glasses have been reported [102][106]. From the close-up view of TEM studies, it can be seen that $AlPO_4$ secondary phase regions exhibit cracks or defects. Waetzig *et al.* as well reported that $AlPO_4$ secondary phase regions and $AlPO_4$-LATP grain interfaces are the sources of crack formation [80]. In addition to this, in $(Li_x)P_yO_z$, holes are burned by the beam which shows that secondary phases are not as stable as the primary LATP phase.

The main phases which are considered by us are LATP, $AlPO_4$ and (lithium) phosphate, and pores. The residual Al_2O_3 polishing particles sometimes observed in SEM, mainly on the sample sintered at 1050°C, are attributed to porosity as they favourably accumulate in pores [96]. Other secondary phases as reported in the literature, such as TiO_2 [50][79][80][92] were not observed in our EDS analyses both by SEM and TEM.

5.2. Elemental/phase mapping

5.2.1. Parameter search for elemental/phase mapping

In a similar manner to the three different regions in the STEM-EDS elemental maps, EDS elemental maps obtained in the SEM providing a larger field of view can be used for quantitative phase analysis. $Li_{1+x}Al_xTi_{2x}(PO_4)_3$ (LATP), as the chemical formula suggests, is composed of lithium, aluminium, titanium, phosphorus, and oxygen. On the other hand, EDS is not capable of detecting lithium. Therefore,

elemental maps for aluminium, titanium, phosphorus, and oxygen were recorded at 10 kV to enable titanium-mapping using titanium Kα ($K\alpha_1$ at 4.51084 kV and $K\alpha_2$ at 4.50486 kV) and titanium Kβ ($K\beta_1$ 4.93181 kV) emission lines, avoiding deconvolution of titanium Lα ($L\alpha_1$ at 0.4522 kV and $L\alpha_2$ at 0.4522 kV), titanium Lβ ($L\beta_1$ at 0.4584 kV) emission lines and oxygen Kα ($K\alpha_1$ at 0.5249 kV) emission line [107].

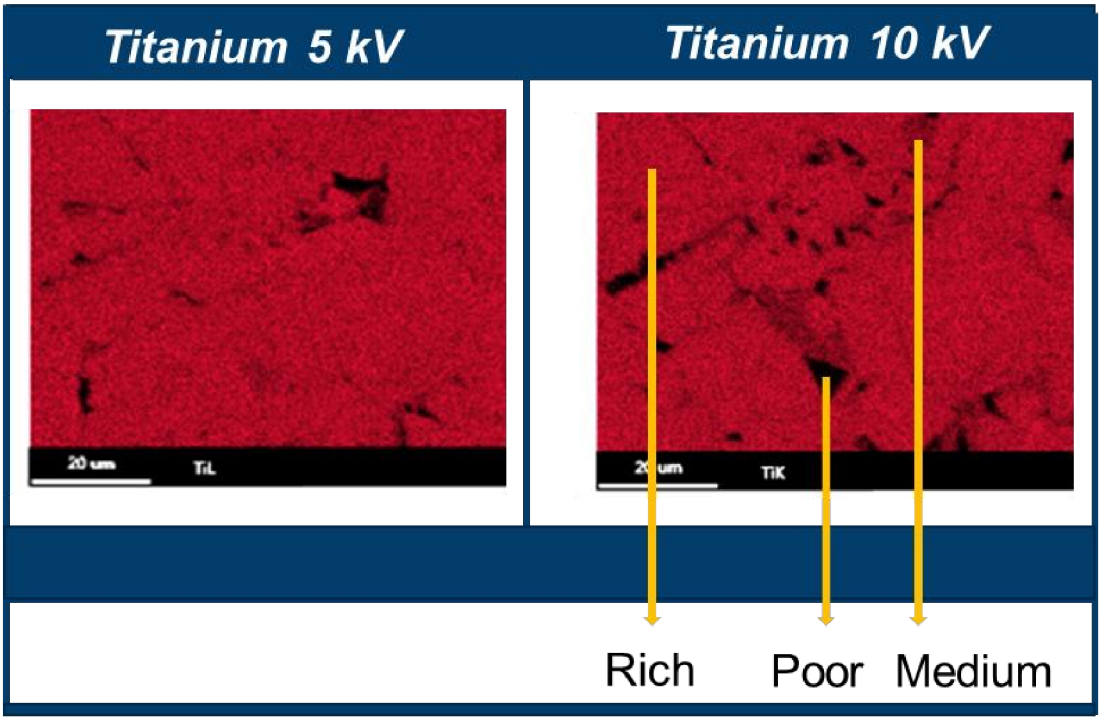

Figure 5.6: Correlative titanium maps of LATP sintered at 1100 °C from the same positions of the sample acquired at 5 kV and 10 kV.

A correlative comparison of 5 kV and 10 kV titanium maps of LATP sintered at the temperature of 1100 °C are provided from the same position of the sample in Figure 5.6. Elementally rich, poor and medium regions are shown for comparison. Because of the fact that the titanium Lα (Lα1 at 0.4522 kV and Lα2 at 0.4522 kV), titanium Lβ (Lβ1 at 0.4584 kV) emission lines and oxygen Kα (Kα1 at 0.5249 kV) emission line partially overlaps, titanium map acquired at 5 kV is not as informative

as the titanium map acquired at 10 kV. Despite the fact that the titanium map acquired at 10 kV clearly shows the regions with different intensities such that elementally rich, elementally medium and elementally poor regions, the titanium map acquired at 5 kV does not differentiate these regions in a clear manner.

Despite the achievable higher resolution of micrographs via increasing the accelerating voltage, LATP ceramic samples commence degrading under electron beam at high accelerating voltages. Therefore, there is a trade-off between getting micrographs with a high resolution and also avoiding the sample damage under electron beam.

5.2.2. Image segmentation and phase map reconstruction recipe from correlative EDS elemental maps

The idea is to make use of the correlative EDS elemental maps for oxygen, phosphorus, aluminium, and titanium from the same position of the sample. Therefore, all these elemental maps must be adjusted in a manner that they overlay on top of each other. For this purpose, the edges of the micrographs are cropped for all elemental maps, and these maps were adjusted overlaying on top of each other after cropping as mentioned.

Segmentation is basically based on assigning labels to image pixels which is responsible for identifying and separating objects in a micrograph. The four EDS elemental maps for oxygen, phosphorus, aluminium and titanium (shown in the left column of Figure 5.8) were segmented into low, medium and high-intensity regions representing the low, medium and high elemental content as shown in the centre column of Figure 5.8. Therefore, there are potentially three different regions exhibiting different intensities.

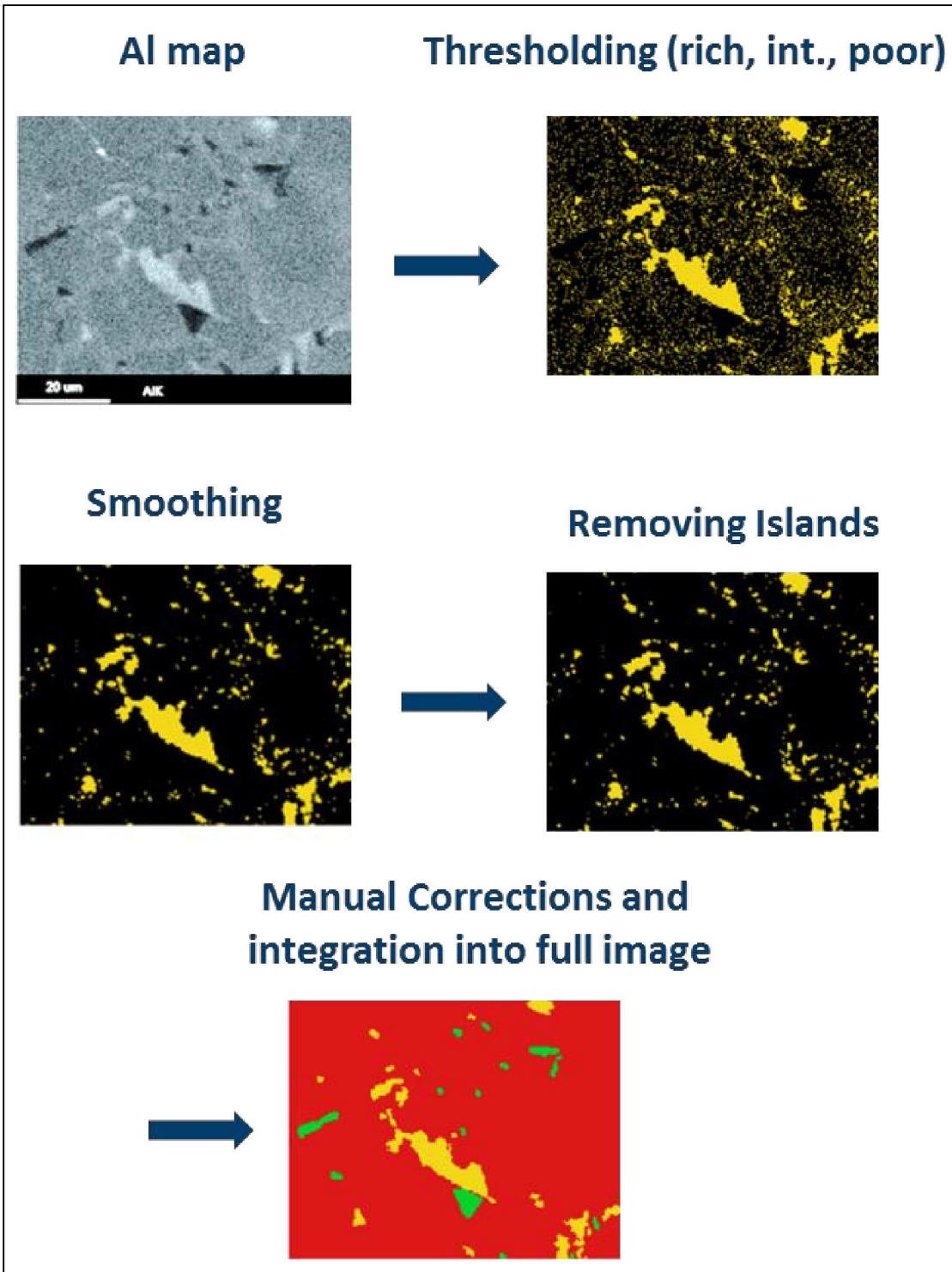

Figure 5.7: Schematic diagram showing the functions employed during the course of image segmentation: thresholding, smoothing and removing islands.

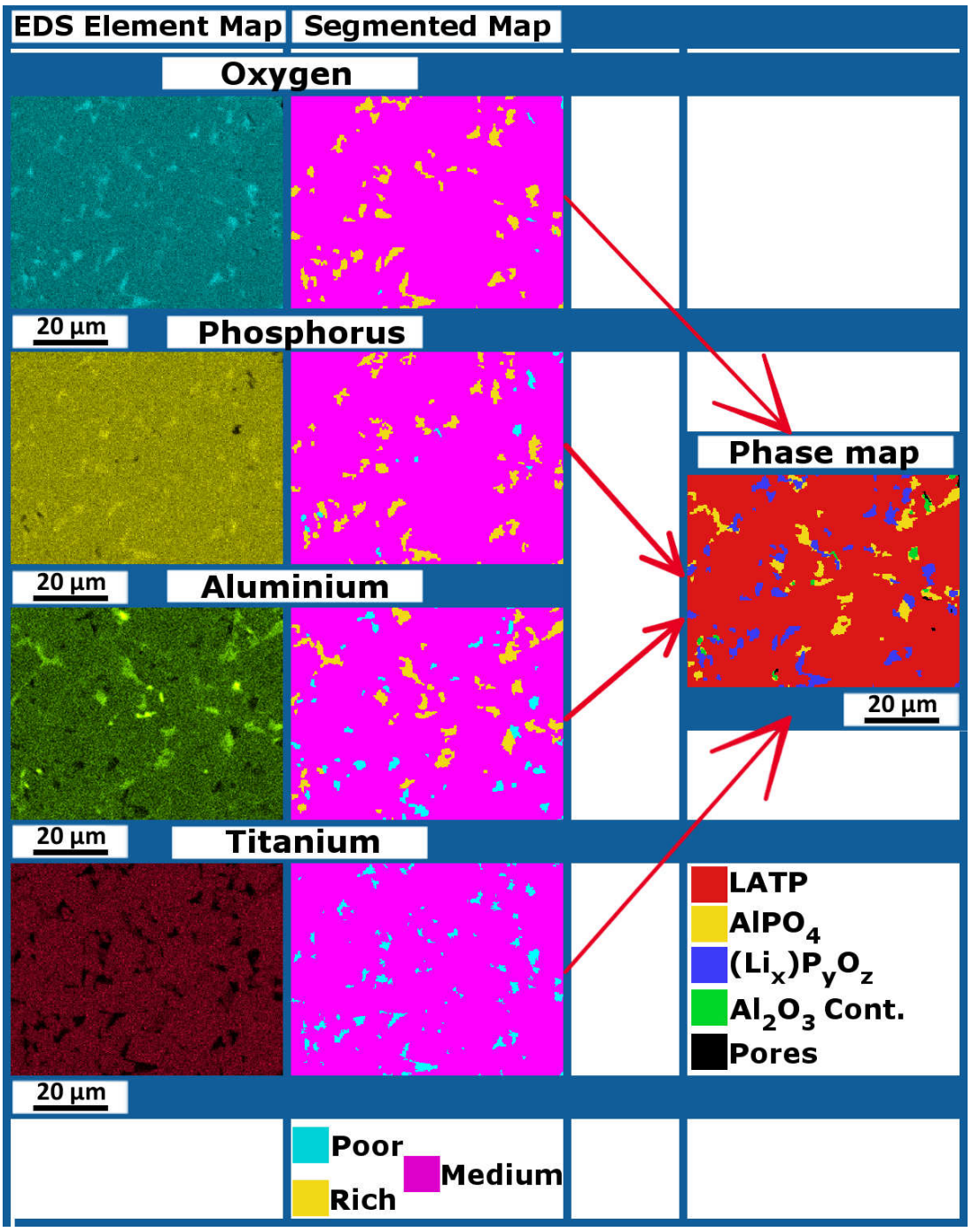

Figure 5.8: SEM-EDS elemental maps of LATP sample sintered at 1000 °C (left column). Segmentation of each elemental map into regions with poor (cyan), medium (magenta) and rich (yellow) elemental content (centre column). Phase map generated from the image analysis of single elemental maps (right column).

In order to clearly differentiate the elementally rich, medium and poor regions, the colours of CMYK colour model were used during the course of image segmentation. CMYK refers to the four inks used in some of the colour printing: cyan, magenta, yellow, and key (black). Black is called as key due to the fact that the combination of the aforementioned colours produces black colour. Elementally rich regions are depicted with yellow, medium regions are shown in magenta, and elementally pour regions are depicted with cyan.

After different regions with different intensities are determined, "remove islands" and/or "smooth" functions can be employed. Remove islands function removes the points or areas smaller than a defined pixel number. Smooth function smoothens the outline of all objects (by changing the assignment of pixels close to the outline). Depending on the image and the effectiveness of the thresholding, smoothing and removing islands, these methods were applied consecutively. The order which of these functions should be used firstly depends on the image to be analysed.

After the above-mentioned procedures are completed, different intensity regions are almost clearly separated, and only little amount of manual corrections is required. This procedure is shown in a schematic in Figure 5.7 One important point which should be taken into consideration for the case of "elementally rich" regions is the edge effect observed near the pores for the oxygen maps. This is the case for the oxygen K-line (and titanium L lines) due to the low energy of the oxygen Kα line. The map includes topographic effects, as edges pointing towards the detector will exhibit higher counts. Such areas were removed during the course of manual corrections.

By using these regions of high, low, and intermediate content for the four different elements, it is now possible to attribute the regions to the four different phases. The Avizo® software allows to cross check the assignment made on one map with all other elemental maps as well as the SE and BSE micrographs. It turned

out that the oxygen map is very well suited to retrieve the $(Li_x)P_yO_z$-regions as well as the pores. Therefore, mainly oxygen maps were used for the detection of pores. $(Li_x)P_yO_z$-regions are also well represented in Phosphorous maps. The phosphorus map also aids in identifying polishing particles as they do not contain phosphorus. The aluminium map highlights the aluminium phosphate regions. In this way, the overall phase maps are retrieved. At the final state, there should be five different regions: LATP main phase regions, $AlPO_4$ secondary phase regions, $(Li_x)P_yO_z$ secondary phase regions, pores and residual Al_2O_3 polishing particles. Because of the fact that the polishing particles preferentially accumulate in pores and grains boundaries, such regions are attributed to porosity. Grain boundaries were not included as a separate phase in this study.

5.3. Quantitative analysis of phase contents

The novel image segmentation and phase map reconstruction recipe for quantitative phase map analyses were used in order to retrieve information and provide a better understanding on the temperature dependent phase evolution, formation mechanism of different secondary phases and their connection with the chemistry of grains as well as correlation between these factors and the electrical properties of LATP ceramic samples.

Exemplary final phase maps are shown in Figure 5.9 for the four sintering temperatures 950 °C, 1000 °C, 1050 °C and 1100 °C. For each sintering temperature, four such different regions were analysed (Exemplary analyses are shown in Figure 5.9). For each region, four such EDS elemental maps of oxygen, phosphorus, aluminium, and titanium were analysed making a total of sixteen maps for each of the sintering temperature. Total areas of 2640 μm^2, 16508 μm^2, 16508 μm^2, 16508 μm^2 were analysed for the sintering temperatures of 950 °C, 1000 °C, 1050 °C and 1100 °C respectively. Naturally, EDS elemental map studies were carried out with a higher magnification at 950 ^oC because of the fact that all the microstructural components are smaller at this temperature, and low-magnification map analyses

would not be useful at that temperature. EDS showed the presence of crystalline LATP-grains (red), $AlPO_4$ secondary phase regions (yellow), (lithium) phosphate $(Li_x)P_yO_z$ secondary phase regions (blue), residual Al_2O polishing particles (green) and pores (black).

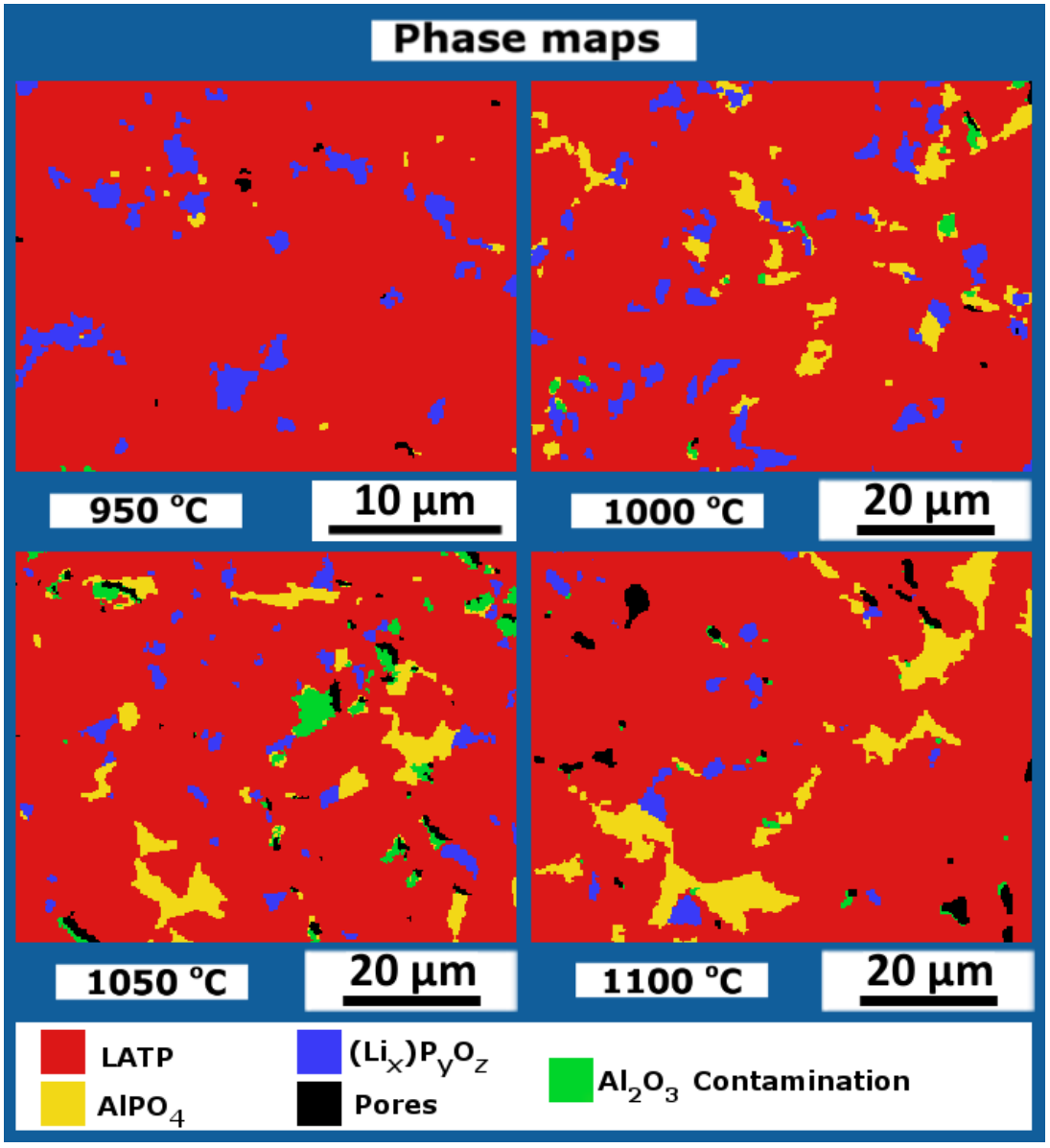

Figure 5.9: Phase maps of LATP ceramic samples for the sintering temperatures of between 950 and 1100°C.

Qualitatively, the evolution of the phase maps shows that at the sintering temperature of 950 °C, secondary phase content is mainly predominated by $(Li_x)P_yO_z$ secondary phase regions while small amount of $AlPO_4$ secondary phase regions are present. Also, the size of $(Li_x)P_yO_z$ secondary phase regions are a lot bigger compared to the size of $AlPO_4$ secondary phase regions. At the sintering temperature of 1000 °C, both the size and amount of $(Li_x)P_yO_z$ secondary phase regions decrease while an accompanying increase in the size and amount of $AlPO_4$ secondary phase regions is observed. $AlPO_4$secondary phase regions commence predominating over $(Li_x)P_yO_z$ secondary phase regions both in size and amount at the sintering temperature of 1050 °C. Eventually, huge blocks of $AlPO_4$ secondary phase regions are formed while most of the $(Li_x)P_yO_z$ secondary phase regions are consumed at the sintering temperature of 1100 °C.

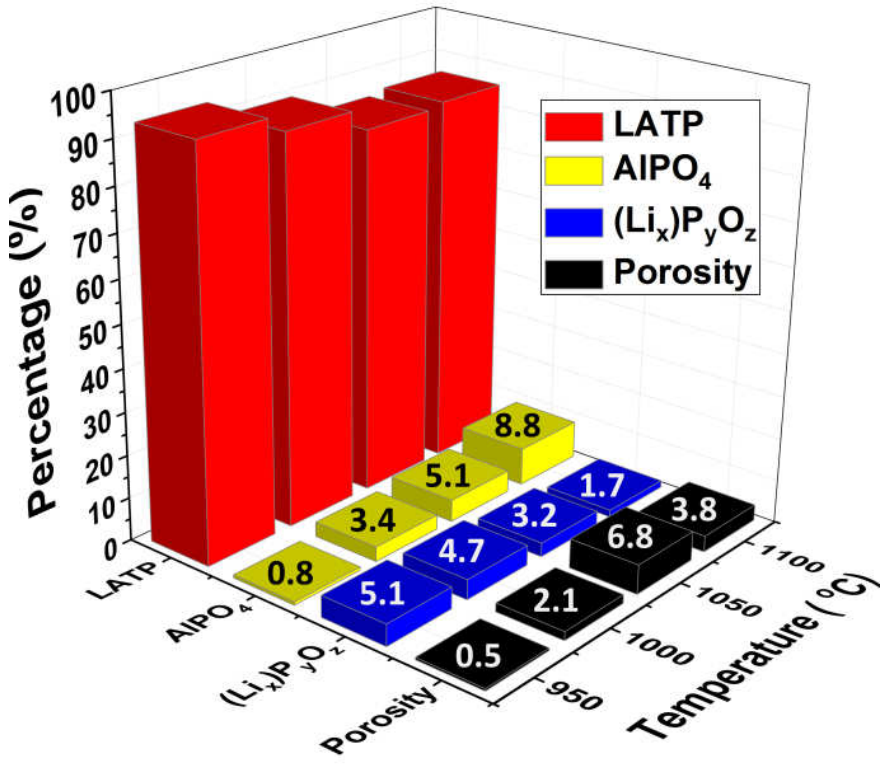

Figure 5.10: Quantification of phases retrieved from phase map analyses.

From the coverage in analysed maps, the quantitative phase content was extracted and is shown in Figure 5.10. The same colours for the same elements are used in Figure 5.10 with the Figure 5.9 for clearance; however, residual Al_2O polishing particles were merged with the pores in this graph. At 950°C sintering temperature, the amount of secondary phases is the lowest and the observed main secondary phase is $(Li_x)P_yO_z$ with ≈ 5%. Only a little amount of $AlPO_4$ (1 %) is found for this sample. With increasing sintering temperature, the amount of $(Li_x)P_yO_z$ decreases, while more and more $AlPO_4$ regions are found. Between the sintering temperature of 1000°C and 1050°C, the main secondary phase changes from $(Li_x)P_yO_z$ to $AlPO_4$. A strong step is then observed in the last step from the sintering temperature of 1050°C to 1100°C, in which the amount of $(Li_x)P_yO_z$ decreases from 3.2 % to 1.7% and the amount of $AlPO_4$ increases from 5.1 % to 8.8 %. With the increasing sintering temperature, not only the amount of $AlPO_4$ secondary phase regions but also their sizes increase while both the amount and size of $(Li_x)P_yO_z$ secondary phase regions decrease. It is also observed that newly most of the formed $(Li_x)P_yO_z$ secondary phase regions are in contact with the $AlPO_4$ secondary phase regions.

The total amount of secondary phases increases as well with increasing sintering temperature. A similar trend is observed for the porosity, but here a maximum is observed for the sample sintered at 1050°, which is the sample in which the residual Al_2O_3 polishing particles were detected. In the other samples, we detected much less of these residual polishing particles. Hence, the quantification of porosity for this sample should be treated with care. The amount of $AlPO_4$ retrieved from the image analyses of EDS elemental maps for different temperatures are comparable with the values obtained from CLSM and SEM image analyses before, but in addition to that, now it was possible to identify and quantify the second secondary phase as well as porosity.

5.4. $AlPO_4$-formation mechanism

The $AlPO_4$-formation mechanism requires sources of aluminium as well as phosphate. LATP grains are the only possible source of aluminium for $AlPO_4$ formation in the material at the beginning. That's why also EDS-spectra of twenty grains from the analysed maps for each sintering temperature were measured. Figure 5.11 displays the sintering temperature dependent evolution of the atomic percentage of aluminium among the elements of LATP apart for lithium (aluminium, titanium, phosphorus, and oxygen) for the four different samples.

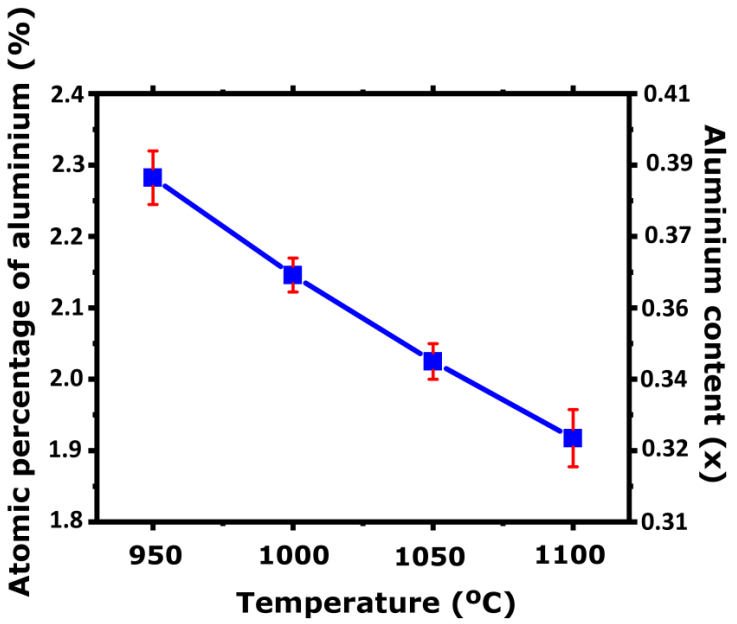

Figure 5.11: Sintering temperature dependent evolution of the atomic percentage of LATP grains.

Equating the determined atomic percentages to the ratio of the aluminium subscript to the sum of the subscripts of the elements of $Li_{1+x}Al_xTi_{2-x}(PO_4)_3$ apart for lithium (aluminium, titanium, phosphorus and oxygen), the aluminium content subscript *x* is found. Data is shown in blue colour and the standard deviations are given in red colour. It is observed that the aluminium-content *x* of LATP bulk

decreases with increasing sintering temperature. This explains the source of aluminium in $AlPO_4$ formation mechanism. In correlation with the strong increase in $AlPO_4$ content from the sintering temperature of 950°C to 1000°C and also for the last step from the sintering temperature of 1050°C to 1100°C, the sharper decreases of aluminium-content in grain stoichiometry are observed at the same temperature steps.

5.5. Effect of phase content on electrical properties

In order to reveal the correlation between the LATP bulk chemistry and the electrical properties of the LATP ceramic samples, impedance data was analysed in addition to the microstructure of LATP ceramic samples. The microstructural information is correlated with the impedance results. In principle, the lithium ion transport taking place inside of the grains should appear as an arc in the impedance data. Due to the fact that the small semicircle in the high-frequency region, which arises from ionic charge transport within the grains, is not resolved, this value is obtained by distribution of relaxation times (DRT) analysis for all LATP samples via using the method reported for the LATP sample sintered at 1100 ^{o}C. The quantification of the impedance data was carried out between $f = 3 \times 10^6$ Hz and $f = 5 \times 10^5$ via employing a distribution of relaxation times analysis in two dimensions (2D-DRT). In this manner, a high resolution in the high frequency range was achieved. The grain resistance R_g and grain boundary resistance R_{gb} are obtained after electrical circuit model (ECM) fitting. The retrieved values with their uncertainties are tabulated in in table 5.3. The grain resistance of LATP ceramic samples increases with the increasing sintering temperature.

Table 5.3: Grain resitance R_g and grain boundary resistance R_{gb} determined by DRT and ECM fitting.

Sintering temperature	R_g (Ω)	ΔR_g (Ω)	R_{gb}	ΔR_g
950°C	19.8	0.3	1041	6
1000°C	26.2	0.4	951	1
1050°C	29.3	1.2	439	1
1100°C	41.8	1.7	639	2

Figure 5.12 shows the grain resistance in relation with the atomic percentage of aluminium in grains. The grain resistance increases continuously with increasing sintering temperature. The composition of the $Li_{1+x}Al_xTi_{2-x}(PO_4)_3$ grains changes upon sintering. On the other hand, the effect of the chemistry of the LATP ceramic samples and aluminium-content x of LATP on the electrical properties of the samples is still a matter of discussion. Takada et al. [70] and Forsyth et al. [69] compared LTP and LATP in their NMR studies, and they found that the partial substitution of titanium by aluminium only results in some minor changes in the line widths, which indicates only a small effect of aluminium content on the lithium ion conductivity of LATP samples.

On the other hand, As reported by Aono *et al.* [17] lithium conductivity is at its maximum for x = 0.3. They found the aluminium-content x via starting chemistry of the samples. Therefore, in that study, there was not a differentiation between the aluminium-content x of LATP bulk and other components such as grain boundaries and secondary phases. Based on single grain contact measurements

Rettenwander *et al.* [26] reported the maximum conductivity for x = 0.4. For this case, they measured the aluminium-content x by atomic emission spectroscopy. Wang *et al.* [108] also carried out NMR studies on LATP samples and they interpreted their results in a manner that that the aluminium-content x of LATP does not have a strong effect on the lithium ion conductivity; however, they also observed the maximum lithium ion conductivity at the aluminium-content x of LATP equal to 0.4.

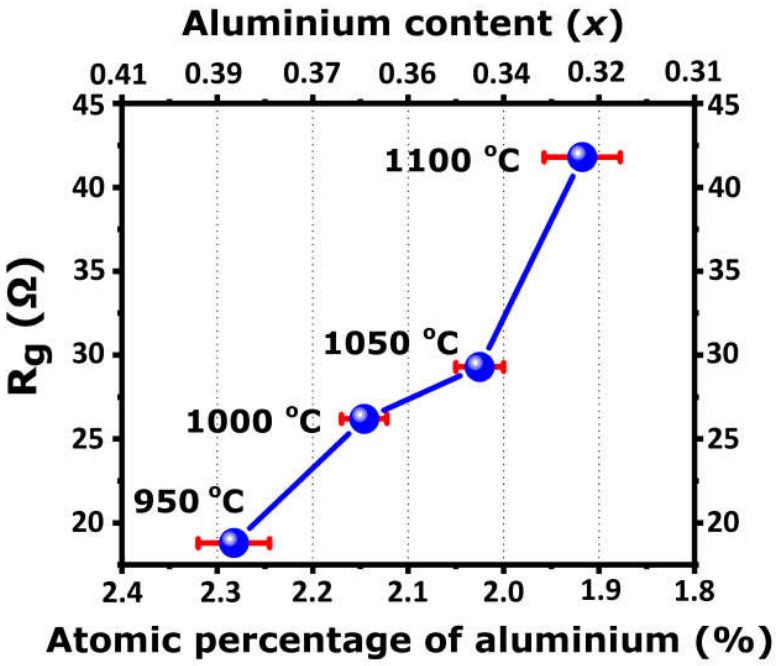

Figure 5.12: The relation between atomic percentage of aluminium in grain stoichiometry and grain resistance. Statistical data are collected from twenty grains from the analysed maps for each sintering temperature. Standard deviations of the data are shown in red.

Aono *et al.* [30] report an improved ionic conductivity due to higher lithium-ion content at the grain boundaries by the addition of binders such as Li_2O and $Li_4P_2O_7$. As discussed before, lithium detection was not possible during this work. If the $(Li_x)P_yO_z$ phase is a lithium containing phosphate, the higher $(Li_x)P_yO_z$-content observed for low sintering temperatures would increase the lithium-ion

concentrations at the grain boundaries and increase their ionic conductivity. $(Li_x)P_yO_z$-regions can serve as a phosphate source, and the decrease in the amount of $(Li_x)P_yO_z$ secondary phase in the course of $AlPO_4$ secondary phase formation underpins this mechanism. This decrease could also explain an increase in the grain boundary resistance measured by impedance spectroscopy. Considering the increasing grain sizes with increasing sintering temperature, the contribution of grain boundary resistance to the total resistance should decrease, as the number of grain boundaries that need to be crossed reduces. This trend is observed from the sintering temperature of 950°C to 1050°C sintering temperature. On the other hand, in the last step to the sintering temperature of 1100°C, the total grain boundary resistance increases (Figure 5.13). One possible explanation for this behaviour would be more cracks in LATP grains as observed by Hupfer *et al.* [79] and Waetzig *et al.* [80]. Another possible explanation for this behaviour is the lower amount of $(Li_x)P_yO_z$ compared to the other sintering temperatures.

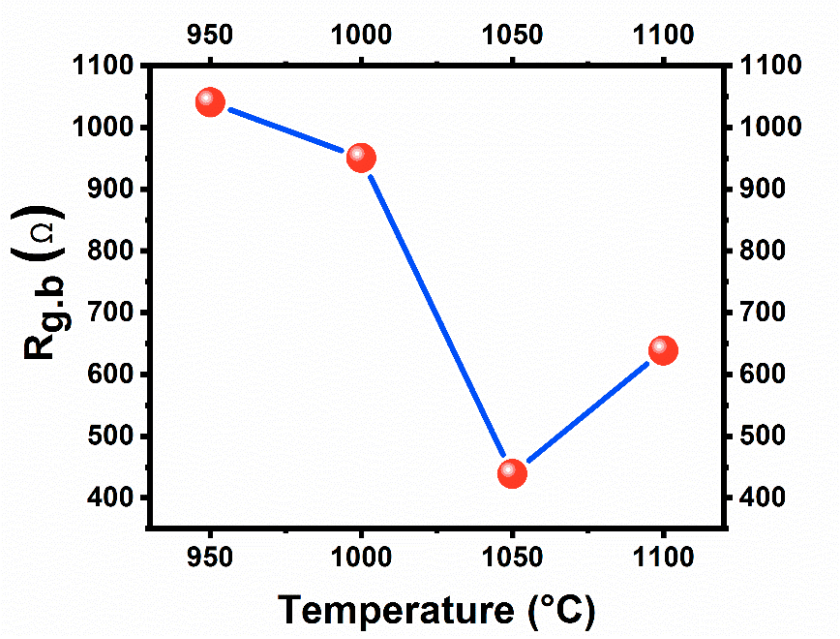

Figure 5.13: Temperature dependent evolution of grain boundary resistance.

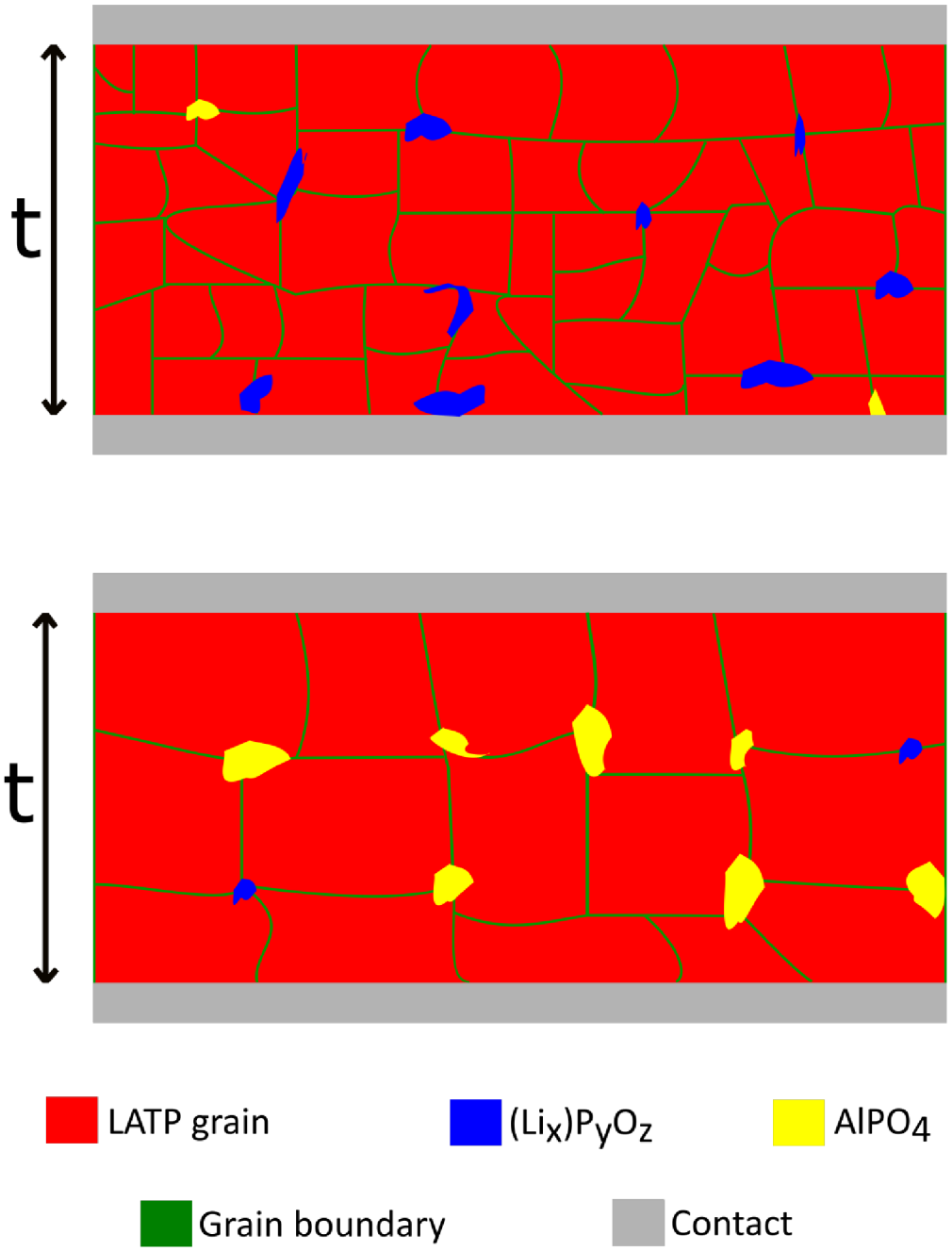

Figure 5.14: Schematic representation of phase evolution of LATP with sintering temperatures of 950 (left) and 1100 °C (right). Grains, grain boundaries, $(Li_x)P_yO_z$ secondary phase regions and $AlPO_4$ secondary phase regions are shown in red, green, blue, yellow, respectively.

Figure 5.14 is a schematic representation of the observed phase evolution in two contacted LATP pellets sintered at 950 °C (left) and 1100 °C (right). LATP grains, grain boundaries, $(Li_x)P_yO_z$ secondary phase regions, $AlPO_4$ secondary phase regions and pellet contacts are depicted in red, green, blue, yellow, and gray in a respective manner. I expect the total lithium ion conductivity to be affected mainly by the grain size, as the total number of grain boundaries decreases with the increasing grain sizes. On the other hand, both the grain and grain boundary conductivity can be affected by the changes in chemistry upon sintering. Up to the sintering temperature of 1100°C, the amount of non-lithium-ion-conductive secondary phases such as $AlPO_4$ is not that high to totally block the lithium ion conduction pathways through the solid electrolyte unless grain boundaries are wetted by $AlPO_4$ secondary phase. This was partially observed in TEM so with a dramatical increase in the amount of $AlPO_4$ secondary phase, wetting of grain boundaries becomes more probable, which can be one possible reason leading to the suppression of a further decrease of total resistance above 1050°C sintering temperature.

5.6. Chapter summary

In this chapter, secondary phase formation mechanism as well as the phase evolution of LATP ceramic pellets sintered at temperatures from 950°C to 1100°C with 50 °C steps were studied by EDS elemental mapping in the SEM in a correlative manner with EDS spectra taken from the different grains so as to provide a better understanding of the secondary phase formation mechanism in LATP ceramic pellets, its direct relation with the evolution of LATP bulk chemistry as well as their correlation with electrical properties LATP ceramic pellets. The evolution of Crystalline LATP-grains, $AlPO_4$ secondary phase regions, (lithium) phosphate $(Li_x)P_yO_z$ secondary phase regions during the course of sintering is analysed and shows the presence of mainly $(Li_x)P_yO_z$ as secondary phase at low sintering temperatures. With increasing temperature, $AlPO_4$ secondary phase is formed and $(Li_x)P_yO_z$ secondary phase is consumed. In addition to this, the aluminium content

inside the LATP grains is reduced because of the fact that they act as an aluminium source. This affects the grain resistance as well as the total resistance.

Chapter 6 : Conclusion

In this thesis study, microstructure-property relation in $Li_{1.3}Al_{0.3}Ti_{1.7}(PO_4)_3$ superionic lithium conducting ceramics were investigated.

LATP ceramic samples are highly brittle, and also they degrade when they are exposed to water. Therefore, in order to enable a non-destructive characterisation of LATP ceramic samples, an all-oil-based metallographic sample preparation route was developed which allows a clear differentiation of different microstructural components on flat LATP ceramic surfaces.

Crystalline LATP-grains, secondary phase regions and pores were observed as microstructural components. CLSM and SEM micrographs indicate that a minimum sintering temperature of 950 °C is required to produce fully sintered samples and before that temperature LATP ceramic samples look more like a loose powder. Secondary phases can be detected by CLSM and SEM in samples sintered at 1000°C and above. Grain size, grain symmetry, the amount of one secondary phase, and contact ratio of grains αcontact are determined both by the analyses of CLSM and SEM micrographs. Grain size increases with increasing sintering temperature. Grain symmetry does not change and the amount of $AlPO_4$ secondary phase increases especially for the last step from 1050 to 1100 °C.

TEM is used so as to estimate grain boundary width and also to identify the amorphous nature of $AlPO_4$ secondary phase. It is shown that $AlPO_4$ secondary phase is not only filling larger intergranular regions, but it is also partially wetting grain boundaries with a few nanometres thin film. Hence, these thin films might be missed in CLSM and SEM micrographs affecting the determination of contact ratio $\alpha_{contact}$. Despite this fact even the contact ratio retrieved from SEM and CLSM images shows the trend of a clear decrease with increasing sintering temperature. Correlating these findings with total resistance determined by impedance spectroscopy measurements leads to the interpretation that the reduced

conduction path length across grain boundaries due to larger grain sizes has the major contribution on the total resistance. The total lithium-ion conductivity increases with increasing sintering temperature with an accompanying increase in grain sizes. On the other hand, at 1100 °C, the negative effects of crack and secondary phase formation reducing the contact ratio of grains $\alpha_{contact}$ come into account as well. Therefore, total resistance of the sample increases in this last step.

In case of a presence of more than one secondary phase and pores, image analysis must tackle the difficulties about distinguishing between these microstructural features. A novel image segmentation and phase map reconstruction recipe for quantitative phase map analyses employing SEM-EDS maps was developed to overcome such difficulties.

Secondary phase formation mechanism as well as phase evolution of LATP ceramic pellets during sintering were studied by EDS elemental mapping in the SEM combined with quantitative analysis of LATP grains. Following microstructural components were observed: Crystalline LATP-grains, $AlPO_4$ secondary phase regions, (lithium) phosphate $(Li_x)P_yO_z$ secondary phase regions and pores. The evolution of these phases during sintering is analysed and shows the presence of mainly $(Li_x)P_yO_z$ as secondary phase at low sintering temperatures. With increasing temperature, $AlPO_4$ is formed and $(Li_x)P_yO_z$ is consumed. Also, the aluminium content inside the LATP grains is reduced, as they act as aluminium source. As the aluminium content of the grains decreases, their conductivity decreases as well. This proved a direct correlation between LATP bulk aluminium content and lithium-ion conductivity excluding any other microstructural effects such as grain boundaries and secondary phases.

It is shown that the microstructural parameters can be conceived as a tool to tune the lithium ion transport properties. Firstly, engineering the grain sizes allows changing the grain to grain boundary volume ratio and paves a way to reduce conduction path length across grain boundaries, which directly results in increased

lithium-ion conductivity. Secondly, independent from any microstructural effect such as grain boundaries and secondary phases, it is shown that aluminium content of LATP bulk directly correlates with LATP bulk lithium-ion conductivity.

List of figures

List of tables

Bibliography

[1] U.S. Energy, International Energy Outlook 2017 Overview, (2017).

[2] British Petroleum, BP Statistical Review of World Energy 2017, Br. Pet. (2017) 1–52. doi:http://www.bp.com/content/dam/bp/en/corporate/pdf/energy-economics/statistical-review-2017/bp-statistical-review-of-world-energy-2017-full-report.pdf.

[3] World Energy Resources | 2016, (2016).

[4] D.J. Wuebbles, A.K. Jain, Concerns about climate change and the role of fossil fuel use, Fuel Process. Technol. 71 (2001) 99–119. doi:10.1016/S0378-3820(01)00139-4.

[5] M.C. Maccracken, Earth's Future Special Section : The rationale for accelerating regionally focused climate intervention research, (2016). doi:10.1002/eft2.164.

[6] ATC - Austrian Technology Corporation GmbH: Energy (Hydropower) Technologies, (n.d.). http://www.atc.or.at/en/scope/energy-hydropower-technologies/ (accessed November 16, 2018).

[7] 1.25 Gigawatts of Solar Thermal Power Approved in California in Past Two Days Will Double US Capacity | TreeHugger, (n.d.). https://www.treehugger.com/renewable-energy/125-gigawatts-of-solar-thermal-power-approved-in-california-in-past-two-days-will-double-us-capacity.html (accessed November 16, 2018).

[8] Germany Launches its Largest Offshore Wind Farm on the North Sea: Bard Offshore 1, (n.d.). http://strangesounds.org/2013/08/germany-launches-its-largest-offshore-wind-farm-on-the-north-sea-bard-offshore-1.html (accessed November 16, 2018).

[9] Belectric discuss German grid stability project as solar-plus-storage goes large | Energy Storage News, (n.d.). https://www.energy-storage.news/blogs/belectric-discuss-german-grid-stability-project-as-solar-plus-storage-goes (accessed November 16, 2018).

[10] J.M. Tarascon, M. Armand, Issues and challenges facing rechargeable lithium batteries., Nature. 414 (2001) 359–67. doi:10.1038/35104644.

[11] B. Nykvist, M. Nilsson, Rapidly falling costs of battery packs for electric vehicles, 5 (2015) 100–103. doi:10.1038/NCLIMATE2564.

[12] T. Sasaki, Memory effect in a lithium-ion battery, Nat. Mater. 12 (2013) 569–575. doi:10.1038/nmat3623.

[13] Y. Wang, W.D. Richards, S.P. Ong, L.J. Miara, J.C. Kim, Y. Mo, G. Ceder, Design principles for solid-state lithium superionic conductors, Nat. Mater. 14 (2015)

1026–1031. doi:10.1038/nmat4369.

[14] P. Bai, J. Li, F.R. Brushett, M.Z. Bazant, Transition of lithium growth mechanisms in liquid electrolytes, Energy Environ. Sci. 9 (2016) 3221–3229. doi:10.1039/c6ee01674j.

[15] M. Ogawa, K. Yoshida, K. Harada, All-solid-state lithium batteries with wide operating temperature range, SEI Tech. Rev. (2012) 88–90.

[16] J.B. Goodenough, K.S. Park, The Li-ion rechargeable battery: A perspective, J. Am. Chem. Soc. 135 (2013) 1167–1176. doi:10.1021/ja3091438.

[17] Y. Zhu, X. He, Y. Mo, Origin of Outstanding Stability in the Lithium Solid Electrolyte Materials: Insights from Thermodynamic Analyses Based on First-Principles Calculations, ACS Appl. Mater. Interfaces. 7 (2015) 23685–23693. doi:10.1021/acsami.5b07517.

[18] J. Janek, W.G. Zeier, A solid future for battery development, Nat. Energy. 1 (2016) 1–4. doi:10.1038/nenergy.2016.141.

[19] P. Jakes, J. Granwehr, H. Kungl, R.-A. Eichel, Mixed Ionic–Electronic Conducting Li4Ti5O12 as Anode Material for Lithium Ion Batteries with Enhanced Rate Capability – Impact of Oxygen Non-Stoichiometry and Aliovalent Mg2+-Doping Studied by Electron Paramagnetic Resonance, Zeitschrift Für Phys. Chemie. 229 (2015). doi:10.1515/zpch-2015-0618.

[20] J.B. Bates, N.J. Dudney, B. Neudecker, A. Ueda, C.D. Evans, Thin-film lithium and lithium-ion batteries, Solid State Ionics. 135 (2000) 33–45. doi:10.1016/S0167-2738(00)00327-1.

[21] H. Aono, E. Sugimoto, Y. Sadaoka, N. Imanaka, G. Adachi, Ionic Conductivity of Solid Electrolytes Based on Lithium Titanium Phosphate, J. Electrochem. Soc. 137 (1990) 1023. doi:10.1149/1.2086597.

[22] A.C. Luntz, J. Voss, K. Reuter, Interfacial Challenges in Solid-State Li Ion Batteries, J. Phys. Chem. Lett. 6 (2015) 4599–4604. doi:10.1021/acs.jpclett.5b02352.

[23] T. Kato, R. Yoshida, K. Yamamoto, T. Hirayama, Effects of sintering temperature on interfacial structure and interfacial resistance for all-solid-state rechargeable lithium batteries, 325 (2016) 584–590. doi:10.1016/j.jpowsour.2016.06.068.

[24] J.C. Bachman, S. Muy, A. Grimaud, H.H. Chang, N. Pour, S.F. Lux, O. Paschos, F. Maglia, S. Lupart, P. Lamp, L. Giordano, Y. Shao-Horn, Inorganic Solid-State Electrolytes for Lithium Batteries: Mechanisms and Properties Governing Ion Conduction, Chem. Rev. 116 (2016) 140–162. doi:10.1021/acs.chemrev.5b00563.

[25] U. V. Alpen, A. Rabenau, G.H. Talat, Ionic conductivity in Li3N single crystals, Appl. Phys. Lett. 30 (1977) 621–623. doi:10.1063/1.89283.

[26] Y. Inaguma, C. Liquan, M. Itoh, T. Nakamura, T. Uchida, H. Ikuta, M. Wakihara, High ionic conductivity in lithium lanthanum titanate, Solid State Commun. 86 (1993) 689–693. doi:10.1016/0038-1098(93)90841-A.

[27] R. Murugan, V. Thangadurai, W. Weppner, Fast lithium ion conduction in garnet-type Li7La 3Zr2O12, Angew. Chemie - Int. Ed. 46 (2007) 7778–7781. doi:10.1002/anie.200701144.

[28] N. Kamaya, K. Homma, Y. Yamakawa, M. Hirayama, R. Kanno, M. Yonemura, T. Kamiyama, Y. Kato, S. Hama, K. Kawamoto, A. Mitsui, A lithium superionic conductor, Nat. Mater. 10 (2011) 682–686. doi:10.1038/nmat3066.

[29] H. Wada, M. Menetrier, A. Levasseur, P. Hagenmuller, Preparation and ionic conductivity of new B2S3-Li2S-LiI glasses, Mater. Res. Bull. 18 (1983) 189–193. doi:10.1016/0025-5408(83)90080-6.

[30] H. Aono, Ionic Conductivity of Solid Electrolytes Based on Lithium Titanium Phosphate, J. Electrochem. Soc. 137 (1990) 1023. doi:10.1149/1.2086597.

[31] H. Aono, E. Sugimoto, Y. Sadaoka, N. Imanaka, G. ya Adachi, Ionic conductivity and sinterability of lithium titanium phosphate system, Solid State Ionics. (1990). doi:10.1016/0167-2738(90)90282-V.

[32] S. Wenzel, T. Leichtweiss, D. Krüger, J. Sann, J. Janek, Interphase formation on lithium solid electrolytes - An in situ approach to study interfacial reactions by photoelectron spectroscopy, Solid State Ionics. 278 (2015) 98–105. doi:10.1016/j.ssi.2015.06.001.

[33] S. Xuefu, H. Nemori, S. Mitsuoka, P. Xu, M. Matsui, Y. Takeda, O. Yamamoto, N. Imanishi, High Lithium-Ion-Conducting NASICON-Type Li1+xAlxGeyTi2−x−y(PO4)3 Solid Electrolyte, Front. Energy Res. 4 (2016) 2–10. doi:10.3389/fenrg.2016.00012.

[34] P. Zhang, M. Matsui, A. Hirano, Y. Takeda, O. Yamamoto, N. Imanishi, Water-stable lithium ion conducting solid electrolyte of the Li1.4Al0.4Ti1.6 - XGex(PO4)3system (x = 0-1.0) with NASICON-type structure, Solid State Ionics. 253 (2013) 175–180. doi:10.1016/j.ssi.2013.09.022.

[35] S. Yu, A. Mertens, H. Tempel, R. Schierholz, H. Kungl, R.A. Eichel, Monolithic All-Phosphate Solid-State Lithium-Ion Battery with Improved Interfacial Compatibility, ACS Appl. Mater. Interfaces. 10 (2018) 22264–22277. doi:10.1021/acsami.8b05902.

[36] R.D. Shannon, Revised effective ionic radii and systematic studies of interatomic distances in halides and chalcogenides, Acta Crystallogr. Sect. A. 32 (1976) 751–767. doi:10.1107/S0567739476001551.

[37] M. Catti, A. Comotti, S. D. Blas, R. M. Ibberson, Extensive lithium disorder in Li1.5Fe0.5Ti1.5(PO4)3 Nasicon by neutron diffraction, and the Li11xFexTi22x(PO4)3 phase diagram, (2012) 21602–21607. doi:10.1039/c2jm34227h.

[38] A. Aatiq, M. Ménétrier, L. Croguennec, E. Suard, C. Delmas, On the structure of Li3Ti2(PO4)3, J. Mater. Chem. 12 (2002) 2971–2978. doi:10.1039/b203652p.

[39] E. Dashjav, F. Tietz, Neutron Diffraction Analysis of NASICON-type Li1+xAlxTi2-xP3O12, Zeitschrift Für Anorg. Und Allg. Chemie. 640 (2014) 3070–3073. doi:10.1002/zaac.201400195.

[40] K. Arbi, W. Bucheli, R. Jiménez, J. Sanz, High lithium ion conducting solid electrolytes based on NASICON Li1+xAlxM2-x(PO4)3 materials (M = Ti, Ge and 0 ≤ x ≤ 0.5), J. Eur. Ceram. Soc. 35 (2015) 1477–1484. doi:10.1016/j.jeurceramsoc.2014.11.023.

[41] E.R. Losilla, M.A.G. Aranda, M. Martinez-Lara, S. Bruque, Reversible Triclinic-Rhombohedral Phase Transition in LiHf 2 (PO 4) 3 : Crystal Structures from Neutron Powder Diffraction, Chem. Mater. 9 (1997) 1678–1685. doi:10.1021/CM970078N.

[42] M. Catti, S. Stramare, R. Ibberson, Lithium location in NASICON-type Li+conductors by neutron diffraction. I. Triclinic α'-LiZr2(PO4)3, Solid State Ionics. 123 (1999) 173–180. doi:10.1016/S0167-2738(99)00089-2.

[43] A. Aatiq, C. Delmas, A. El Jazouli, Structural and electrochemical study of Li0.5Mn0.5Ti1.5Cr0.5(PO4)3, J. Solid State Chem. 158 (2001) 169–174. doi:10.1006/jssc.2001.9088.

[44] C.M. Burba, R. Frech, Vibrational spectroscopic study of lithium intercalation into LiTi2(PO4)3, Solid State Ionics. 177 (2006) 1489–1494. doi:10.1016/j.ssi.2006.07.015.

[45] H. Aono, E. Sugimoto, Y. Sadaoka, N. Imanaka, G. Adachi, Ionic Conductivity of the Lithium Titanium Phosphate (Lil+xMxTi2-x(PO4)3, M = Al, Sc, Y, and La) Systems, J. Electrochem. Soc. 136 (1989) 590–591. doi:10.1149/1.2096693.

[46] M. Kotobuki, M. Koishi, Y. Kato, Preparation of Li1.5Al0.5Ti1.5(PO4)3 solid electrolyte via a co-precipitation method, Ionics (Kiel). 19 (2013) 1945–1948. doi:10.1007/s11581-013-1000-4.

[47] P. Zhang, H. Wang, Q. Si, M. Matsui, Y. Takeda, O. Yamamoto, N. Imanishi, High lithium ion conductivity solid electrolyte of chromium and aluminum co-doped NASICON-type LiTi2(PO4)3, Solid State Ionics. 272 (2015) 101–106. doi:10.1016/j.ssi.2015.01.004.

[48] M. Pérez-Estébanez, J. Isasi-Marín, D.M. Többens, A. Rivera-Calzada, C. León, A systematic study of Nasicon-type Li1+xMxTi2−x(PO4)3 (M: Cr, Al, Fe) by neutron diffraction and impedance spectroscopy, Solid State Ionics. 266 (2014) 1–8. doi:10.1016/j.ssi.2014.07.018.

[49] E.C. Bucharsky, K.G. Schell, A. Hintennach, M.J. Hoffmann, Preparation and characterization of sol-gel derived high lithium ion conductive NZP-type ceramics Li1+xAlxTi2-x(PO4)3, Solid State Ionics. 274 (2015) 77–82.

doi:10.1016/j.ssi.2015.03.009.

[50] T. Hupfer, E.C. Bucharsky, K.G. Schell, M.J. Hoffmann, Influence of the secondary phase LiTiOPO4 on the properties of Li1+xAlxTi2−x(PO4)3 (x=0; 0.3), Solid State Ionics. 302 (2016) 49–53. doi:10.1016/j.ssi.2016.10.008.

[51] B. Key, D.J. Schroeder, B.J. Ingram, J.T. Vaughey, Solution-based synthesis and characterization of lithium-ion conducting phosphate ceramics for lithium metal batteries, Chem. Mater. 24 (2012) 287–293. doi:10.1021/cm202773d.

[52] Y. Yoon, J. Kim, C. Park, D. Shin, The relationship of structural and electrochemical properties of NASICON structure Li1.3Al0.3Ti1.7(PO4)3 electrolytes by a sol-gel method, J. Ceram. Process. Res. 14 (2013) 563–566.

[53] K. Takada, Progress and prospective of solid-state lithium batteries, Acta Mater. 61 (2013) 759–770. doi:10.1016/j.actamat.2012.10.034.

[54] C.M. Chang, Y. Lee, S.H. Hong, H.M. Park, Spark plasma sintering of LiTi2(PO4)3-based solid electrolytes, J. Am. Ceram. Soc. 88 (2005) 1803–1807. doi:10.1111/j.1551-2916.2005.00246.x.

[55] J.S. Thokchom, B. Kumar, Microstructural effects on the superionic conductivity of a lithiated glass-ceramic, Solid State Ionics. 177 (2006) 727–732. doi:10.1016/j.ssi.2006.01.027.

[56] J.L. Narváez-Semanate, A.C.M. Rodrigues, Microstructure and ionic conductivity of Li1+xAlxTi2-x(PO4)3 NASICON glass-ceramics, Solid State Ionics. 181 (2010) 1197–1204. doi:10.1016/j.ssi.2010.05.010.

[57] N. Imanaka, T. Shimizu, G. Adachi, Lithium conducting amorphous solid electrolytes obtained by explosion method, Solid State Ionics. 62 (1993) 167–171. doi:10.1016/0167-2738(93)90368-D.

[58] H. Morimoto, H. Awano, J. Terashima, Y. Shindo, S. Nakanishi, N. Ito, K. Ishikawa, S.I. Tobishima, Preparation of lithium ion conducting solid electrolyte of NASICON-type Li1+xAlxTi2-x(PO4)3 (x = 0.3) obtained by using the mechanochemical method and its application as surface modification materials of LiCoO2 cathode for lithium cell, J. Power Sources. 240 (2013) 636–643. doi:10.1016/j.jpowsour.2013.05.039.

[59] X. Xu, Z. Wen, X. Yang, J. Zhang, Z. Gu, High lithium ion conductivity glass-ceramics in Li2O-Al2O3-TiO2-P2O5 from nanoscaled glassy powders by mechanical milling, Solid State Ionics. 177 (2006) 2611–2615. doi:10.1016/j.ssi.2006.04.010.

[60] M. Schroeder, S. Glatthaar, J.R. Binder, Influence of spray granulation on the properties of wet chemically synthesized Li1.3Ti1.7Al0.3(PO 4)3 (LATP) powders, Solid State Ionics. 201 (2011) 49–53. doi:10.1016/j.ssi.2011.08.014.

[61] R. Jiménez, A. del Campo, M.L. Calzada, J. Sanz, S.D. Kobylianska, S.O.

Solopan, A.G. Belous, Lithium La0.57Li0.33TiO3 Perovskite and Li1.3Al0.3Ti1.7 (PO4)3 Li-NASICON Supported Thick Films Electrolytes Prepared by Tape Casting Method, J. Electrochem. Soc. 163 (2016) A1653–A1659. doi:10.1149/2.0881608jes.

[62] Y. Matsuda, Y. Itami, K. Hayamizu, T. Ishigaki, M. Matsui, Y. Takeda, O. Yamamoto, N. Imanishi, Phase relation, structure and ionic conductivity of Li7−x−3yAlyLa3Zr2−xTaxO12, RSC Adv. 6 (2016) 78210–78218. doi:10.1039/C6RA13317G.

[63] M. Subramanian, R. Subramanian, A. Clearfield, Lithium ion conductors in the system AB(IV)2(PO4)3 (B = Ti, Zr and Hf), Solid State Ionics. 18–19 (1986) 562–569. doi:10.1016/0167-2738(86)90179-7.

[64] Z.X. Lin, H.J. Yu, S.C. Li, S.B. Tian, Lithium ion conductors based on LiTi2P3O12 compound, Solid State Ionics. 31 (1988) 91–94. doi:10.1016/0167-2738(88)90291-3.

[65] A. Martínez-Juárez, C. Pecharromán, J.E. Iglesias, J.M. Rojo, Relationship between Activation Energy and Bottleneck Size for Li+ Ion Conduction in NASICON Materials of Composition LiMM‘(PO4)3 ; M, M‘ = Ge, Ti, Sn, Hf, J. Phys. Chem. B. 102 (1998) 372–375. doi:10.1021/jp973296c.

[66] G. Nuspl, T. Takeuchi, A. Weiß, H. Kageyama, K. Yoshizawa, T. Yamabe, Lithium ion migration pathways in LiTi2(PO4)3 and related materials, J. Appl. Phys. 86 (1999) 5484–5491. doi:10.1063/1.371550.

[67] H.Y.P. Hong, Crystal structures and crystal chemistry in the system Na1+xZr2SixP3-xO12, Mater. Res. Bull. 11 (1976) 173–182. doi:10.1016/0025-5408(76)90073-8.

[68] K.M. Nairn, M. Forsyth, M. Greville, D.R. MacFarlane, M.E. Smith, Solid state NMR characterization of lithium conducting ceramics, Solid State Ionics. (1996) 1397–1402. doi:10.1016/0167-2738(96)00320-7.

[69] M. Forsyth, S. Wong, K.M. Nairn, A.S. Best, P.J. Newman, D.R. MacFarlane, NMR studies of modified nasicon-like, lithium conducting solid electrolytes, Solid State Ionics. 124 (1999) 213–219. doi:10.1016/S0167-2738(99)00213-1.

[70] K. Takada, M. Tansho, I. Yanase, T. Inada, A. Kajiyama, M. Kouguchi, S. Kondo, M. Watanabe, Lithium ion conduction in LiTi2(PO4)3, Solid State Ionics. 139 (2001) 241–247. doi:10.1016/S0167-2738(01)00688-9.

[71] D. Rettenwander, A. Welzl, S. Pristat, F. Tietz, S. Taibl, G.J. Redhammer, J. Fleig, A microcontact impedance study on NASICON-type Li1+xAlxTi2−x(PO4)3 (0 ≤ x ≤ 0.5) single crystals, J. Mater. Chem. A. 4 (2016) 1506–1513. doi:10.1039/C5TA08545D.

[72] M. Monchak, T. Hupfer, A. Senyshyn, H. Boysen, D. Chernyshov, T. Hansen, K.G. Schell, E.C. Bucharsky, M.J. Hoffmann, H. Ehrenberg, Lithium Diffusion Pathway in Li1.3Al0.3Ti1.7(PO4)3 (LATP) Superionic Conductor, Inorg. Chem.

55 (2016) 2941–2945. doi:10.1021/acs.inorgchem.5b02821.

[73] M.J. Verkerk, B.J. Middelhuis, A.J. Burggraaf, Effect of grain boundaries on the conductivity of high-purity ZrO2Y2O3 ceramics, Solid State Ionics. 6 (1982) 159–170. doi:10.1016/0167-2738(82)90083-2.

[74] T. Dijk van, A.J. Burggraaf, Grain boundary effects on ionic conductivity in ceramic GdxZr1-xO2-(x/2) solid solutions, Phys. Status Solidi A Appl. Res. 63 (1981) 229. doi:10.1002/pssa.2210630131.

[75] J. Fleig, J. Maier, The impedance of ceramics with highly resistive grain boundaries: validity and limits of the brick layer model, J. Eur. Ceram. Soc. 19 (1999) 693–696. doi:10.1016/S0955-2219(98)00298-2.

[76] J. Fleig, Influence of non-ideal microstructures on the analysis of grain boundary impedances, Solid State Ionics. 131 (2000) 117–127. doi:10.1016/S0167-2738(00)00627-5.

[77] J. Fleig, The grain boundary impedance of random microstructures: Numerical simulations and implications for the analysis of experimental data, Solid State Ionics. 150 (2002) 181–193. doi:10.1016/S0167-2738(02)00274-6.

[78] Superionic bulk conductivity in Li1.3Al0.3Ti1.7(PO4)3 solid electrolyte, Solid State Ionics. 309 (2017) 180–186. doi:10.1016/J.SSI.2017.07.023.

[79] T. Hupfer, E.C. Bucharsky, K.G. Schell, A. Senyshyn, M. Monchak, M.J. Hoffmann, H. Ehrenberg, Evolution of microstructure and its relation to ionic conductivity in Li1+xAlxTi2-x(PO4)3, Solid State Ionics. 288 (2016) 235–239. doi:10.1016/j.ssi.2016.01.036.

[80] K. Waetzig, A. Rost, U. Langklotz, B. Matthey, J. Schilm, An explanation of the microcrack formation in Li1.3Al0.3Ti1.7(PO4)3ceramics, J. Eur. Ceram. Soc. 36 (2016) 1995–2001. doi:10.1016/j.jeurceramsoc.2016.02.042.

[81] E. Kazakevičius, A. Kežionis, L. Žukauskaitė, M. Barré, T. Šalkus, A. Orliukas, Characterization of NASICON-type Na solid electrolyte ceramics by impedance spectroscopy, Funct. Mater. Lett. 07 (2014) 1440002. doi:10.1142/S1793604714400025.

[82] J.S. Thokchom, B. Kumar, Microstructural effects on the superionic conductivity of a lithiated glass-ceramic, Solid State Ionics. 177 (2006) 727–732. doi:10.1016/j.ssi.2006.01.027.

[83] H. Aono, E. Sugimoto, Y. Sadaoka, N. Imanaka, G. ya Adachi, Ionic conductivity and sinterability of lithium titanium phosphate system, Solid State Ionics. 40–41 (1990) 38–42. doi:10.1016/0167-2738(90)90282-V.

[84] H. Aono, E. Sugimoto, Y. Sadaoka, N. Imanaka, G. ya Adachi, Electrical property and sinterability of LiTi2(PO4)3 mixed with lithium salt (Li3PO4 or Li3BO3), Solid State Ionics. 47 (1991) 257–264. doi:10.1016/0167-2738(91)90247-9.

[85] H. Chung, B. Kang, Increase in grain boundary ionic conductivity of Li1.5Al0.5Ge1.5(PO4)3by adding excess lithium, Solid State Ionics. 263 (2014) 125–130. doi:10.1016/j.ssi.2014.05.016.

[86] S. Duluard, A. Paillassa, L. Puech, P. Vinatier, V. Turq, P. Rozier, P. Lenormand, P.L. Taberna, P. Simon, F. Ansart, Lithium conducting solid electrolyte Li1.3Al0.3Ti1.7(PO4)3 obtained via solution chemistry, J. Eur. Ceram. Soc. 33 (2013) 1145–1153. doi:10.1016/j.jeurceramsoc.2012.08.005.

[87] S. Duluard, A. Paillassa, P. Lenormand, P.L. Taberna, P. Simon, P. Rozier, F. Ansart, J. Ihlefeld, Dense on Porous Solid LATP Electrolyte System: Preparation and Conductivity Measurement, J. Am. Ceram. Soc. 100 (2017) 141–149. doi:10.1111/jace.14451.

[88] M. Kotobuki, B. Kobayashi, M. Koishi, T. Mizushima, N. Kakuta, Preparation of Li1.5Al0.5Ti1.5(PO4)3 solid electrolyte via coprecipitation using various PO4 sources, Mater. Technol. 29 (2014) A93–A97. doi:10.1179/1753555714Y.0000000181.

[89] N. Schön, D.C. Gunduz, S. Yu, H. Tempel, R. Schierholz, F. Hausen, Correlative electrochemical strain and scanning electron microscopy for local characterization of the solid state electrolyte Li1.3Al0.3Ti1.7(PO4)3, Beilstein J. Nanotechnol. 9 (2018) 1564–1572. doi:10.3762/bjnano.9.148.

[90] J.I. Goldstein, D.E. Newbury, P. Echlin, D.C. Joy, C.E. Lyman, E. Lifshin, L. Sawyer, J.R. Michael, Scanning Electron Microscopy and X-Ray Microanalysis, 10 (1992) 1983. doi:10.1080/00202967.1992.11870972.

[91] K. Kanaya, S. Okayama, Penetration and energy-loss theory in solid targets, J.Phys.D:Appl.Phys. 5 (1972) 43–58.

[92] S. Yu, A. Mertens, X. Gao, D.C. Gunduz, R. Schierholz, S. Benning, F. Hausen, J. Mertens, H. Kungl, H. Tempel, R.A. Eichel, Influence of microstructure and AlPO4 secondary-phase on the ionic conductivity of Li1.3Al0.3Ti1.7(PO4)3 solid-state electrolyte, Funct. Mater. Lett. 9 (2016) S1793604716500661. doi:10.1142/S1793604716500661.

[93] T.E. Everhart, R.F.M. Thornley, Wide-band detector for micro-microampere low-energy electron currents, J. Sci. Instrum. 37 (1960) 246–248. doi:10.1088/0950-7671/37/7/307.

[94] Ernst Ruska-Centre for Microscopy and Spectroscopy with Electrons, FEI Helios NanoLab 400S FIB-SEM, J. Large-Scale Res. Facil. JLSRF. 2 (2016) A59. doi:10.17815/jlsrf-2-105.

[95] Ernst Ruska-Centre for Microscopy and Spectroscopy with Electrons, FEI Tecnai G2 F20, J. Large-Scale Res. Facil. JLSRF. 2 (2016) A77. doi:10.17815/jlsrf-2-138.

[96] G. Elssner, H. Hoven, G. Kiessler, and P. Wellner, Ceramics and Ceramic Composites: Materialographic Preparation, R. Wert, Trans., Elsevier Science

Inc., 1999.

[97] T. Hupfer, E.C. Bucharsky, K.G. Schell, A. Senyshyn, M. Monchak, M.J. Hoffmann, H. Ehrenberg, Evolution of microstructure and its relation to ionic conductivity in Li1+xAlxTi2-x(PO4)3, Solid State Ionics. 288 (2016) 235–239. doi:10.1016/j.ssi.2016.01.036.

[98] N. V. Kosova, E.T. Devyatkina, A.P. Stepanov, A.L. Buzlukov, Lithium conductivity and lithium diffusion in NASICON-type Li 1+xTi2-xAlx(PO4)3 (x=∈0; 0.3) prepared by mechanical activation, Ionics (Kiel). 14 (2008) 303–311. doi:10.1007/s11581-007-0197-5.

[99] K.G. Schell, E.C. Bucharsky, F. Lemke, M.J. Hoffmann, Effect of calcination conditions on lithium conductivity in Li1.3Ti1.7Al0.3(PO4)3 prepared by sol-gel route, Ionics (Kiel). 3 (2016). doi:10.1007/s11581-016-1883-y.

[100] C.R. Mariappan, C. Yada, F. Rosciano, B. Roling, Correlation between micro-structural properties and ionic conductivity of Li1.5Al0.5Ge1.5(PO4)3 ceramics, J. Power Sources. 196 (2011) 6456–6464. doi:10.1016/j.jpowsour.2011.03.065.

[101] S. Poisson, F. D'Yvoire, Ng.H. Dung, E. Bretey, P. Berthet, Crystal Structure and Cation Transport Properties of the Layered Monodiphosphates: Li9M3(P2O7)3(PO4)2 (M 5 Al, Ga, Cr, Fe), J. Solid State Chem. 138 (1998) 32–40. doi:10.1006/jssc.1998.7751.

[102] F. Moreau, A. Durán, F. Muñoz, Structure and properties of high Li2O-containing aluminophosphate glasses, J. Eur. Ceram. Soc. 29 (2009) 1895–1902. doi:10.1016/j.jeurceramsoc.2008.12.016.

[103] M. Saidi, G. Coffy, F. Sibieude, Les systemes binaires AlPO4−M3PO4 (M =Li, Na, K), J. Therm. Anal. 44 (1995) 15–23. doi:10.1007/BF02547129.

[104] S. Poisson, F. D'Yvoire, H.D. Nguyen, E. Bretey, P. Berthet, Crystal structure and cation transport properties of the layered monodiphosphates : Li9M3(P2O7)3(PO4)2 (M = Al, Ga, Cr, Fe), J. Solid State Chem. 138 (1998) 32–40. doi:10.1006/jssc.1998.7751.

[105] R.W. Mooney, M.A. Aia, Alkaline earth phosphates, Chem. Rev. 61 (1961) 433–462. doi:10.1021/cr60213a001.

[106] E. Metwalli, R.K. Brow, Modifer effects on the properties and structures of aluminophosphate glasses, J. Non. Cryst. Solids. 289 (2001) 113–122. doi:10.1016/S0022-3093(01)00704-9.

[107] J.A. Bearden, X-ray wavelengths, Rev. Mod. Phys. 39 (1967) 78–124. doi:10.1103/RevModPhys.39.78.

[108] S. Wang, L. Ben, H. Li, L. Chen, Identifying Li^+ ion transport properties of aluminum doped lithium titanium phosphate solid electrolyte at wide temperature range, Solid State Ionics. 268 (2014) 110–116.

doi:10.1016/j.ssi.2014.10.004.

Appendix

```
function p = porosity(x)
if ~ismatrix(x)
   error('Input must be a matrix')
end
n = 1024*1024;     % Number of matrix elements of x matrix
prompt = 'What is the threshold? ';
t = input(prompt); % Threshold
y = x > t;         % Matrix elements of x greater than threshold will be displayed as 1 in y matrix
a = sum(sum(y));   % Rows and columns of y matrix are summed to find out how many 1 is included in y matrix
r = a/n;           % Fractional porosity: number of values greater than threshold/Total number of matrix elements
p = r*100;         % Porosity
end
```

Code 1: MATLAB function p is used to calculate the porosity of samples. Thresholds are employed to differentiate pores from dark grey regions.

Acknowledgement

First of all, I would like to express my sincere gratitude to Prof. Dr. Rüdiger-A. Eichel for providing me the opportunity to be a member of Forschungszentrum Jülich IEK-9. I am very grateful to him for his informative discussions, inspiration and guidance during the course of my thesis study. I am thankful to Prof. Dr. Joachim Mayer and Prof. Dr. Ullrich Englert for being the second and third reviewer of my thesis, respectively, as well as for their useful scientific discussions. I would like to also thank Prof. Dr. Lorenz Singheiser and Prof. Dr. Markus Albrecht for taking place in my doctoral committee as an examiner and a chairman, respectively.

I am indebted to Dr. Hans Kungl, Dr. Roland Schierholz, Dr. Hermann Tempel, Dr. Peter Jakes and Prof. Dr. Florian Hausen for fruitful scientific discussions, useful suggestions, and feedbacks. I am especially thankful to Dr. Roland Schierholz for his guidance, comments, discussions, friendship, and valuable suggestions on my research that helped me a lot. Working with him was a precious experience for me.

I would like to thank Nino Schön, Anja Paulus and Marc Paulus for their help, support, and discussions. I like to thank Shicheng Yu for the materials synthesis. Also, I want to thank Shicheng Yu and Andreas Mertens for the impedance results and Christian Hellenbrandt for his component support in the lab.

I feel lucky to be around the people of finest calibre in IEK-9, and I took delight at working with them and I am thankful to all of them. I am thankful to my officemates Daniel Kröger and Xiaochao Wu.

Last but not the least, I would like to thank my family for their unconditional love, endless support, and encouragement during my studies.

List of publications

Peer-reviewed publications:

[1] N. Schön, D.C. Gunduz, S. Yu, H. Tempel, R. Schierholz, F. Hausen, Correlative electrochemical strain and scanning electron microscopy for local characterization of the solid state electrolyte Li1.3Al0.3Ti1.7(PO4)3, Beilstein J. Nanotechnol. 9 (2018) 1564–1572. doi:10.3762/bjnano.9.148.

Contributions: D. C. Gündüz did the energy-dispersive X-ray spectroscopy measurements. He carried out the scanning electron microscopy (SEM) part of the correlative study and took part in atomic force microscopy measurements (AFM) with N. Schön to enable that AFM measurements are carried out in a correlative manner with SEM measurements.

[2] S. Yu, A. Mertens, X. Gao, D.C. Gunduz, R. Schierholz, S. Benning, F. Hausen, J. Mertens, H. Kungl, H. Tempel, R.A. Eichel, Influence of microstructure and AlPO 4 secondary-phase on the ionic conductivity of Li1.3Al0.3Ti1.7(PO4)3 solid-state electrolyte, Funct. Mater. Lett. 9 (2016) S1793604716500661. doi:10.1142/S1793604716500661.

Contributions: D. C. Gündüz carried out the microstructural characterization of $Li_{1.3}Al_{0.3}Ti_{1.7}(PO_4)_3$ superionic Li-conducting ceramic samples by the means of scanning electron microscopy and energy-dispersive X-ray spectroscopy.

[3] A. Mertens, S. Yu, N. Schön, D. Gunduz, H. Tempel, R. Schierholz, F. Hausen, H. Kungl, J. Granwehr, R.-A. Eichel, Superionic bulk conductivity in Li1.3Al0.3Ti1.7(PO4)3 solid electrolyte, Solid State Ionics. 309 (2017) 180–186. doi:10.1016/J.SSI.2017.07.023.

Contributions: D. C. Gündüz carried out the microstructural characterization of $Li_{1.3}Al_{0.3}Ti_{1.7}(PO_4)_3$ superionic Li-conducting ceramic samples via confocal laser

scanning microscopy and scanning electron microscopy. He also did the image analyses for this article.

[4] Crystallization and phase separation mechanism of silicon oxide thin films fabricated via e-beam evaporation of silicon monoxide, D.C. Gunduz, A. Tankut, S. Sedani, M. Karaman, R. Turan, Phys. Status Solidi C, 12: 1229–1235 (2015). doi: 10.1002/pssc.201510114.

Contributions: D. C. Gündüz is the main contributor to this publication. He prepared the samples, performed the spectroscopic characterisations, and wrote the article.

Papers to be submitted:

[1] D. C. Gunduz, R. Schierholz, S. Yu, A. Mertens, H. Tempel, H. Kungl and R.-A. Eichel, “Combined confocal laser scanning microscopy and scanning electron microscopy for microstructural analysis of Li1.3Al0.3Ti1.7(PO4)3 superionic Li-conducting ceramics”.

Contributions: D. C. Gündüz is the main contributor to this paper. He carried out the combined confocal laser scanning microscopy and scanning electron microscopy studies of $Li_{1.3}Al_{0.3}Ti_{1.7}(PO_4)_3$ superionic Li-conducting ceramic samples. He also did the image analyses and wrote the article. In this thesis, chapter 4 is based on this paper.

[2] D. C. Gunduz, R. Schierholz, S. Yu, A. Mertens, H. Tempel, H. Kungl and R.-A. Eichel, “Secondary phase evolution during sintering of Li1.3Al0.3Ti1.7(PO4)3 super-ionic Li-conducting ceramics”.

Contributions: D. C. Gündüz is the main contributor to this paper. He carried out the energy-dispersive X-ray spectroscopy studies of $Li_{1.3}Al_{0.3}Ti_{1.7}(PO_4)_3$ superionic Li-conducting ceramic samples and developed the novel image segmentation and reconstruction method. He also did all the image analyses and wrote the paper. In this thesis, chapter 5 is based on this paper.

Conference presentations:

[1] D. C. Gunduz, R. Schierholz, S. Yu, A. Mertens, H. Tempel, H. Kungl and R.-A. Eichel, “Microstructural Properties of Li1.3Al0.3Ti1.7(PO4)3 Solid-State Electrolyte”, The German Physical Society Spring Meeting, 2017, Dresden, Germany, Oral Contribution.

Contributions: D. C. Gündüz is the main contributor. He did the combined confocal laser scanning microscopy and scanning electron microscopy studies of $Li_{1.3}Al_{0.3}Ti_{1.7}(PO_4)_3$ superionic Li-conducting ceramic samples and image analyses.

Declaration

The work described in this thesis was performed by the author in the department of Prof. Dr. R.-A. Eichel at the Forschungszentrum Jülich for Fundamental Electrochemistry (IEK-9) from July 2015 to June 2018. The contents are the original work of the author except where indicated otherwise and have not been previously submitted for any other degree or qualification at any academic institution.

Jülich, March, 2019 Deniz Cihan Gündüz

Erklärung

Die vorliegende Doktorarbeit wurde vom Autor selbst in der Abteilung von Prof. Dr. R.-A. Eichel am Forschungszentrum Jülich für Grundlagen der Elektrochemie (IEK-9), im Zeitraum vom Juli 2015 bis Juni 2018 angefertigt. Der Inhalt ist die eigene Arbeit des Autors, Ausnahmen sind gekennzeichnet, und wurde noch nicht zur Erlangung einer Qualifizierung oder eines Titels an einer akademischen Institution eingereicht.

Jülich, März, 2019 Deniz Cihan Gündüz